Timing and distribution of post-subduction magmatism in the Southern Uplands of Scotland: New insights from U-Pb zircon data of Caledonian igneous bodies in the Southern Uplands Terrane

Chloe Angel Rebekah Gemmell BSc (Hons)

Submitted in fulfilment of the requirements of the Degree of Master of Science by Research

School of Geographical and Earth Sciences, College of Science and Engineering

University of Glasgow

October 2024

Abstract

The Southern Uplands of Scotland and its equivalent Down-Longford Terrane in Northern Ireland were part of a Palaeozoic accretionary complex on the Laurentian margin that actively accreted during the Ordovician and Silurian (~455 – 420 Ma). The Terranes were widely cross-cut by Devonian-aged 'Caledonian' intrusions related to subduction of the Iapetus oceanic slab and associated collision of peri-Gondwanan Terranes with Laurentia (~428 – 423 Ma). However, geochronological data is lacking for several magmatic bodies in the Southern Uplands Terrane. Consequently, the timing of specific geodynamic and tectonic events and the overall architecture of the resultant magmatic systems is uncertain. In this study, I conducted U-Pb zircon dating and partial zircon trace element analysis using laser ablation mass spectrometry for several under-studied intrusions, namely the Cairnsmore of Carsphairn pluton, the Black Stockarton Moor subvolcanic complex, the Bengairn and Cheviot plutons. I apply a cautious texturally and in part chemically constrained approach to determine an appropriate time of emplacement for these magmatic bodies and the total duration of magmatism, based on the occurrence of zircon cores interpreted as reflecting antecrystic zircon growth. Zircon is a robust mineral that is inherited from basement rock and/or newly crystallises from magmas at different depths throughout the crust (Roberts and Spencer, 2015), thus zircon records total durations of magmatism from deeper levels to emplacement. Zircon data can be integrated regionally to identify magmatic patterns (i.e., time of onset of magmatism vs emplacement) that in turn can be linked to geodynamic processes that are suspected within a specific region (Oliver et al. 2008; Yilmaz Şahin et al. 2014).

Results presented in this study support and advance previous work by confirming textural and geochronological evidence for long-lived pre-emplacement evolution of magmas, probably in a lower crustal hot zone setting. The earliest onset of zircon crystallisation at ~424 Ma reflects the start of Iapetus slab rollback following the onset of continental collision between Laurentia and peri-Gondwanan Terranes. A potential southwards younging in the onset of magmatism from northern bodies (e.g., Carsphairn) to southern bodies (e.g., Cheviot) is supportive of rollback. There is no obvious spatial pattern in emplacement, rather individual emplacement events appear to be randomly distributed, probably due to local tectonic controls and associated pathways for melt migration. Overall, little emplacement occurred prior

to ~415 Ma, but an upsurge in emplacement from hereon is coeval with a proposed switch from transpression to transtension; such an event might be concurrent with slab breakoff. Findings of this study imply that the Midland Valley and Grampian Highlands Terranes would benefit from further zircon studies of ‘Caledonian’ intrusions to define total durations of zircon growth and aim for high precision emplacement ages. This in turn would enable comparison between the geodynamic reconstruction presented here and geodynamic models for the Grampian Highlands and Midland Valley, to better understand the geodynamics over a broader sector of the Caledonian Orogen.

Table of Contents

List of Figures

List of Tables

Acknowledgements

First and foremost, I would like to thank Dr Iain Neill for his exceptional supervision throughout the duration of this project. I am extremely grateful for all the discussions, prompt Microsoft Teams chat replies and the invaluable guidance provided on both a professional and personal level throughout its duration. I would like to thank Iain for the memorable field days and the knowledge and insight he provided whilst in the field.

I would like to express a special thank you to the technical staff in the School of Geographical and Earth Sciences, especially to Dr Mark Wildman for his time and expertise which helped me navigate the challenging technical and data processing aspects of research. I would like to thank Dr David Currie at the British Geological Survey (BGS) for the time he dedicated to my trip down to BGS Keyworth and for the invaluable knowledge provided in follow-up conversations regarding data analysis and interpretation. I would like to extend my sincere thank you to the BGS for the Black Stockarton Moor borehole samples they provided. This project benefited from additional funding awarded to Dr Joshua Franz Einsle and I would like to thank him for this financial contribution which allowed for additional LA-ICP-MS analysis.

This project would not have been possible without the continuous support from my friends and fellow MRes students including Careen, Neve and Shona. A special thank you goes to Careen for her insight and unwavering support during field days, sample preparation, data processing and day-to-day research life. I am grateful for all the conversations and advice provided by fellow post-graduate students in Room 414/418 of the Molema Building.

On a more personal note, I would like to express my deepest appreciation to my family, especially to my Mum and Dad, who have shown unconditional support and have listened to many a geology conversation throughout my academic journey. Finally, words really cannot express my appreciation to my supervisor, Dr Iain Neill. His undergraduate igneous geology course was my inspiration for progressing into further research and I am incredibly grateful for the above and beyond support, encouragement, communication and patience he has shown throughout my academic journey.

Authors Declaration

I declare that, except where explicit reference is made to the contribution of others, that this dissertation is the result of my own work and has not been submitted for any other degree at the University of Glasgow or any other institution.

Printed name: **CHLOE ANGEL REBEKAH GEMMELL**

Signature:

1. Introduction

This thesis is as assessment of the quality and coverage of geochronology in Palaeozoic intrusions within the Southern Uplands of Scotland and will present new U-Pb zircon geochronological data from the Carsphairn, Bengairn and Cheviot plutons and the Black Stockarton Moor (BSM) subvolcanic complex.

For the purpose of this thesis, the following definitions will apply. Convergent margin magmatism refers to all magmatism occurring at convergent margins (e.g., continental arcs). Collision magmatism can be defined as magmatism which occurs following the onset of continental collision. Post-subduction magmatism represents a sub-set of collision magmatism (Richards, 2009) and is triggered after the subducting slab is no longer connected to the surface.

Magmatism is an intrinsic feature of the cycle of continental margin subduction, collision and post-collisional lithospheric delamination and/or slab breakoff (Bird, 1978; Freeburn et al. 2017; Neill et al. 2015; Song et al. 2015; von Blanckenburg and Davies, 1995a). The petrogenesis of such magmatism is highly debated and the role of crustal and lithospheric mantle melting as well as asthenospheric input is uncertain (Keskin, 2003; Lin et al. 2020; Neill et al. 2015; Pearce et al. 1990; von Blanckenburg and Davies, 1995; Williams, 2004). Several geodynamic models have been proposed to explain post-subduction magmatism in global collision zones, including slab break-off (Aldanmaz et al. 2000; Keskin, 2003; Neill et al. 2015; von Blanckenburg and Davies, 1995), lithospheric delamination (Aldanmaz et al. 2000; Keskin et al. 1998; Lin et al. 2020; Pearce et al. 1990), edge-driven convection (Missenard and Cadoux, 2012) and sub-lithospheric small-scale convection (Kaislaniemi et al. 2014). Several studies (Chapman et al. 2021; Ducea et al. 2015; Paterson and Ducea, 2015) have focused more on magma production such as “lulls” (i.e., input of small volumes of magma) vs “flare-ups” and their association with geodynamics within global convergent continental arc systems.

Magmatism which occurs following the onset of continental collision at locations which were originally continental margin accretionary complexes, are most likely to be locations where slab break-off is a dominant initial trigger for magmatism (Dilek and Altunkaynak, 2009; Keskin, 2003; Li et al. 2016; Rabayrol et al. 2019; Şengör et al. 2003; von Blanckenburg and Davies, 1995; Wu et al. 2022). Such locations are too close to the continent-ocean suture to be sites of continental arc magmatism and therefore magmatism by definition is only likely to occur following slab roll-back and breakoff (Altunkaynak, 2007; Dilek and Altunkaynak, 2009; von Blanckenburg and Davies, 1995; Wu et al. 2015). Today, Eastern Anatolia is a useful analogue for understanding post-subduction magmatism in such settings (Keskin, 2003; Pearce et al. 1990; Şengör et al. 2003). Here, extensive post-subduction magmatism is hosted in rocks which originated as a continental margin accretionary complex, namely the 'East Anatolian Accretionary Complex' (Ekici, 2016; Keskin, 2003; Neill et al. 2015; Skobeltsyn et al. 2014)**.** The modern East Anatolian region has a thin or even no lithospheric mantle below it and slab break-off is thought to have occurred beneath the complex within the last 10 -15 Myr (Al-Lazki et al. 2003; Ekici, 2016; Keskin, 2003; Şengör et al. 2003; Skobeltsyn et al. 2014). However, the specific mechanisms by which roll-back and breakoff lead to magmatism are uncertain (Keskin, 2003; Neill et al. 2015; Şengör et al. 2003; Skobeltsyn et al. 2014). Does breakoff immediately lead to an upsurge in magmatism by replacement of cold subducting lithosphere with hot upwelling asthenosphere? Does breakoff lead to surface uplift and crustal extension resulting in decompression melting of existing lower crust and (albeit thin) mantle lithosphere, as well as input of asthenospheric sources?

Most, if not all, ancient orogenic belts contain a record of magmatism which post-dates initial continental collision and, in many cases, will post-date the end of subduction processes (Altunkaynak, 2007; Chapman et al. 2021; Dilek and Altunkaynak, 2009; Ersoy et al. 2017; Keskin, 2003; Maury et al. 2000; Neill et al. 2015; Richards, 2009; Williams, 2004).The Southern Uplands of Scotland, the focus of this study, are one such example. This terrane contains extensive plutonic, sub-volcanic and volcanic suites of igneous rocks generated and emplaced between ~430 – 382 Ma (Hines et al. 2018; Miles et al. 2014). Magma generation and emplacement probably covers the termination of Iapetus subduction, the onset of continental collision, break-off and other post-subduction magmatic processes. However, there are few modern constraints on a range of features which can help reconstruct the precise geodynamic events and petrogenetic processes involved in their formation (Brown et al. 2008; Hines et al. 2018; Miles et al. 2014, 2016; Thirlwall, 1988).

Magmatic bodies in the Southern Uplands Terrane (SUT) have been variably dated by Rb-Sr and K-Ar mineral dating methods (Halliday et al. 1980; Thirlwall, 1988). These dating systems can provide valuable emplacement age data, however they are vulnerable to thermal resetting and element remobilisation during secondary alteration and therefore cannot recognise earlier pre-emplacement magmatism (Archibald et al. 2022; Miles et al. 2014). The U-Pb dating system is more robust and is not susceptible to mineral reheating or resetting by alteration (Oliver et al. 2008). U-Pb dating of zircons can constrain total durations of magmatism from onset through to emplacement (Archibald et al. 2021; Hines et al. 2018; Miles and Woodcock, 2018; Milne et al. 2023) which when integrated at a regional scale (i.e., across multiple plutons), can aid in deciphering wider geodynamic processes and crustal stress state during later stages of continental collision. U-Pb zircon dating has been applied to some plutons in the Southern Uplands (Hines et al. 2018; Miles et al. 2014), but coverage is not extensive and therefore requires further work. In comparison to better studied plutons in the Southern Uplands (e.g., Loch Doon pluton; Hines et al. 2018), the Carsphairn, Bengairn and Cheviot plutons and the BSM subvolcanic complex lack modern petrographic, geochronological and chemical data. Consequently, a complete timeline of late Caledonian magmatism across the Southern Uplands of Scotland has not been established and the geodynamic mechanisms triggering post-subduction magmatism remain contentious.

This study will therefore assess existing geochronological data and wider interpretations made using this data with a key goal of applying a more robust technique that is, U-Pb zircon geochronology to identify previously unobserved clues in the rock record that might provide a better insight into the magmatic history and its geodynamic implications beneath the Southern Uplands prism. There is also little recent investigation of how magmatism relates to known occurrences of mineralisation in the region, specifically porphyry copper deposits (Brown et al. 1979b). Understanding magmatic evolution and its implications for crustal stress state could aid in better understanding mineralisation paragenesis and the relationship between magmatism and mineralisation in the Southern Uplands (Chiaradia, 2022; Richards, 2009).

U-Pb dating, and trace element geochemical analysis of zircons is employed to address the following **aim** and **objectives.**

- **Aim:** To fully constrain the timing of the onset of magmatism and the duration of emplacement magmatism in the lesser-studied Carsphairn, Bengairn and Cheviot plutons and in the Black Stockarton Moor subvolcanic complex of the Southern Uplands of Scotland.

The **objectives** are as follows:

- To obtain new U-Pb zircon geochronological data from the under-studied Carsphairn, Bengairn and Cheviot plutons and the Black Stockarton Moor subvolcanic complex.

- To further substantiate the presence of antecrystic zircons which may be consistent with the development of lower crustal hot zones beneath the Southern Uplands towards the end of Iapetus subduction.

- To accurately determine an appropriate time of emplacement for the Carsphairn and Cheviot plutons for which previous Rb-Sr dates exist and for the Bengairn pluton and Black Stockarton Moor subvolcanic complex for which no previous geochronological data is available.

- To determine if zircon trace element chemistry can distinguish between zircon rims (i.e., plausible emplacement growth) and zircon cores (i.e., plausible antecrystic growth).

- To integrate the onset of magmatism ages and zircon crystallisation ages interpreted as appropriate times of emplacement with existing literature for the Southern Uplands-Down-Longford Terranes and discuss a new geodynamic interpretation for the Laurentian margin of the British – Irish Caledonides during collision of peri-Gondwanan terranes at the time of the Caledonian Orogeny.

These objectives will be achieved by a workflow which will include fieldwork, optical mineralogy, scanning electron microscopy cathodoluminescence (SEM-CL) imaging, laser ablation inductively coupled mass spectrometry (LA-ICP-MS), U-Pb zircon geochronology and trace element geochemistry.

2. Previous Work

2.1. The Caledonian Orogeny

The Cambrian – Devonian Caledonian Orogeny in Britain and Ireland involved tectonism between the Laurentian, Baltican and peri-Gondwanan continental, relating to closure of the Iapetus Ocean (Archibald et al. 2022; Chew and Strachan, 2014; McKerrow et al. 2000; Oliver et al. 2008). The British and Irish Caledonides, positioned between the North American Appalachian Orogen (to the south) and the Scandinavian and East Greenland Caledonides (to the north), experienced three orogenic events during Iapetus closure, that is the Ordovician Grampian Orogeny(ies) (*c.* 475 – 460 Ma; 450 Ma), the Silurian Scandian Orogeny (*c.* 437 – 415? Ma) and the early Devonian Acadian Orogeny (*c.* 404 – 394 Ma) (Archibald et al. 2022; Chew and Strachan, 2014; Dewey and Mange, 1999; Dewey and Ryan, 2016; Miles et al. 2014; Soper et al. 1999; Strachan et al. 2020; Woodcock et al. 2007).

2.1.1. The Grampian event and the onset of accretion

During the Grampian orogeny (Fig. 2.1 a), the Laurentian margin of Scotland and northwest Ireland collided with an intra-oceanic (i.e., the Midland Valley) island arc which lay above a south-dipping subduction zone (Archibald et al. 2022; Chew and Strachan, 2014; Dewey et al. 2015; Dewey and Ryan, 2016; Miles et al. 2016). This event triggered obduction of ophiolites onto the southern margin of the island arc terrane, considered part of Laurentia by this time (e.g., Ballantrae Igneous Complex of Midland Valley), as well as regional deformation and metamorphism in the Northern Highland and Grampian Highland Terranes (Archibald et al. 2022; Chew and Strachan, 2014; Jones and Blake, 2003; Miles et al. 2016; Walker et al. 2020). Ophiolite obduction also marked a switch in subduction polarity of the Iapetus slab (Fig. 2.1 a), from southward dipping to a new northward dipping subduction zone, marking the onset of the formation of the Southern Uplands accretionary prism formation along the Laurentian margin (Archibald et al. 2022; Chew and Strachan, 2014; Jones and Blake, 2003; Leggett et al. 1983; Miles et al. 2014; Stone, 2014; Walker et al. 2020).

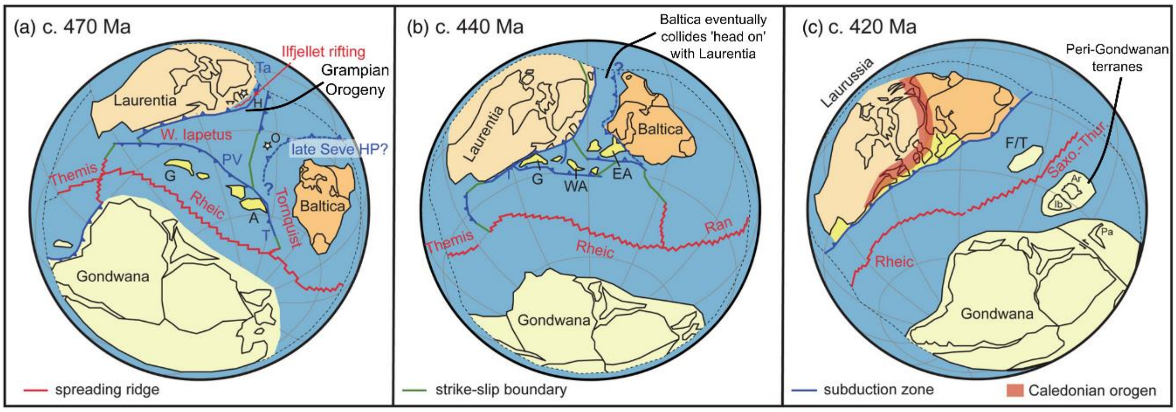

Figure 2.1: Palaeogeographical plate reconstruction for different phases of the Caledonian Orogeny. (a) At ~470 Ma the Grampian Orogeny was taking place during which subduction beneath an intra-oceanic island arc was occurring. Laurentia eventually collided with this arc and there was a switch in subduction polarity of the Iapetus slab, marking the onset of a new N dipping subduction zone beneath Laurentia and the beginning of Southern Uplands accretionary prism formation. A = Avalonia, G = Ganderia (b) At ~440 Ma the Scandian Orogeny was about to begin (*c.* 437 Ma). In the N sector of the Iapetus Ocean, Baltica would eventually collide 'head on' with Laurentia, defining the Scandian Orogeny (not shown). In the S sector, peri-Gondwanan microcontinents would eventually undergo highly oblique collision with Laurentia. It is key to note that this palaeogeographical reconstruction reproduced and adapted from Gasser et al. (2024) divides Avalonia into Western Avalonia (WA) and Eastern Avalonia (EA) and depicts EA as colliding with Baltica. This is not discussed in text. The 'head on' collision between Baltica and Laurentia is also marked as uncertain (blue question mark) in their reconstruction. (c) At ~420 Ma the Iapetus Ocean is thought to have closed and is associated with the onset of continental collision. Peri-Gondwanan terranes Armorica (Ar) and Iberia (Ib) are shown. The position of the Grampian Orogeny was estimated from van Staal et al's., (2021) plate reconstruction.

During Iapetus subduction, the accretionary prism advanced when sequences of submarine pelagic, volcaniclastic and turbidite sediments and continental-derived material of Laurentian provenance were sequentially scraped from the downgoing oceanic slab and thrust onto the Laurentian margin (Fig. 2.2), with younger slices thrust beneath older ones (Fig. 2.2), forming an inverted stratigraphic succession (Stone et al. 2012; Stone, 2014; Waldron et al. 2008)**.** Sedimentation in the prism occurred between *c.*455 – 420 Ma (Brown et al. 2008; Mckerrow et al. 1977; Oliver et al. 2008; Watson, 1984). Stratigraphic sequences experienced polyphase deformation and were structurally rotated to an upright position (Fig 2.2), forming the distinct Southern Uplands stratigraphic tracts bounded by NE-SW striking faults (Stone, 2014; Waldron et al. 2008).

It should be noted that deformation and high-grade metamorphism of the western Northern Highlands terrane (NHT), associated with the Grampian II event *(c.* 450 Ma), despite being concurrent with the onset of subduction beneath the Laurentian margin, has been linked with alternative triggers such as accretion of an arc-derived microcontinental block further north and east along the Laurentian margin (Bird et al. 2013), a period of flat slab subduction (Dewey et al. 2015), or the onset of collision between the Northern Highlands and a Baltican promontory (Milne et al. 2023). Shortening structures (e.g., folding, cleavage formation) in the Dalradian Supergroup of the Grampian Highlands Terrane (GHT) may also be related to this ~450 Ma event (Chew and Strachan, 2014). The trigger of this event ultimately remains unresolved (Walker et al. 2020).

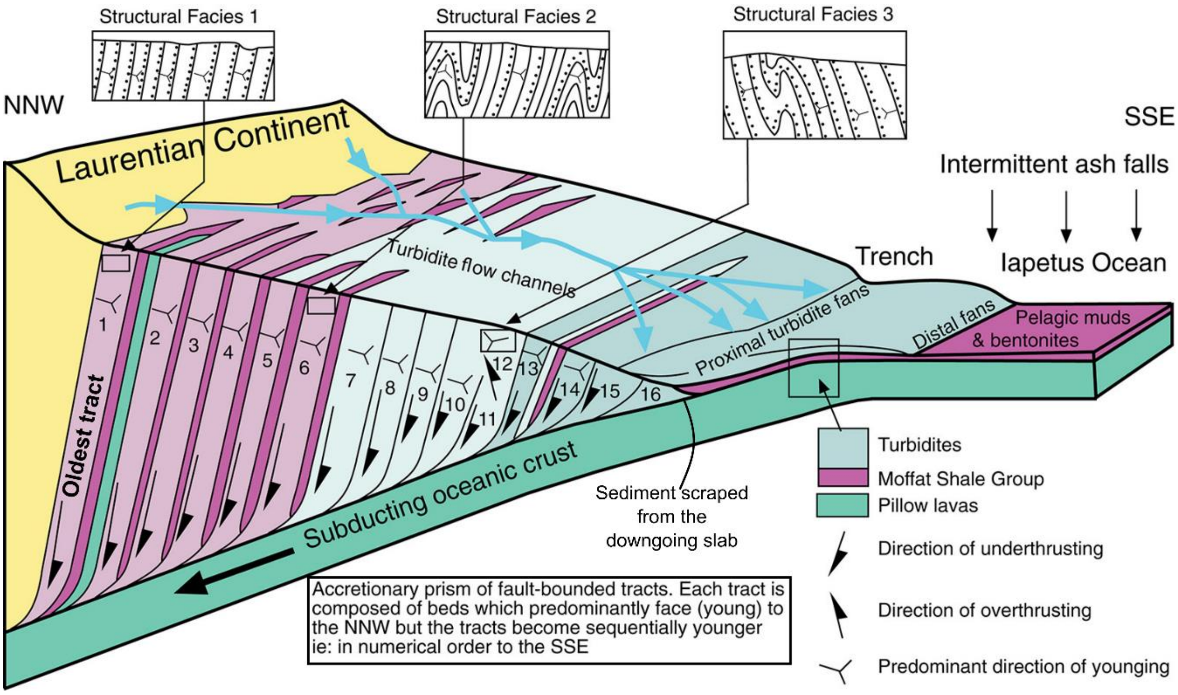

Figure 2.2: Summary of the formation of the Southern Uplands – Down - Longford Terrane according to the accretionary prism model of Legget et al. (1979). Reproduced and adapted from Chew and Strachan (2014).

2.1.2. The Scandian Orogeny and Iapetus closure

Final closure of the Iapetus Ocean involved two distinct tectonic regimes, one operating further north and the other further south (Soper and Woodcock, 2003). The Scandian Orogeny (*c.* 437 – 415 Ma?) marks the closure of the northern sector of the Iapetus Ocean, during which Baltica collided 'head on' with Laurentia (Fig. 2.1 b) causing significant regional deformation and metamorphism in the Northern Highlands Terrane (Bird et al. 2013; Chew and Strachan, 2014; Dewey and Strachan, 2003; Strachan et al. 2020; van Staal et al. 2021). Terranes south of the major strike-slip-dominated Great Glen Fault (GGF) were not directly involved in the Scandian event (Soper and Woodcock, 2003). Further south, peri-Gondwanan microcontinents, including Ganderia and Avalonia, underwent a 'soft' (i.e., highly oblique) collision with Laurentia (Fig. 2.1b) starting during the Silurian (*c.* 428 – 423 Ma), producing weak deformation and metamorphism in the Southern Uplands

Terrane, and marking the final closure of the Iapetus Ocean in this region (Fig. 2.1 c; Chew and Strachan, 2014; Dewey and Strachan, 2003; Mendum, 2012; Oliver et al. 2008; Schofield et al. 2016; Soper and Woodcock, 2003).

There is some controversy around the tectonics of the Scandian – Acadian events (Dewey and Strachan, 2003; Soper and Woodcock, 2003). In Dewey and Strachan's (2003) model, an orogen-wide switch took place from Scandian sinistral transpression (*c.* 435 – 425 Ma) to a time of regional strike-slip faulting, associated "Newer Granite" emplacement (*c.* 425 – 410 Ma) and early Devonian transtension (*c.* 420 – 400 Ma). As is true of various models over the last three decades, this work considers the northern and southern British Caledonides as belonging to one broad tectonic regime.

In contrast, Soper and Woodock (2003) consider British-Irish terranes north of the Great Glen Fault (i.e., those affected by the Scandian Orogeny) to be in a different tectonic regime to those south of it (i.e., Grampian Highland Terrane, Midland Valley Terrane, Southern Uplands Terrane). They argue that Silurian deformation south of the Great Glen Fault does not fit with progressive orogen wide models (e.g., Dewey and Strachan, 2003). Instead, a model is proposed for the southern terranes whereby sinistral transpression and Iapetus closure (until c. 420 Ma) was associated with strike-slip faults, flexural and transtensional basin formation (Soper and Woodcock, 2003). This was followed directly by a period of orogen-wide early Devonian transtension (*c.* 420 – 400 Ma, as opposed to having a period of strike-slip faulting proposed by Dewey and Strachan, 2003) associated with fluvial sediment deposition (e.g., Old Red Sandstone group; *c.* 420 – 400 Ma) lamprophyric and felsic magmatism (Brown et al. 2008; Chew and Strachan, 2014; Dewey and Strachan, 2003; Mendum, 2012; Oliver et al. 2008; Rock et al. 1986; Soper and Woodcock, 2003). The Acadian Orogeny (*c.* 404 – 394 Ma) marks the end of this transtensional event in southern Britain (Soper and Woodcock, 2003).

2.1.3. The short-lived Acadian Orogeny

It has been proposed that the Acadian orogeny (*c.* 404 – 394 Ma) involved collision of the peri-Gondwanan microcontinent Amorica or Iberia with Avalonia (Fig. 2.1 c), likely causing fault displacement along the Great Glen Fault, Highland Boundary Fault (HBF) and Southern Upland fault and strong deformation and metamorphism in the early Palaeozoic sedimentary rocks in terranes south of the Iapetus suture (Mendum, 2012; Woodcock et al. 2019; Woodcock et al. 2007; Woodcock and Strachan, 2012). However, it should be noted that there is much debate around what terranes were actually involved in the Acadian orogeny in the British-Irish sector of the Caledonides (van Staal et al. 2021; Waldron et al. 2014; Woodcock et al. 2019). Activity within the Southern Uplands Moniaive Shear Zone is attributed to the Acadian event (Soper and Woodcock, 2003)**.** The beginning of the Acadian event marks the end of the Caledonian orogeny (Mendum, 2012; Woodcock et al. 2007)

2.2. Geological Background of the Southern Uplands Terrane

The Southern Uplands-Down-Longford Terrane consists of a series of turbidite-dominated marine siliclastic rocks deposited into the accretionary prism between *c.* 455 – 420 Ma (Brown et al. 2008; Oliver et al. 2008; Watson, 1984). Regionally, the terrane is divided into three fault-bounded chunks (Fig. 2.3), younging southwards, namely the Ordovician northern belt and Ordovician(?) to mid-Silurian central to southern belts (McKerrow, 1987; Stone, 2014; Waldron et al. 2008), all of which comprise multiple tracts separated by significant thrust faults, in which individual slices young from south to north (Chew and Strachan, 2014; Jones and Blake, 2003; Leggett et al. 1982, 1979; Woodcock and Strachan, 2012).

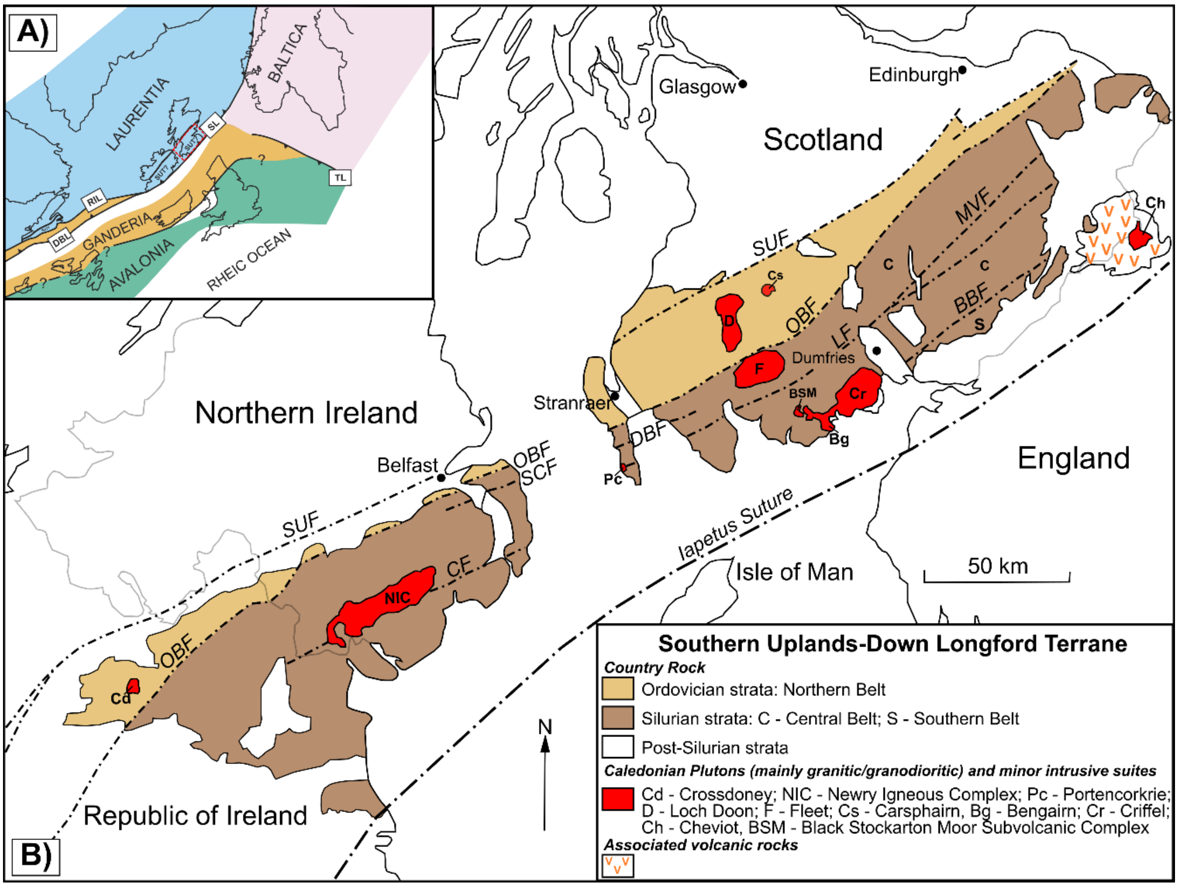

Figure 2.3: (A) Palaeogeographical tectonic reconstruction at ~420 Ma as per Figure 2.1 c (not to scale). RIL = Red Indian Line; DBL = Dog Bay Line; TL = Tornquist Line; SL = Solway Line. Adjusted from Waldron et al. (2014). (B) Three Belts of the Southern Uplands – Down - Longford Terrane including the Northern, Central (C) and Southern (S) Belts. Distribution of Caledonian plutons, volcanic rocks, intrusive suites and significant faults also shown. SUF = Southern Uplands Fault; OBF = Orlock Bridge Fault; LF = Laurieston Fault, MVF = Moffat Valley Fault; BBF = Balmae Burn Fault; CF = Cloghy Fault; SCF = Southern Coalpit Bay Fault; DBF = Drumbreddan Bay Fault. Adapted from Cooper et al. (2016), Miles et al. (2014) and Stone et al. (2012). Reproduced in Gemmell et al. (2025).

2.3. Models for Caledonian magmatism south of the Great Glen Fault

2.3.1. The "Newer Granite" suite and other classifications

The Caledonian Orogeny in Britain and Ireland was accompanied by a period of late Silurian to early Devonian post-subduction magmatism (*c.* 437 – 370 Ma) extending across all terranes north of the suture in the form of granitoid plutons, widespread dyke swarms, stocks, sheets and volcanic activity (Atherton and Ghani, 2002; Brown et al. 2008; Rock et al. 1986). Previous U-Pb and Rb-Sr dating identified emplacement magmatism between ~415 – 385 Ma in the Southern Uplands accretionary prism (Halliday et al. 1980; Hines et al. 2018; Miles et al. 2014; Thirlwall, 1988).

When discussing late Caledonian magmatism in the context of regional tectonic events, this study has taken the view that magmatism in terranes north (i.e., in the Northern Highlands Terrane) and south of the Great Glen Fault (i.e., Grampian Highlands, Southern Uplands) should be considered separately. This is because these terranes ultimately occupied different positions along the Laurentian margin, were initially involved in different collision events (Fig. 2.1 b) and were separated at the time by several hundred kms of lateral offset on the Great Glen Fault (Chew and Strachan, 2014). Northern Highland Terrane granites are therefore not considered further here, in contrast to the regional syntheses of e.g., Miles et al. (2016). Caledonian magmatic bodies of the Grampian Highlands Terrane and Southern Uplands Terrane are related to Iapetus subduction and convergence and collision between peri-Gondwanan terranes and the Laurentian margin (Fig. 2.1 b).

Traditionally, most of the Caledonian granites emplaced sometime after Grampian deformation are classed as "Newer Granites" after Read (1961). The group was divided into two categories, the 'forceful' intrusions (to which he assigned Carsphairn) and the 'last' intrusions (e.g., Cheviot), subdivided largely on the basis of different perceived pluton emplacement mechanisms. The term "Newer Granites" is, however, problematic as it originated at a time when the geochemical and petrogenetic variability, geochronology and emplacement mechanisms of different bodies, was less well understood than today (Milne et al. 2023).

Others, such as Stephens and Halliday (1984) preferred to classify late Caledonian bodies according to geochemical, petrographic and isotopic characteristics, delineating three suites for those bodies south of the Great Glen Fault, that is the Cairngorm suite, the Argyll suite and the South of Scotland suite (Fig. 2.4). Stephens and Halliday's (1984) original classification was heavily influenced by the work of Chappel, White and others (Chappell and White, 2001) on so-called I, S and A-type granites of different protolith compositions and tectonic settings. I-type granites were attributed to melting of igneous lower crust, S-type to sedimentary protoliths, and A-type to melting of upper mantle and subsequent fractional crystallisation under largely anorogenic conditions. Stephens and Halliday (1984) identified the Cairngorm suite (Fig. 2.4) as largely I - A type with low Ba-Sr abundances and few associated intermediate and mafic rocks. Plutons of this suite were characterised by positive εSr and $\delta^{18}O$ signatures and negative εNd values, reflective of significant crustal melting during petrogenesis (Lawrence et al. 2023; Stephens and Halliday, 1984). The Argyll suite included all late-Caledonian plutons in the NW Grampian Highlands, defined by dominantly I-type granodioritic - dioritic compositions, high Ba-Sr concentrations and associated appinites. Broadly, the εSr, εNd and $\delta^{18}O$ signatures of this suite span mantle and crustal-like compositions (Dewey et al. 2015; Fowler et al. 2008; Lawrence et al. 2023; Stephens and Halliday, 1984). The South of Scotland suite (Fig. 2.4) consisted of plutons in the Southern Grampian Highlands, Midland Valley and Southern Uplands Terranes, except for the Criffel and Fleet plutons (Stephens and Halliday, 1984). These are mainly I-type low Ba-Sr granodiorite – diorite plutons, with appinitic rocks related to the northern most plutons. Bodies of this suite are generally marked by positive εSr and $\delta^{18}O$ and varied εNd signatures, reflecting heterogenous crustal and mantle input during genesis (Stephens and Halliday, 1984). Both Criffel and Fleet were excluded from this classification due to their anomalous S-type characteristics compared to other late-Caledonian plutons (Halliday et al. 1980; Stephens and Halliday, 1984, 1979).

Later classifications extended Stephens and Halliday's (1984) three suite classification to include some Northern Highland plutons i.e., the Argyll and Northern Highlands Suite of Highton (1999). The S-type Southern Uplands plutons (e.g., Criffel, Fleet, Cheviot), excluded from Stephens and Halliday's (1984) classification, were termed the ‘Galloway Suite’ after Highton (1999) where they differentiated these bodies from the south of Scotland suite (Fig. 2.4) by their broadly younger age, S-type affinities and compositional zoning (e.g., from I-type margins to S-type granitic centre for Criffel; Stephens and Halliday, 1979). This suite comprises a variety of rock types, including diorite, granodiorite and granite compositions (Halliday et al. 1980; Highton, 1999). Galloway plutons broadly exhibit crustal-like $^{87}Sr/^{86}Sr$ ratios, $\delta^{18}O$ signatures and εNd values (Halliday, 1984; Halliday et al. 1980; Highton, 1999). Interaction between mantle and/or mafic lower crustal sources and metasedimentary partial melts of Lower Palaeozoic turbidite sequences have been proposed to explain the complex isotopic signatures and compositional zonation of most Galloway plutons (see Halliday, 1984; Halliday et al. 1980, 1979; Highton, 1999; Macdonald and Fettes, 2006).

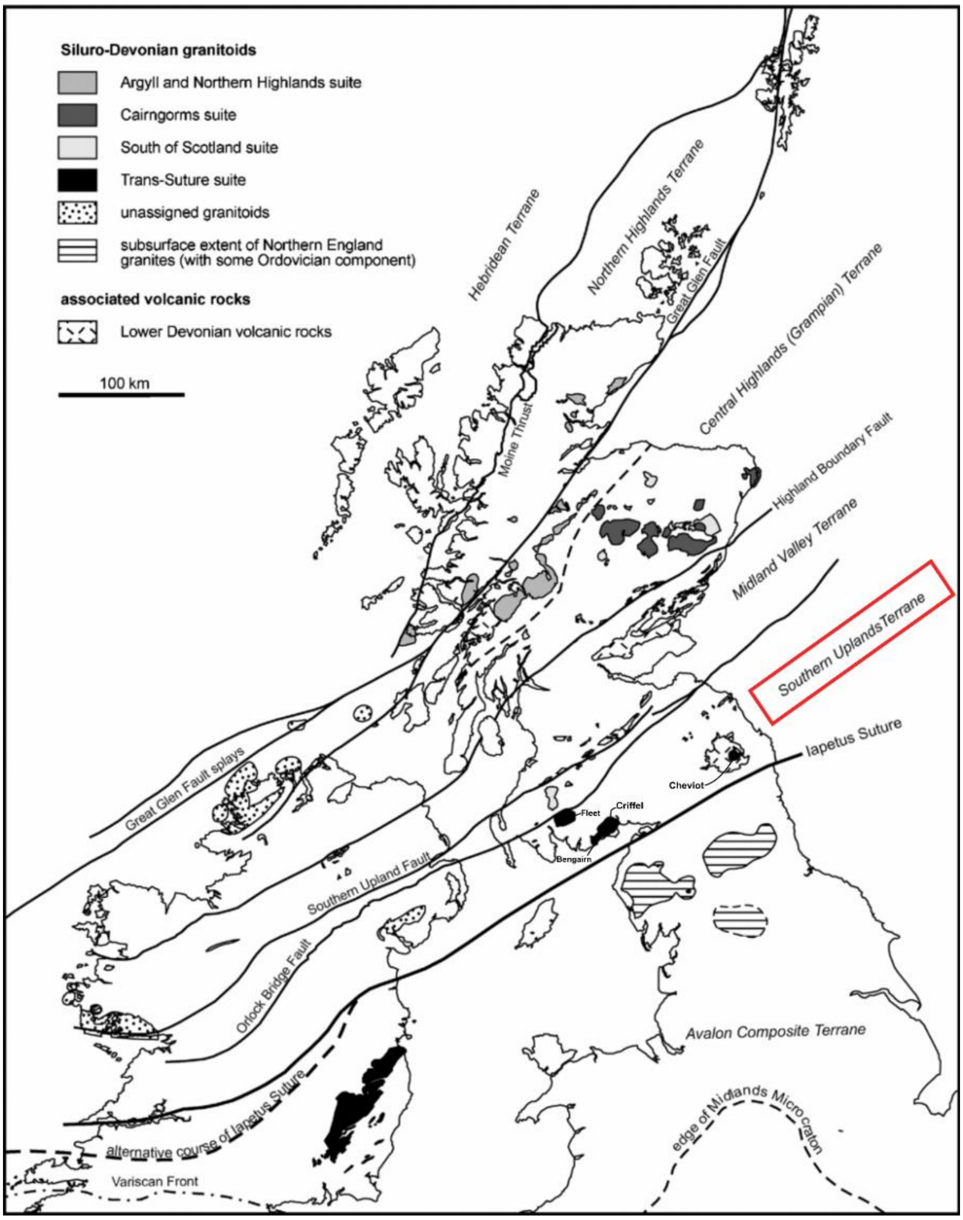

Figure 2.4: Map of the distribution of Caledonian plutonic or intrusive bodies across the British – Irish sector and their classifications as discussed in text. The Southern Uplands Terrane is outlined in red, and all major faults are annotated. See Figure 2.3 for pluton and complex names. Reproduced and adapted from Brown et al. (2008).

The Southern Uplands Moniaive Shear Zone or Orlock Bridge fault (OBF; Fig. 2.4) has further been interpreted as a ‘compositional break in crust’ determined from geophysical modelling of the subsurface and recognition of a lower crustal – upper mantle discontinuity below the Southern Uplands Terrane (Highton, 1999; Macdonald and Fettes, 2006; Stone et al. 1997). In some papers, broadly older isotopically and geochemically distinct late-Caledonian I-type plutons north of the fault (that is the three groups of Stephens and Halliday, 1984) are defined as ‘Northern Granites’ (e.g., Dewey et al. 2015), distinct from younger S-type plutons south of the fault (that is the ‘Galloway Suite’ of Highton, 1999).

The once defined ‘Galloway Suite’ (Highton, 1999) has since been expanded and re-defined as the ‘Trans-suture Suite’ (Brown et al. 2008) encompassing those late-Caledonian Scottish, Irish and northern English bodies south of the Orlock Bridge Fault (excluding unassigned Irish granites of Brown et al. 2008), occurring both north and south of the Iapetus Suture (Fig. 2.4). Brown et al. (2008) defined the Trans-suture Suite (TSS) plutons based on their distinct early Devonian tectonic emplacement setting, broadly younger age (*c.* 400 – 390 Ma) and shared S-type affinities compared to those plutons north of the Orlock Bridge Fault (Fig. 2.4). Notably, those Southern Uplands bodies classed as Trans-suture Suite plutons (e.g., Fleet, Criffel, Cheviot) exhibit $^{87}Sr/^{86}Sr$, $\delta^{18}O$ and εNd isotopic signatures indicating significant crustal input during genesis (Brown et al. 2008; Halliday, 1984; Halliday et al. 1980; Highton, 1999; Miles et al. 2014).

Whilst the Southern Uplands plutons south of the Orlock Bridge Fault fit with the TSS classification in that they are generally younger than those intrusions to the north (Table 2.1 e.g., Fleet, Criffel), they do not conform to the TSS classification in all respects. Several geochronological studies of these plutons produced Rb-Sr and U-Pb ages outwith the range of *c.* 400 – *c.* 390 Ma proposed by Brown et al. (2008). This classification also excludes plutons north of the Orlock Bridge Fault (that is ‘South of Scotland Suite’), some of whose U-Pb emplacement ages are distinctly younger than surrounding bodies (Table 2.1 e.g., Loch Doon). The Bengairn pluton and Black Stockarton Moor subvolcanic complex were not considered in the original TSS classification (Brown et al. 2008). Recent studies (Hines et al. 2018; Miles et al. 2016) argue for common isotopic, geochemical and geochronological characteristics between plutons north (e.g., Carsphairn, Doon) and South (e.g., Fleet, Criffel, Cheviot) of the Orlock Bridge Fault and group all Southern Uplands plutons as the one suite.

Table 2.1: Summary Rb-Sr and U-Pb age data for Caledonian bodies across the Southern Uplands Down-Longford Terrane of Britain and Ireland. See Figure 2.3 for relative locations of igneous bodies. Bodies are described in age order from the youngest known emplacement age with some plutons producing a range of emplacement ages for different rock types. Rb-Sr ages have been recalculated according to the revised ^{87}Rb decay constant as per Villa et al. (2015) and are presented to 2σ. Weighted mean ^{206}Pb/^{238}U ages are reported to 2σ for U-Pb analysis of zircons as per the literature. The Crossdoney pluton (Ireland) is an exception, where a weighted mean ^{207}Pb/^{206}Pb age was recalculated to give a final emplacement age. Abbreviations are as follows. CBS and NBS = Central Belt (CB) and Northern Belt (NB) of the Southern Uplands of Scotland; E = England; I = Ireland. WR = whole-rock analysis. Bt = biotite. Ms = muscovite. Ap = apatite. IMP = ion microprobe. LA-ICP-MS = laser ablation inductively coupled mass spectrometry. TIMS = thermal ionisation mass spectrometry. Reproduced in Gemmell et al. (2025).

Name	Location and type of magmatism	Rb-Sr-derived time of emplacement	Method	U-Pb zircon-derived time of emplacement	Ages of antecrystic zircon growth	Method	References
Fleet	CBS pluton	399.4 ± 2.1	Bt-Ms WR	387 ± 5 Ma for inner muscovite granite; 410 ± 3 Ma for outer biotite granite	Not apparent	U-Pb IMP	*Halliday et al. (1980); Miles et al. (2014)*
Portencorkrie	CBS pluton	399.9 ± 19.4	WR	395 ± 9 Ma	Not apparent	U-Pb IMP	*Evans (1975); Oliver et al. (2008)*
Doon	NBS pluton	416.5 ± 1.5	Bt-WR	396.7 ± 4.3 Ma for outer quartz diorite; other zones provided older ages interpreted as antecrystic or inherited	~416-424 Ma	U-Pb LA-ICP-MS	*Halliday et al. (1980); Hines et al. (2018)*
Cheviot	SBE+S pluton and volcanic complex	403.8 ± 3.0 403.8 ± 3.9	Bt-WR Bt-Ap	*This study*	*This study*	U-Pb LA-ICP-MS	*Thirlwall et al. (1988); this study*
Bengairn	CBS pluton	Not analysed	n/a	*This study*	*This study*	U-Pb LA-ICP-MS	*This study*
Criffell-Dalbeattie	CBS pluton	404.2 ± 2.0	Bt-WR	Range from 408 ± 14 to 412 ± 5 Ma for four zones out of five identified. Overall emplacement age of 410 ± 6 Ma	Not apparent	U-Pb IMP	*Halliday et al. (1980); Miles et al. (2014)*
Newry	CBI plutonic complex	Range from 411.1 ± 3.1 to 407 ± 3.1	WR	Range from 414.0 ± 0.2 to 410.3 ± 0.2 Ma for three zones (Seeconnell, Rathfriland, Newry) and 407.2 ± 0.4 Ma for a younger zone (Cloghoge)	~415 Ma, in Rathfriland zone	U-Pb TIMS	*O'Connor (1975); Cooper et al. (2016)*
Cairnsmore of Carsphairn	NBS pluton	418.6 ± 4.1	WR	*This study*	*This study*	U-Pb LA-ICP-MS	*Thirlwall et al. (1988); this study*
Crossdoney	NBI pluton	Not analysed	n/a	Granite re-interpreted as 413.2 ± 1.7 Ma (n = 18, MSWD = 0.8).	Not apparent in original study but likely up to 425 Ma as re-interpreted.	U-Pb IMP	*Fritschle (2016), re-interpreted here*
Black Stockarton Moor	CBS sub-volcanic minor intrusions	Not analysed	n/a	*This study*	*This study*	U-Pb LA-ICP-MS	*This study*

2.3.2. Geodynamic models for Southern Uplands magmatism

The transition from subduction to continental collision involves many phases, in particular subduction itself and the angle of the subducting slab, slab rollback upon commencement of collision, slab break-off into the underlying asthenosphere, and wider lithospheric delamination (Aldanmaz et al. 2000; Chemenda et al. 2000; Ding et al. 2017; Keskin, 2003; Lin et al. 2020; Neill et al. 2015; Pearce et al. 1990; Toussaint et al. 2004; von Blanckenburg and Davies, 1995; Williams, 2004).

In this context, bearing in mind the Palaeozoic age of the Caledonian Orogeny, many different geodynamic models have emerged to describe the evolution of the collision zone. Many of these models rely on interpretation of the magmatic record, which often provides the best-preserved manifestation of deeper geodynamic processes in ancient orogenic belts. Models which purport to explain the magmatic record of the Southern Uplands include subduction (Soper, 1986; Thirlwall, 1988, 1982, 1981), break-off (Atherton and Ghani, 2002; Hines et al. 2018; Miles et al. 2016; Neilson et al. 2009; Oliver et al. 2008) transtension (Brown et al. 2008; Miles et al. 2014, 2016) lithospheric delamination (Freeman et al. 1988; O'Reilly et al. 2012) and underthrusting of the continental lithosphere (Miles et al. 2014 and references therein). Table 2.2 outlines the different timings of collisional stages proposed by each geodynamic model (where specified).

Table 2.2: Summary of all geodynamic models proposed for Caledonian igneous bodies across the British – Irish sector of the Caledonides south of the Great Glen Fault. The specific terranes which each model addresses are listed. The stages generally associated with continental collision are noted (e.g., subduction though to underthrusting). Ages or durations for different collisional stages are presented below as per the literature. Where not directly stated but inferred, dates or durations are provided with a question mark (?). Some models refer to but do not specify dates for distinct collisional stages. Abbreviations include MVT = Midland Valley Terrane. GHT = Grampian Highlands Terrane. SUT = Southern Uplands Terrane. NR = not relevant to the specified model.

References	Terranes involved	Subduction	Flat vs steep slab	Slab rollback	Slab break-off	Lithospheric delamination	Continental underthrusting
Thirlwall (1981, 1982, 1988)	MVT, GHT	~410 – 396 Ma	NR	NR	NR	NR	NR
Atherton and Ghani (2002)	GHT	Early-Silurian to ~435 Ma	NR	NR	Not specified	NR	NR
Oliver et al. (2008)	Orogen-wide	Until ~430 Ma	Flat slab *c.*450 – 430 Ma Steeper slab *c.* 430 Ma?	~420 Ma	~400 Ma or ~410 Ma	~400 Ma or ~410 Ma	NR
Nielson et al. (2009)	GHT	Until ~430 Ma?	NR	NR	Not specified	NR	NR
Hines et al. (2018)	SUT	~424 Ma	NR	NR	~430 Ma	NR	NR
Brown et al. (2008)	SUT	~420 Ma	NR	NR	NR	NR	NR
Miles et al. (2016)	Orogen-wide	Until ~420 Ma?	Flat slab between ~455 - 425 Ma?	Before ~430 Ma	~430 Ma	~430 Ma if not sometime before?	NR

2.3.2.1. The subduction model for late-Caledonian magma genesis north of the Southern Uplands Fault

The subduction models of Thirlwall (1988, 1982, 1981) argue that late-Caledonian volcanic and related plutonic rocks north of the Southern Uplands Fault (SUF) exhibit comparable calc-alkaline geochemical signatures with modern continental arcs, reflective of generation during subduction beneath the Laurentian margin. In their models, Iapetus Ocean closure occurred between *c.* 410 – *c.* 396 Ma (Table 2.2).

According to Rb-Sr age data, magmatism within the Grampian Highland Terrane was prevalent between *c.* 424 – 408 Ma, starting with Old Red Sandstone volcanism (*c.* 424 – 415 Ma) followed by intrusives (*c.* 414 – 408 Ma). Magmatism within the Midland Valley Terrane (MVT) overlaps this range, prevalent between *c.* 415 – 410 Ma. Late Caledonian volcanic and plutonic rocks of the Southern Uplands exhibit broadly younger ages and distinct chemistries compared to igneous rocks north of the Southern Uplands Fault (Thirlwall, 1982, 1981). Plutons in the Southern Uplands also exhibit temporal and chemical variations from north – south across the terrane, such as the northern plutons broadly being older *c.* 413 – 407 Ma compared to the southernmost plutons with Rb-Sr emplacement ages of *c.* 398 – 391 Ma (Table 2.1). These plutons are not therefore entirely consistent with a subduction origin (Thirlwall, 1982, 1981). The proximity of some Southern Uplands plutons to the Iapetus suture supports Thirlwall's suggestion that these are unrelated to subduction (Miles, 2013).

Whilst the geochemistry of the late-Caledonian volcanic and plutonic rocks may support a subduction origin (Dewey et al. 2015; Thirlwall, 1988, 1982, 1981), the geochronology of late-Caledonian magmatism in the Midland Valley and Grampian Highlands is not consistent with a subduction mechanism for magma genesis. Thirlwall (1988) proposes that the Iapetus Ocean was closed as late as *c.* 410 – *c.* 396 Ma (Table 2.2). However, other studies, harking back to the work of Watson (1984), argue for the cessation of sedimentation in the accretionary prism at ~420 Ma as a marker of the end of ocean-continent subduction (Brown et al. 2008; Chew and Strachan, 2014; Oliver et al. 2008). If this is the case, and the end of sedimentation does indicate Iapetus closure (Oliver et al. 2008), then all magmatism after *c.* 420 Ma is post-subduction in origin and cannot be related to active subduction (Richards, 2009).

2.3.2.2. Slab break-off models

Atherton and Ghani (2002) were the first to propose that slab break-off following Iapetus closure triggered granite magmatism (Table 2.2; Fig. 2.5 a). In this model, Atherton and Ghani (2002) argued that continental underplating of Baltica beneath Laurentia preceded break-off, which further triggered asthenospheric upwelling and melting of the enriched mantle lithosphere. In turn, they argued for magmatic underplating, intrusion of mafic magmas into the crust, and subsequent crustal melting due to heat advection, leading to the generation of calc-alkaline granitoid magmas (Atherton and Ghani, 2002). They envisaged a laterally consistent break-off depth producing a large, aligned belt of calc-alkaline plutons, over a short time period, and referenced the high Ba-Sr calc-alkaline plutons extending from Donegal through Scotland and into Shetland as compatible with this model**.** This model has become very popular in subsequent literature, highlighted by the work of Neilson et al. (2009) on the northwest of the Grampian Highland Terrane (Table 2.2; Fig. 2.5 b). However, we now understand that the plutons were emplaced over a considerable time period (~40+ Myr). This model also tries to attribute magmatism in different terranes to the same process, and a general critique of slab break-off as a mechanism for magmatism during continental collision is provided in Section 2.3.2.4. Neilson et al. (2009) accounts for both plutonic and volcanic magmatism in the Grampian Highland Terrane, as opposed to Atherton and Ghani, (2002) who only discuss granite pluton genesis. In Neilson et al. (2009), rather than partial melting of the mafic underplate for granite genesis (Atherton and Ghani, 2002), Neilson et al. (2009) argues for continuous crustal underplating and subsequent partial melting of the lower crust to explain protracted intermediate-felsic plutonic and volcanic magmatism (Fig. 2.5 b). The surface expression of break-off is a linear belt of volcanic and plutonic magmatism, mobilised to the upper crust through major faults (Neilson et al. 2009). Surface uplift also accompanies break-off, followed by erosion, deposition and/or extension (Atherton and Ghani, 2002; Davies and Von Blanckenburg, 1995; Garzanti et al. 2018). Mid Silurian – Devonian extensional basins across the orogen are interpreted as representing a surface expression of break off (Atherton and Ghani, 2002). Uplift in response to break-off has been recognised in other collisional orogens such as the European Alps (von Blanckenburg and Davies, 1995b).

A further model includes bi-lateral slab break-off to explain late Caledonian magmatism across the entire Scottish Caledonides and northern England (Table 2.2; Oliver et al. 2008). In their model, Oliver et al. (2008) includes divergent double subduction of the Iapetus slab (i.e., NW below Laurentia and SE below amalgamated peri-Gondwanan terranes and Baltica) from *c.* 450 Ma to *c.* 430 Ma followed by slab rollback at ~420 Ma and bi-lateral break-off and delamination north and south of the suture at ~400 Ma (Table 2.2; Fig. 2.5 c). A shallow slab angle was inferred to account for their proposed 'gap' in magmatism *c.* 450 Ma – 430 Ma (Table 2.2), though it should be noted that this 'gap' is no longer clearly apparent in recent regional data (e.g., Milne et al. 2023).

Break-off at ~400 Ma is identified as the causal mechanism for lithospheric delamination below the Southern Uplands, Midland Valley, Grampian Highlands and the Lakesman Terrane (Oliver et al. 2008). From *c.* 400 Ma removal of the mantle lithosphere above both subducting slabs triggered hot asthenosphere to rise and impinge to the base of the Midland Valley and Southern Uplands continental crust, instigating high temperature metamorphism and partial melting of the lower crust (Fig. 2.5 c). S-type granites originated from these partial melts (e.g., Criffel, Fleet plutons; Oliver et al. 2008)

Miles et al. (2016) propose a version of the post-collisional slab break-off model to explain late Caledonian magmatism in all terranes across the British sector of the Caledonides with a key focus on the Grampian Highlands and Midland Valley Terranes (Table 2.2; Fig. 2.5 d). They argue for collision between Avalonia and Laurentia at *c.* 430 Ma, end of Iapetus subduction at *c.* 420 Ma and accelerated Iapetus slab rollback before slab break-off at *c.* 430 Ma (Miles et al. 2016). Widespread delamination of the lithospheric mantle directly below the suture (Fig. 2.5 d) and 100 km SE below Avalonian crust accompanied Iapetus slab rollback (Miles et al. 2016). Lithospheric delamination triggered magma genesis in their model, but strike-slip faulting is argued to have facilitated emplacement (Miles et al. 2016). They argue that upwelling mafic magmas resulted in formation of lower crustal hot zones from which granite magmas originated via fractional crystallisation and associated crustal melting**.**

2.3.2.3. Regional transtension and other models for magmatism in the Southern Uplands Terrane

Brown et al. (2008) discuss the genesis of the TSS (see Section 2.3.1) within the context of early Devonian regional transtension. In this model, genesis of the TSS occurred after Iapetus closure at ~420 Ma (Table 2.2) and are genetically related to lamprophyres formed during regional transtension *c.* 420 Ma - 400 Ma. Lamprophyre generation is related to extensional tectonics, decompression and melting of the enriched Avalonian lithospheric mantle occurring during regional transtension. It is the heat transfer from lamprophyres into the lower crust and associated crustal melting beneath the prism which triggered genesis of the I- and S-type components of the TSS. Thus, Trans-suture Suite magmas were generated during regional transtension and emplaced during a subsequent transpressional episode (*c*. 400 – 390 Ma).

The most recent geodynamic model for magmatism in the Southern Uplands reconciles ideas from previous models (Atherton and Ghani, 2002; Brown et al. 2008; Miles et al. 2016; Oliver et al. 2008) and combines these with geochronological, geochemical and isotopic data from plutons in the Southern Uplands (Table 2.2). Hines et al. (2018) re-interpret Loch Doon, Carsphairn, Portencorkrie and Newry plutons as members of the Trans-suture Suite and propose multiple geodynamic controls to explain prolonged magmatism between *c.* 430 – 382 Ma in the Southern Uplands, rather than attributing magmatism to one geodynamic trigger (e.g., Atherton and Ghani, 2002).

Hines et al. (2018) argued for collision between peri-Gondwanan terranes and Laurentia to have occurred between *c.* 430 – 424 Ma. They argue for Iapetus slab break-off at ~430 Ma, prior to the end of collision (Table 2.2). Asthenospheric upwelling and depleted lithospheric mantle melting in response to break-off is argued to trigger the onset of magmatism from *c.* 430 Ma. Assimilation of Laurentian components (± deeply-subducted peri-Gondwanan crust*)* into mantle-derived magmas occurred between *c.* 430 – 415 Ma. Hines et al. (2018) then propose post-collisional regional transtension, associated reactivation of lithospheric mantle and development of lower crustal reservoirs from *c.* 415 – 400 Ma, resulting in the formation of a mid – lower crustal batholith. They argued that magmas experienced open system petrogenetic processes such as fractional crystallisation, mixing and contamination (*c.* 400 – 380 Ma) within this batholith prior to high level emplacement between *c.* 414 – 382 Ma (Hines et al. 2018).

Lithospheric delamination is an alternative geodynamic mechanism to which late Caledonian magmas have been attributed. Freeman et al. (1988) proposed delamination of the Avalonian mantle lithosphere from its continental crust prior to underthrusting of the decoupled Avalonian lithospheric mantle below Laurentia**.** O'Reilly et al. (2012) argued for an 'incipient delamination' model, in which orogen-scale late Caledonian felsic and mafic magmatism is attributed to changes in applied vertical stress due to continental lithospheric shortening following Iapetus closure.

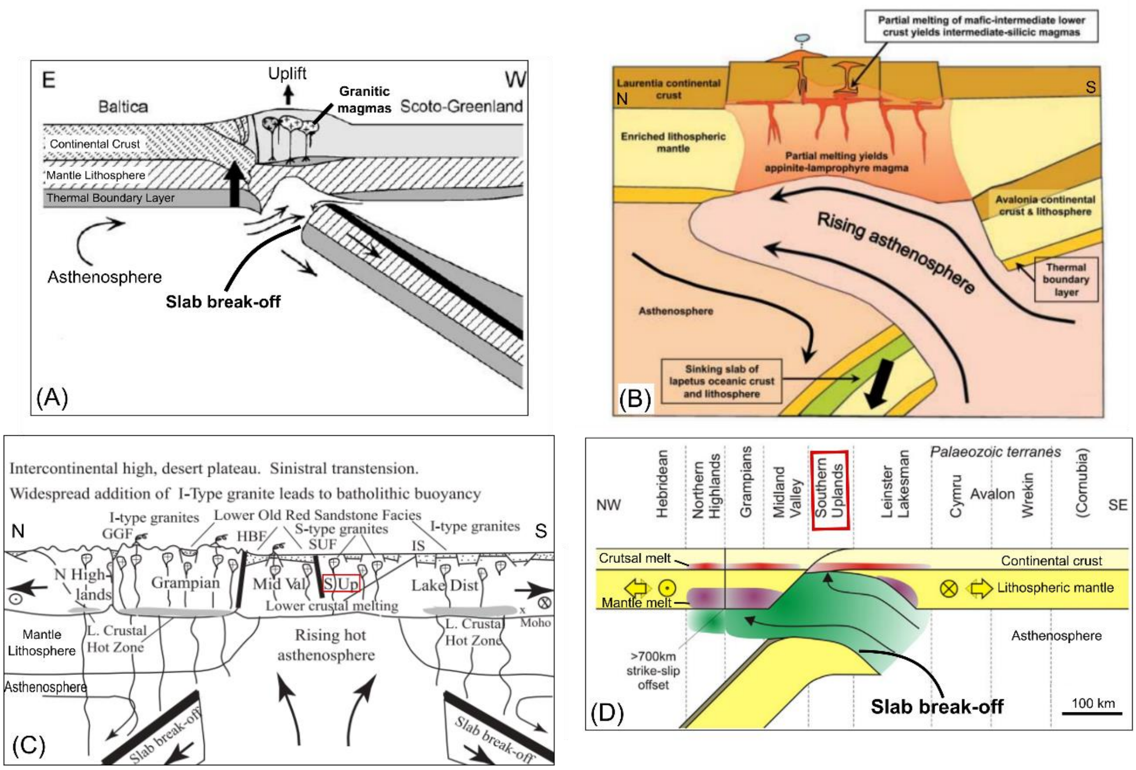

Figure 2.5: Geodynamic models emphasising the role of slab break-off in triggering Caledonian magmatism across the Grampian Highlands, Midland Valley and Southern Uplands terrane. Models include (A) Atherton and Ghani (2002). (B) Neilson et al. (2009). (C) Oliver et al. (2008) suggesting break-off at ~400 Ma and (D) Miles et al. (2016) proposing break-off at ~430 Ma. Note that no model is shown to scale.

2.3.2.4. The need for a consistent geodynamic model

A range of inconsistencies within and between these geodynamic models is outlined in Table 2.3. In very broad terms, some models argue that late Caledonian magmatism south of the Great Glen Fault is the product of subduction and the very early stages of collision (Thirlwall, 1988, 1982, 1981) whereas others propose that magma genesis is largely related to regional transtension (Brown et al. 2008). Several models attribute magmatism entirely to slab break-off (Table 2.3) but each propose different timings (Table 2.2). For example, Hines et al. (2018) and Miles et al. (2016) propose early break-off at ~430 Ma in contrast to Oliver et al. (2008) who argued for later bi-lateral break-off at ~410 Ma or ~400 Ma (Table 2.2). Break-off is globally not considered a significant geodynamic trigger for post-collisional magmatism (Freeburn et al. 2017) despite its apparent popularity in recent Scottish literature. In global collisional zones where slab breakoff has been proposed, such as in the European Alps, magmatism is characterised by a spatially constrained linear surface expression (e.g., Periadriatic intrusions) and a pronounced age peak in magmatism (~33 – 29 Ma; von Blanckenburg and Davies, 1995b). This contrasts several breakoff models proposed for Caledonian magmatism, attributing orogen-wide magmatism over long timescales entirely to slab breakoff (e.g., Oliver et al. 2008). Additionally, some existing models discuss data on quite local terms, related to singular terranes or magmatic suites, as opposed to considering the entire orogen as part of a broader continental arc system south of the Great Glen Fault.

These considerable inconsistencies (Table 2.3) are likely to reflect our ever-growing body of geological knowledge and a need to refine earlier ideas, but it also reflects more fundamentally how we rely on the magmatic record and its interpretation to help us reconstruct geodynamic processes in ancient orogenic belts. As Lawrence et al. (2023) and Milne et al. (2023) highlight, the interpretation of the true meaning of purported emplacement ages of magmatic bodies in such belts can be subject to biases and over-interpretation of limited data.

Table 2.3: Summary of key issues and inconsistencies of the geodynamic models outlined in Table 2.2. [1] Watson (1984) [2] Lancaster et al. (2017) [3] Strachan et al. (2020) [4] Chew et al. (2010) [5] Trewin (2003) [6] Miles et al. (2014) [7] Freeburn et al. (2017) [8] Garzanti et al. (2018) [9] van Hunen and Allen (2011) [10] Andrews and Billen (2009) [11] Maury et al. (2000). See Table 2.2 for abbreviation definitions.

References	Terranes considered	Geodynamic mechanism(s) for late Caledonian magmatism	Critique
Thirlwall (1981, 1982, 1988)	GHT, MVT	Active subduction	• Iapetus closure between ~410 – 396 Ma is inconsistent with widely accepted closure at ~420 Ma[1]. Therefore, the proposed subduction-related magmatism from ~424 – 408 Ma would instead be considered as post-subduction in nature rather than arc-related.
Atherton and Ghani (2002)	NHT, GHT	Slab break-off	• Attributes late Caledonian magmatism to one geodynamic mechanism, that is break-off. Slab break-off is now recognised as a less significant trigger for post-collisional magmatism [7, 8]. • Recent U-Pb geochronology data for some plutons (e.g., Graven, emplacement at *c.* 440 Ma[2]) do not support a break-off origin (~430 Ma). • This model refers to break-off and magmatism within the GHT in the context of the Scandian event, however the GHT is thought to be 100's of km further south during the collision *and* thus would be expected to be unaffected by Scandian. • Their model does not recognise magma storage in crust prior to emplacement.
Oliver et al. (2008)	Orogen-wide	Bi-lateral slab break-off	• There are inconsistencies in dates between text and geodynamic figures e.g., proposing break-off at ~410 Ma in text but ~400 Ma in the geodynamic figure. • The widely accepted date for onset of Scandian collision is *c.*437 Ma[3]. Therefore, it would not be possible to have subduction starting at ~430 Ma if collision occurred ~7 Ma prior. • Obduction of Ballantrae ophiolite at *c.* 478 Ma[4,5] probably reflects onset of subduction initiation of peri-Gondwanan terranes beneath Laurentia, thus raises questions about the validity of ~430 Ma for onset of subduction proposed here. • Geochronology of several plutons does not support slab break-off at ~400 Ma. For example, U-Pb zircon ages of ~415 – 408 Ma[6] for Criffel would imply emplacement >~8 Ma before the proposed causal mechanism that is break-off.

			• No lower crustal hot zones are depicted below the Southern Uplands to account for I-type affinities of plutons or ages >400 Ma recorded by some plutons.
Brown et al. (2008)	SUT	Regional transtension	• Argue for emplacement of the Trans-suture Suite towards the end of or quickly following regional transtension (*c.* 420 – 400 Ma) but some pluton dates are considerably older than *c.* 400 Ma. For example, the outer granite zone of the Fleet pluton gave a U-Pb age of 410 Ma[6].
Miles et al. (2016)	Orogen-wide, but mainly GHT, SUT	Slab break-off	• Their model contains some temporal inconsistencies as it proposes slab 'peel-back' and break-off after Iapetus closure at ~420 Ma but suggests break-off occurred at *c.* 430 Ma. • They also argue for collision, 'peel-back' and break-off at ~430 Ma. Active subduction was ongoing until ~420 Ma therefore these timescales appear to be unrealistic [8, 9 10].
Nielson et al. (2009)	GHT	Slab break-off	• They attribute all post-collisional volcanic and plutonic magmatism to slab break-off [7, 8]. • Their model portrays unrealistic subducting slab angles and asthenospheric upwelling.
Hines et al. (2018)	SUT	Slab break-off and regional transtension	• Proposes early break-off at ~430 Ma, thus break-off prior to end of subduction (*c.* 424 Ma) which is inconsistent with recent work[9, 11] indicating that break-off occurs millions of years following the onset of continental collision.

2.4. Study areas

To re-iterate, there is a strong need for modern petrographic, geochronological and geochemical analysis for the Carsphairn pluton, Black Stockarton Moor subvolcanic complex and Cheviot pluton, hence their inclusion in this study. Obtaining new data will allow a complete timeline of late Caledonian magmatism (e.g., from onset of magmatism to emplacement) to be established across the Southern Uplands which in turn will enable discussion of a new geodynamic interpretation for collisional magmatism in this region. Addressing data gaps in the select bodies and subvolcanic complex will also aid in reconciling existing geodynamic models (see Section 2.3.2).

The Carsphairn pluton (11 km^2) located to the northwest of the Southern Uplands in the northern belt (Fig. 2.6) has one previously published Rb-Sr biotite - whole rock emplacement age of 418.6 ± 4.1 Ma (Table 2.1, Thirlwall, 1988). The pluton was intruded into the turbidite, conglomerate and siltstone tracts of the Kircolm Formation of the Barrhill Group (Leggett et al. 1979; Stone et al. 2012). It is compositionally zoned (Deer, 1935) from a less evolved quartz diorite outer zone to a more evolved granite centre (Hines et al. 2018). Previous whole rock and mineral geochemical studies (Deer, 1935; Tindle et al. 1988) identified fractional crystallisation and hybridisation as important processes in pluton genesis and evolution. The models of Deer (1935) and Tindle et al. (1988) differ in that Deer (1935) interpreted Carsphairn evolution within the context of successive phases of emplacement, hybridisation and fractional crystallisation. Instead, Tindle et al. (1988) argues against a simple 'hybridisation' model envisaging Carsphairn evolution at different crustal levels by more complex processes, rather than only in-situ. One sample was collected from each zone for this study (Fig. 2.6).

The BSM subvolcanic complex, located in the central belt, intrudes >100 km^2 of the sandstone, mudstone and siltstone turbidite successions of the Ross and Carghidown Formations of the Hawick Group (Trewin, 2003; Waldron et al. 2008). It comprises of at least three magmatic phases, encompassing NW-SE and NE-SW striking basic to intermediate porphyrite dyke swarms, mafic dykes, granodiorite sheets, stocks, breccia pipes and the adjacent Criffel and Bengairn plutonic complexes (Fig. 2.6). Each phase was originally distinguished using field relationships and petrography (Brown et al. 1979b; Leake and Cooper, 1983). The minor intrusions could be of a similar age (Table 2.1) to the nearby Criffel pluton (Brown et al. 1979b; Halliday et al. 1980; Leake and Cooper, 1983; Miles et al. 2014). An eastward shift in magmatism at BSM from a subvolcanic to plutonic setting has been argued to be accompanied by variations in magma sources, water content and petrogenetic processes over time (Leake and Cooper, 1983). Evidence of porphyry-type copper mineralisation during the 1970s - 1990s BGS Mineral Reconnaissance Programme supports shallow level crustal emplacement of the complex (Brown et al. 1979b; Leake and Cooper, 1983).Three samples were collected in total, two from the phase 1 quartz diorite dykes and sheets and one from the phase 2 quartz diorite dykes (Fig. 2.6).

The Bengairn pluton (50 km^2), located East of Kirkcudbright in the southern belt of the Southern Uplands Terrane(Fig. 2.6), is thought to post-date the first phase of dykes in the BSM complex, marking the end of the first igneous phase and the earliest phase of plutonic activity at BSM (Leake and Cooper, 1983). The pluton, like the BSM complex, was intruded into the turbidite successions of the Ross and Carghidown Formations of the Hawick Group (Trewin, 2003; Waldron et al. 2008). Leake and Cooper (1983) depict the Criffel-Dalbeattie pluton cutting the E margin of Bengairn, whereas Miles et al. (2014) considers the Criffel-Dalbeattie and Bengairn plutons as one complex, classing Bengairn as part of the outermost zone of Criffel. This body is compositionally zoned from a quartz diorite marginal zone to a granodiorite core (Hines et al. 2018; Leake and Cooper, 1983). Early studies explored field relationships between the minor intrusions and the Bengairn pluton, indicating high levels of emplacement (Leake and Cooper, 1983). One quartz diorite sample was collected for this study (Fig. 2.6).

The Cheviot complex was emplaced into tracts of greywacke sandstone, conglomerates, shale, siltstone and mudstone of the mid – upper Silurian Riccarton Group of the Southern Belt (Stone et al. 2012; Trewin, 2003; Woodcock and Strachan, 2012). Cheviot volcanic rocks have three previous Rb-Sr ages of 399 ± 8 Ma (whole-rock plagioclase, n = 2), 388 ± 11 Ma (whole-rock – clinopyroxene, n = 2) and 404 ± 4 Ma (biotite, n = 2) (Thirlwall, 1988). The Cheviot pluton Rb – Sr ages from a combination of whole-rock, biotite, augite and feldspar mineral analysis range from 402.1 ± 5.5 Ma – 406.4 ± 5.2 Ma (Thirlwall, 1988). Located to the SE of the Southern Uplands, this pluton, exposed over ~70 km^2, was emplaced into the Cheviot volcanic formation extending over >700 km^2 (Fig. 2.6). A previous study (Al-

Hafdh, 1985) concluded that the igneous rocks were sourced from a long-lived deeper magma chamber – akin to modern deep crustal hot zone hypotheses (Annen et al. 2006) – prior to emplacement at shallow crustal levels. Other studies used mapping, petrography, geophysics and geochemical analysis to investigate the magmatic sources and emplacement mechanisms of the pluton (Al-Hafdh, 1985; Jhingran and Tomkeieff, 1942; Lee, 1982; Robson and Green, 1979). The Cheviot pluton is compositionally zoned from marginal quartz diorite to a monzodiorite - granodiorite centre (Fig. 2.6; Al-Hafdh, 1985; Hines et al. 2018). Samples were collected from the 'Granophyric' and 'Standrop' varieties of Jhingran and Tomkeieff (1942). These were unified and classed as one 'Standrop' facies by Al-Hafdh (1985) (Fig. 2.6).

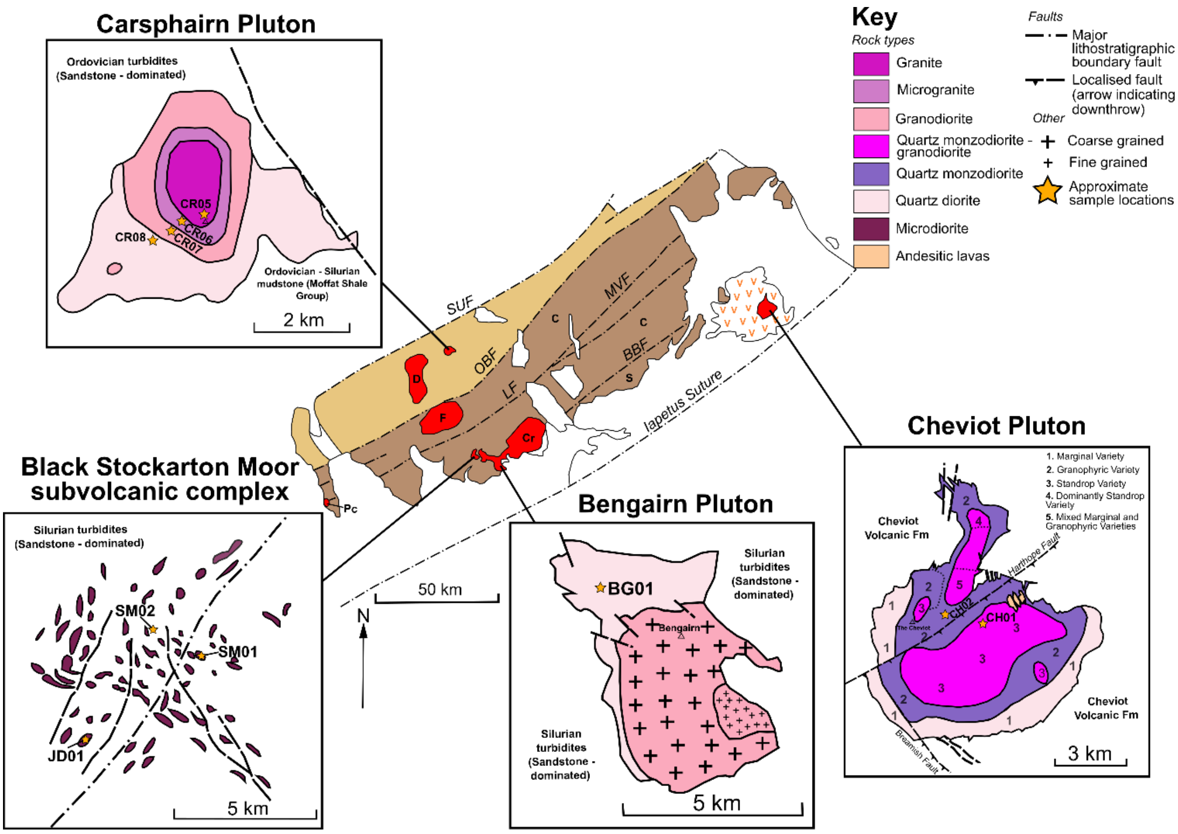

Figure 2.6: Geological map of the Northern, Central and Southern Belts of the Southern Uplands Terrane with insets outlining the rock type, key faults and approximate sample locations for each pluton and complex analysed in this study. See Figure 2.3 for the Southern Uplands Terrane map key. Adapted from Al Hafdh (1985); Hines et al. (2018); Jhingran and Tomkeieff (1942) and Stone et al. (2012). Reproduced in Gemmell et al. (2025). See Table 4.1 for grid references for the samples collected in this study.

2.5. Previous methods

The Carsphairn pluton and Cheviot complex have previous Rb-Sr whole-rock and/or mineral emplacement dates (Thirlwall, 1988). The BSM subvolcanic complex and the Bengairn pluton were undated prior to this study (Table 2.1). Whilst Rb-Sr whole-rock and mineral dating can provide useful emplacement age data (Nebel, 2013), there are a lot of assumptions associated with this method. Firstly, Rb-Sr dating assumes that the age produced represents emplacement, supported by its low closure temperature (300 – 500^{o}C; Nebel, 2013). It also assumes that there has been no modification of whole-rock or mineral Rb-Sr concentrations since initial crystallisation, when in fact the Rb-Sr dating system is particularly vulnerable to alteration and/or thermal resetting (Miles et al. 2014). The Rb-Sr method is also controlled by isochrons (Nebel, 2013), thus involves introducing subjectivity through selecting and removing anomalous data points. It can only be applied to groundmass or late-stage crystallising minerals in volcanic rocks (Nebel, 2013). A major limitation of Rb-Sr dating is that it cannot constrain pre-emplacement magmatic history (Table 2.1) (Archibald et al. 2022, 2021; Miles et al. 2016; Milne et al. 2023; Oliver et al. 2008). Existing Rb-Sr age (Table 2.1) data implies that Carsphairn and Cheviot were emplaced prior to the Acadian Orogeny (from *c.* 404 Ma), thus both bodies may have been susceptible to alteration and disruption of the Rb-Sr system by local fluid flow during this deformational event. However, it is expected that Thirlwall (1988) may have been more cautious and thorough during sample selection to account for potential alteration.

The U-Pb dating system is more robust as it is not susceptible to mineral reheating or resetting by alteration (Oliver et al. 2008). U-Pb dating of zircons can record the total duration of magmatism from deeper in a crustal hot zone through to emplacement (Miles and Woodcock, 2018; Milne et al. 2023) and can therefore be used to better understand the geodynamics and crustal stress state during the later stages of continental collision. U-Pb zircon dating has been applied to other plutons outwith this study in the Southern Uplands, however the data coverage is patchy (Table 2.1, Hines et al. 2018; Miles et al. 2014; Oliver et al. 2008). Hines et al. (2018) used in-situ U-Pb LA-ICP-MS zircon dating to identify up to ~30 Ma of pre-emplacement growth in the Loch Doon pluton. They also re-interpreted previous U-Pb secondary ionisation mass spectrometry (SIMS) ages from Miles et al. (2014) for the Criffel and Fleet plutons and U-Pb sensitive high-resolution ion microprobe

(SHRIMP II) age data for the Portencorkrie pluton (Oliver et al. 2008) as containing evidence of protracted zircon histories from growth interpreted as antecrystic through to emplacement. Hines et al. (2018) used this total duration of magmatism data to better constrain the geodynamic and tectonic setting during genesis and emplacement of these bodies. SHRIMP methods are typically more precise as they can target small zones on a zircon grain (Kröner et al. 2014). The typical precision for SIMS is ~1 – 2% and it is suitable for small volume analysis of smaller overgrowths. LA-ICP-MS, the method of choice for this study, has an individual data point precision of ~1 – 2% (Schaltegger et al. 2015). A 1 – 2% precision on individual spots that for example, are ~400 Myr old (Table 2.1), equates to an age error of ± 4 or ± 8 Myr, thus enabling broad identification of differences in zircon growth ages and general patterns of emplacement over longer timescales (e.g., ~5 – 20 Ma).This study applies U-Pb LA-ICP-MS zircon geochronology to constrain the total duration of magmatism from onset to emplacement at Carsphairn, Cheviot and BSM which in turn will be used to address the regional geodynamic debates outlined in Section 2.3.2. Whilst LA-ICP-MS is not the most precise method, it can acquire large datasets and is cost-effective relative to the alternative methods, ultimately driving its use in this study.

2.6. Lower crustal hot zone framework

2.6.1. Evolution of the lower crustal hot zone concept

This study will explore the lower crustal hot zone (LCHZ) concept because it is directly relevant to each of the plutons and complexes explored in this study. The concept of a lower crustal hot zone is now a geologically well-established principal (Annen et al. 2006; Cashman et al. 2017; Chiaradia, 2022; Hildreth and Moorbath, 1988; Petford and Gallagher, 2001; Richards, 2021)**.** Building on the ideas of the melting, assimilation, storage and homogenisation (MASH) model, Annen et al. (2006) first defined a lower crustal hot zone as a site where mantle-sourced basaltic magma was incrementally injected, and subsequent melt was generated (Fig. 2.7). Basaltic magmas are emplaced as sills at different depths. Newly added magmas undergo fractionation, generating intermediate – felsic melts which ascend from the lower crustal hot zone to higher level shallow reservoirs (Fig. 2.7). Crustal partial melts generated at different levels of the hot zone, might mix with more evolved residual melts*.* Additional processes including further fractionation of evolved magmas, mingling and assimilation of surrounding upper crustal rocks are expected to accompany complex processes within a lower crustal hot zone. Magmas generated in this LCHZ setting are compositionally and texturally heterogeneous (Annen et al. 2006). It is key to note that when referring to a lower crustal hot zone, this study is not referring to just one hot zone, rather multiple hot zones over a variety of depths (Fig. 2.7; Annen et al. 2006).

This LCHZ concept relates somewhat to early ideas around granite genesis, specifically to Chappel and White's (1974) original subdivision of granites into I- and S-types based on different source rock compositions of the Berridale – Kosciuszko granites of the Lachlan Fold Belt region, Australia. They proposed that S-type granites originated from partial melting of a sedimentary or "supracrustal" (i.e., sedimentary rocks deposited on the crust) source and that I-type granites were sourced from partial melting of an igneous or "intracrustal" source (i.e., igneous rocks within the crust). Their I-type granites are especially interesting from a lower crustal hot zone perspective. Within this group are granitic compositions ranging from felsic to mafic compositions, potentially implying the need for multiple stages of intracrustal processing to account for the compositional spectrum of granites. Chappell and White (2001) recognised that I-type source rocks were broadly homogeneous, thus likely originated from deeper levels dominated by more primitive material with limited supracrustal input. This deeper level source idea was supported by the lack of crustal enclaves observed in I-type granites (Chappell and White, 2001). Ultimately, the work of Chappell and White (1974; 1988; 2001) indicates that granites in the Lachlan Fold Belt do not represent one batch of melt, rather involve multiple stages of crustal processing to produce granites we see emplaced at the surface today (Pichavant et al. 2024). Their classification is mainly focused on temperatures required for source rock melting, thus does not consider the role or involvement of mantle-derived melts in granite genesis.

By the 1990s, the idea of a LCHZ although not yet clearly defined, was being explored. Hildreth and Moorbath (1988) introduced the concept of zones of melting, assimilation, storage and homogenisation (MASH) in the lower crust or at the crust - mantle boundary (see Richards, 2021; Figure 1). They proposed that incremental addition of basaltic magmas from the mantle wedge triggered small-scale partial melting of the crust within this MASH zone (Hildreth and Moorbath, 1988). Intermediate magma compositions are reached through fractionation of basaltic magmas, mixing with crustal partial melts and new additions of basaltic magma and incorporation of surrounding wall-rock (Hildreth and Moorbath, 1988; Richards, 2021).These intermediate magmas upwell to and accumulate at shallower crustal depths due to their buoyant nature and form a series of magma reservoirs in the mid - upper crust. They proposed that this MASH zone was structured as a series of mushy segregated intrusions, ponds, dykes, sills and small magma chambers (Hildreth and Moorbath, 1988).

A recent study by Cashman et al. (2017) exploring the concept of transcrustal magmatic systems (TCMS), supports the lower crustal hot zone concept (Annen et al. 2006). They support those magmatic processes, rather than occurring in individual shallow magma chambers, occur at varying levels throughout the crust (Fig. 2.7). At lower crustal depths in the TCMS, processes including fractionation, compaction and separation of basic cumulates from more silicic melts triggered upwelling and storage of evolved melts at mid to upper-crustal levels (Fig. 2.7). At mid-crustal levels, melts are exposed to an open-system environment causing reservoirs to rapidly ascend to upper crustal magma chambers. Within a transcrustal magma system mid-crustal recharge magmas can contain antecrysts derived from earlier magma pulses throughout the system, which may travel to the upper crustal reservoirs upon destabilisation of mid-crustal melt pockets (Miller et al. 2007; Walker et al. 2007). A TCMS is characterised by a crystal mush state (Fig. 2.7), with mushes at the temperature of or at a temperature slightly higher than the solidus temperature. This model argues that the incremental addition of mantle-derived basaltic magma triggers crustal magmatic activity (Cashman et al. 2017).

To clarify for grains referred to as ‘antecrysts’ or ‘antecrystic’ throughout this thesis, I am following the understanding of others (Miller et al. 2007; Walker et al. 2007) that antecrysts are magmatic crystals grown in an earlier pulse of magma and broadly originate from the same long-lived magmatic system as the final pluton in which they are hosted. In this study, I do not address the origin of antecrysts i.e., whether a crystal is scavenged and incorporated from a fully crystalline prior intrusion or from a partially molten crystal mush (Charlier et al. 2005), only that they do not originate from entirely unrelated rock suites (e.g., old sedimentary or metamorphic host rocks through which the magma once rose and interacted with) (Walker et al. 2007).

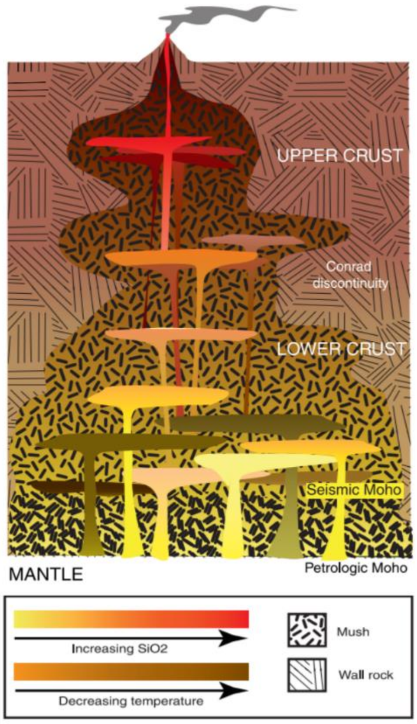

Figure 2.7: Transcrustal magma system (not to scale). Magma is emplaced as sills at different depths throughout the crust. Antecrystic zircons from earlier magma injections are expected to be integrated into different intrusions or remobilised with newly added magma batches as magmas ascend through the crust. Xenocrysts are incorporated through wall-rock assimilation (Miller et al. 2007). Adapted from Cashman et al. (2017).

2.6.2. Controls on lower crustal hot zone development

The development of a lower crustal hot zone is dependent on the tectonic setting and crustal stress state (Chaussard and Amelung, 2014; Chiaradia, 2022; Richards, 2021). For example, thick arc settings in compression favour the development of lower crustal hot zones (Chiaradia, 2022) because compressional settings typically supress upwelling of mantle melts, favour horizontal fracture formation, associated sill emplacement (Fig. 2.7) and the accumulation of hybrid magmas at depth (>20 km according to Chiaradia, 2022) (Annen et al. 2006; Chiaradia, 2022, 2014; Hildreth and Moorbath, 1988; Richards, 2021). Volcanic output in compressional settings is typically reduced (Tibaldi, 2008) but can occur if magmas at depth escape to upper crustal levels due to high pressure conditions (Richards, 2021).

In contrast, short periods of transpression can trigger strike-slip faulting which typically contains localised zones of crustal extension, thus promoting the development of vertical ascent pathways for hot zone magmas to travel to higher crustal levels (e.g., < ~20 km) (Chaussard and Amelung, 2014; Chiaradia, 2022; Chiaradia and Caricchi, 2017). Transpressional settings favour plutonism (e.g., batholith formation) over volcanism (see Richards, 2021 and refs within) Transpressional settings typically occur at the end of an orogenic cycle at which point the compressive force becomes less important. Uplift and decompression follows the compressional episode and enables melt to be remobilised and emplaced as batholiths and plutons in the crust (Richards, 2021). Extensional settings are thought to promote volcanism via magma ascent through vertical discontinuities (Tibaldi, 2008). Plutonism is not favoured in such settings (Richards, 2021). Lower crustal hot zone development and crustal emplacement are indeed complex (Tibaldi, 2008) and factors such as magma composition (i.e., density) regional tectonic setting (e.g., contraction vs transpression) and localised structures should be considered as important controls when investigating volcanism and plutonic activity in continental arc settings (Chaussard and Amelung, 2014; Richards, 2021; Tibaldi, 2008).

2.6.3. Indications of LCHZ development beneath the Southern Uplands

A limited number of recent studies applied the MASH zone (Hildreth and Moorbath, 1988), lower crustal hot zone (Annen et al. 2006) and transcrustal magma system (Cashman et al. 2017) concepts to late Caledonian magmatism across Britian and Ireland (Archibald et al. 2022; Archibald and Murphy, 2021; Miles and Woodcock, 2018; Woodcock et al. 2019). The LCHZ concept has previously been applied, although not in great detail, to the Northern Highlands Terrane (Milne et al. 2023; Oliver et al. 2008), the Grampian Highlands Terrane (Clemens et al. 2009) and the Southern Uplands Terraneof Scotland (Hines et al. 2018; Miles et al. 2014, 2016), but it is clearly a concept that is globally identifiable (e.g., Mount St Helens, Rainer and Adams, Flinders and Shen, 2017; e.g., Nisyros volcano,Klaver et al. 2018) and therefore may well have occurred in Scotland during Iapetus closure. The concept is appealing in terms of explaining the patterns of age, location, chemistry, and ore-forming potential of magmatism during subduction and collision. The lower crustal hot zone concept is relevant to the Southern Uplands as recent studies have recognised antecrystic zircon growth in some Southern Upland plutons (see Section 2.5; Hines et al. 2018; Miles et al. 2014) interpreting these as zircons that have grown over a prolonged period. Protracted zircon histories can be interpreted within the context of a LCHZ (Annen et al. 2006; Cashman et al. 2017). Whilst antecrystic zircons have been identified in Southern Upland plutons, their relationship to lower crustal hot zones and indeed, their implications for the wider geodynamics, has not been fully investigated. This review demonstrates the need for additional geological data from specific localities across the Southern Uplands of Scotland in order to gain a more detailed understanding of magmatism across the region.

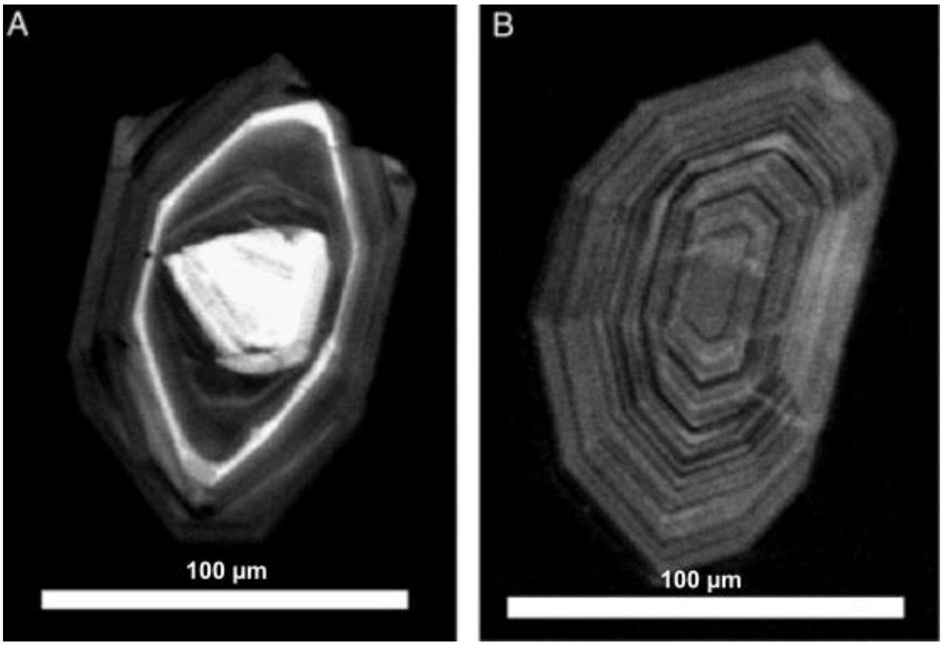

Figure 2.8: Representative cathodoluminescence images of zircons hosted in the Cathedral Peak granodiorite, Sierra Nevada, California, obtained and adapted from Miller et al. 2007 to highlight zircons displaying protracted growth stages vs continuous growth. (A) Zircon grain containing textural evidence of multiple stages of growth, including a distinct bright core (xenocrystic or antecrystic) with variably concentrically zoned overgrowths, implying protracted growth. (B) Zircon grain with consistent concentric zoning from the core – outermost part of grain and no textural evidence of multiple growth stages (e.g., xenocrystic or antecrystic core), implying relatively continuous growth in magma of a consistent chemistry.

3. Methodology

3.1. Sample selection and optical microscopy

Prior to selecting exact sample locations, detailed review of previous geochronological studies was undertaken to identify data gaps in the geochronology of the Caledonian intrusions in the Southern Uplands of Scotland. The Carsphairn pluton, Black Stockarton Moor subvolcanic complex and the Cheviot pluton were the three sites that had no previous geochronological data (e.g., BSM) or lacked modern geochronological data (e.g., Carsphairn, Cheviot). Following identification of areas of interest, previous studies and geological maps were reviewed to better understand the field relationships and the number of facies for each body and complex. The aim was to collect a sample from all the different mapped facies at each locality as determined by field relationships, to determine the total durations of magmatism at each body and its variability within and between each of the study areas.

Sample locations were selected using a combination of previous Mineral Reconnaissance Reports (MRR) and preliminary studies (e.g., Leake and Cooper, 1983) in addition to the BGS maps portal, DigiMap Geology, Ariel Imagery, Google Maps and Google Earth imagery. Such resources were used to identify exposed areas with good potential for medium to coarse-grained igneous rocks yielding zircons. Samples were collected for U-Pb zircon geochronology on October 17th 2022 from the BSM complex and Bengairn pluton, April 19th and May 15th 2023 from the Carsphairn pluton and April 20th 2023 from the Cheviot pluton. Four samples from across the three mapped magmatic phases were obtained from BSM (JD-01, SM-01, SM-02), one sample from Bengairn (BG-01) and four samples from Carsphairn (CR-05 – 08), one from each of the mapped zones of the pluton (Fig. 2.6).Two samples were collected from the Cheviot pluton, one from the ‘Standrop’ facies (CH-01) and another from the ‘Granophyric’ facies (CH-02) of (Jhingran and Tomkeieff, 1942).

Thin sections were made at the University of Glasgow for all field-collected samples using standard procedures. Samples were characterised using a basic transmitted light (TL) optical microscope to constrain the primary mineralogy, alteration mineralogy and textural characteristics. Samples exhibiting potential mineralisation were characterised using the Zeiss Axio Imager.M2m microscope. See section 4.1. for a detailed discussion on the petrography of each sample.

3.2. Zircon separation and imagery

3.2.1. Rock crushing

Rock crushing of all samples was completed at the University of Glasgow, in preparation for further SEM and laser ablation inductively - coupled plasma mass spectrometry (LA-ICP-MS) analysis. The same standard procedure was followed for all samples. All equipment was thoroughly cleaned between samples. Samples were sawn to remove weathered surfaces and where necessary, were broken into smaller fragments using the hydraulic splitter. Each sample was passed through the rock crusher 5 times, with the crushing plates spaced at 5 different distances for each run to produce the largest 500 µm fraction possible. For the first, second and third run, plates were spaced at 15 mm, 10 mm and 5 mm apart. For the final two passes, plates were spaced 2 mm and 0.5 - 1 mm apart. Between each run, crushed material was sieved through the < 1 mm, then < 500 µm and < 63 µm sieves. The > 1 mm, the < 1 mm but > 500 µm and the < 63 µm fractions were bagged and labelled after sieving. After crushing, the < 500 µm fractions remained in a metal tray in preparation for washing. For samples where there were small volumes of < 500 µm fraction remaining after crushing (e.g., CG23-CR-07), a pulveriser was used. Samples were then again passed through the sieves. Following crushing and sieving, the < 500 µm fraction of each sample was passed through a shaking table to wash and divide grains into the least dense and most dense fractions. A table vibration setting of 25 - 40 was used across samples. Once washed and density-separated, each density pot was drained, poured into a metal tray and placed in the oven to dry for approximately 48 - 72 hours. Once dry, all pots for each sample were bagged and labelled. Pots 1 and 2 (most dense) were used for further analysis.

3.2.2. Magnetics and heavy liquid separation

Following crushing and washing, pots 1 and 2 were combined for each sample and material was passed through a vertical magnetic separator to remove highly magnetic material. The remaining non-magnetic fraction was separated further using lithium heteropolytungstate (LST), a heavy liquid with a density of 2.8 g/mL. Once thoroughly mixed and left to separate, grains with a density > 2.8 g/mL that accumulated at the base of separation funnel, were decanted, thoroughly washed with deionised (DI) water and placed under a heat lamp to dry. After LST separation, grains were passed through a horizontal magnetic separator to ensure strongly magnetic minerals were removed. Non-magnetics were further separated in diiodomethane (DIM), a heavy liquid with a density of 3.32 g/mL. Once carefully mixed and left to separate, remaining grains with a density > 3.32 g/mL (e.g., zircons) were decanted, thoroughly washed with acetone and placed under the heat lamp to dry. The same process was followed for grains <3.32 g/mL.

3.2.3. Zircon picking and mounting

DIM fractions were examined under a binocular optical microscope to determine the abundance of zircon in each sample. Where possible, approx. 100 – 120 zircons were hand-picked into a grid-like pattern within a 25 mm circular mould outline onto a glass slide containing double-sided tape. Moulds were then placed onto the double-sided tape over the zircon grids and were mounted in epoxy and left for at least 48 hours to cure. The rationale behind picking and analysing such a high number of zircons for each sample, where possible, included (1) to ensure there would still be enough grains to analyse if any were lost during mounting, grinding or polishing and (2) to enable possible characterisation of the total durations of magmatism in each sample and for each pluton and intrusion rather than focusing soley on emplacement-related growth.

3.2.4. Grinding and polishing

Once cured, the zircons were ground using 2500 – 1200 grade grit paper and polished using 3 µm diamond paste followed by 1 µm corundum paste to achieve a smooth surface. After grinding and polishing, zircons were observed in TL and reflected light (RL) using a standard binocular microscope to ensure sufficient removal of grinding-related scratches and a well-polished finish within grains in preparation for Scanning Electron Microscopy-Cathodoluminescence (SEM-CL) imaging. A few zircons were lost during grinding and polishing stages for each sample.

3.2.5. Scanning electron microscopy – cathodoluminescence (SEM-CL) imagery

Zircon grains were imaged using a cathodoluminescence (CL) detector attached to the FEI Quanta 200F environmental scanning electron microscope at the Geoanalytical Electron Microscopy and Spectroscopy (GEMS) laboratory at the

University of Glasgow. Mounts were carbon coated in preparation for analysis. The CL images were captured to show the micro-scale textural characteristics in zircon grains in preparation for laser ablation. Secondary electron (SE) images were also obtained to constrain grain topography. SEM settings included a spot size of 3, a high voltage (HV) of 15.0kV, a working distance of approx. 14 – 15.5 mm and a scan speed of 20. Carbon coating was removed using 3 µm AL_2O_3 polish on short nap paper.

3.2.6. Laser ablation spot selection and referencing

All CL images for each sample were transferred to Microsoft PowerPoint slides, where 30 µm spots were constructed and positioned in well-developed continuous zoned areas within grains, avoiding fractures and/or inclusions. Once completed for all samples, copper stickers were added to the mounts and used as reference markers for laser ablation. Markers and spots were referenced using the points list function on the Zeiss Axio Imager.M2m microscope. A consistent naming convention, outlining the grain number, spot number and type of analysis (e.g., U-Pb) was used in preparation for laser analysis. The points list included the x, y coordinates for spots within each sample and was exported as a .csv file and imported into the laser

3.3. Laser ablation inductively coupled mass spectrometry (LA-ICP-MS)

3.3.1. Acquisition and instrument parameters

Grains of interest were lasered using the RESOlution laser of Australian Scientific Instruments at the University of Glasgow. Acquisition parameters are outlined in Table 3.1. Material generated from this ablation was carried in an Ar gas medium and collected in a Thermo iCAP-RQ single collector mass spectrometer in the Thermochronology laboratory (Milne et al. 2023) where select isotope concentrations were measured (Table 3.1).

Table 3.1: Summary of LA-ICP-MS analysis parameters for U-Pb analysis of zircons.

Acquisition parameters	
Spot size	30 µm
Ablation time	30 seconds
Fluence	3.3 J/cm^2
Resolution time	10 Hz
Isotope channels measured	^{29}Si, ^{200}Hg, ^{204}Pb, ^{206}Pb, ^{207}Pb, ^{208}Pb, ^{232}Th, ^{235}U, ^{238}U

3.3.2. Analytical process and reference materials

GeoStar software of Norris Scientific was used to navigate between and within samples on the laser. Samples were placed into the sample holder, then placed into the cell and loaded into the GeoStar software. Once in the cell, a live video feed of all mounts was displayed, enabling easy navigation within and between samples. Points lists were imported, and spot locations revisited and adjusted where required to ensure spots were positioned on the correct zones in each grain. Spot positions were also selected for all standards used. These included the 91500 primary reference material (^{206}Pb/^{238}U accepted age of 1062.4 Ma ± 0.4 Ma; Wiedenbeck et al. 1995) and the NIST-610, Pleŝovice (^{206}Pb/^{238}U accepted age of 337.1 ± 0.4 Ma; Sláma et al. 2008) and Temora2 (^{206}Pb/^{238}U accepted age of 416.8 ± 0.3 Ma; Black et al. 2004) as secondary standards.

All samples were analysed over 4 laser ablation runs. During the first run, in which samples BG-01, SM-01 and SM-02 were analysed, Pleŝovice returned a weighted mean $^{206}Pb/^{238}U$ age of 340.1 ± 1.1 Ma (MSWD = 0.8, n = 18). During the second run, in which samples CR-05 and CH-01 were analysed, Pleŝovice generated a weighted mean $^{206}Pb/^{238}U$ age of 338.9 ± 1.2 Ma (MSWD = 1.2, n = 21). During the third run, during which samples JD-01, CR-06 and CH-02 were lasered, a weighted mean $^{206}Pb/^{238}U$ age of 340.1 ± 1.8 Ma (MSWD = 1, n = 24) was calculated for Pleŝovice. During the final run, in which samples CR-07 and CR-08 were analysed, Pleŝovice returned a weighted mean $^{206}Pb/^{238}U$ age of 336.7 ± 1.3 Ma (MSWD = 0.7, n = 17). It is important to note that not all measured Pleŝovice ages were within error of the reported literature value ($^{206}Pb/^{238}U$ accepted age of 337.1 ± 0.4 Ma; Sláma et al. 2008). Standard-sample bracketing was used, with an average of ~4 unknowns between standards.

3.3.3. Iolite (v.4) and data reduction

Isotope data and accompanying laser logs were transferred from the mass spectrometer directly into Iolite in .csv file format. Once imported, the appropriate isotopes were selected (e.g., ^{206}Pb, ^{207}Pb, ^{235}U, ^{238}U; Table 3.1) and data integration signals for individual spots in each sample were adjusted to account for Pb loss. The VizualAge live Concordia tool was used to identify Pb loss across integration signals. Where data integration signals for individual spots exhibited Pb loss trends at the start of their signal, signals were not trimmed because CL images were only available for the grain surface, thus the start of the signal. Therefore, spots exhibiting Pb loss patterns at the start of their integration were rejected as there was no CL reference for the remaining concordant part of the signal. Where integration signals exhibited Pb loss trends towards the end of their signal, these were trimmed appropriately to remove the Pb loss component and were included at the IsoplotR stage (see below).

All samples were run through the U-Pb geochronology data reduction scheme (DRS) (Paton et al. 2011). Primary and secondary reference materials were checked using the Concordia age function in the quality assurance/quality control tab (‘QA/QC’ in Iolite) to ensure measured ages were within error of the accepted published age for that standard. Iolite datasets were exported as .csv files in preparation for Isoplot data processing.

3.3.4. Strategy to identify final "ages" for each sample and to isolate cases of common Pb, Pb loss and antecrystic zircon growth

Iolite datasets were processed and displayed in IsoplotR (Vermeesch, 2018). The zircon ID, $^{206}Pb/^{238}U$ and $^{207}Pb/^{235}U$ mean ratios, standard errors (2σ) and the $^{206}Pb/^{238}U$ vs $^{207}Pb/^{235}U$ rho values within the Iolite .csv datasets for each sample were imported into IsoplotR. The Wetherill $^{206}Pb/^{238}U$ vs $^{207}Pb/^{235}U$ Concordia plot and $^{206}Pb/^{238}U$ weighted mean plots were at this stage carefully investigated alongside textures and contextual evidence from the field (e.g., cross-cutting relationships, relative emplacement understanding), primarily to isolate a statistically and geologically acceptable age of igneous emplacement for each sample.

The first objective was to omit points which were discordant, in particular those plotting horizontally to the right of the Concordia on the Wetherill Concordia plot (i.e., towards infinite $^{207}Pb/^{235}U$). Due to the lower precision (~1 – 2%) of LA-ICP-MS (vs e.g., secondary ion mass spectrometry) and the inability of the mass spectrometer to distinguish between isotopes of the same mass (e.g., ^{204}Pb vs ^{204}Hg), no common Pb correction could be applied at the analytical stage (Andersen, 2002). Iolite data integration signals were revisited and ^{204}Pb levels were closely monitored for each spot plotting off to the right of the Concordia. Spots with above-background level of ^{204}Pb generally correlated with those spots plotting horizontally to the right, indicating the presence of common Pb. Such spots were therefore excluded from further discussion as these reflect highly altered zircons or laser intersection with the resin.

The second objective was to omit spots that had clearly been affected by Pb loss, as well as points significantly older than ages expected to represent an appropriate time of emplacement, the latter probably reflecting xenocrystic zircon growth. Spots considered to be affected by Pb loss were those which tailed off towards younger ages from a cluster of concordant points that seemed to define a significant stage of growth in the overgrowths, on both the Concordia and weighted mean plots. These points were excluded as their inclusion had a detrimental effect on the weighted mean age and error (i.e., statistically unacceptable MSWD). The remaining concordant to near-concordant points were recalculated using the

Stacey-Kramers common Pb correction model offered by IsoplotR (Stacey and Kramers, 1975; Vermeesch, 2018). The corrected dataset was plotted on a $^{206}Pb/^{238}U$ weighted mean plot before textural evidence was revisited to determine which points were most likely to represent the age of emplacement. Any mention of "uncorrected" in Chapter 4 and Chapter 5 refers to original $^{206}Pb/^{238}U$ ages prior to application of the Stacey Kramers common Pb correction (Stacey and Kramers, 1975).

To determine which points were most likely emplacement related, zircons with inverse core – rim age relationships were first carefully investigated. In grains where the spot on a zircon core or inner rim produced an age younger than the outer rim age, both core and rim spots were omitted. In the case where grains contained multiple spots on the same zone and one spot exhibited a markedly different age to the other, both spots were omitted due to uncertainty over the extent of Pb loss.

Zircon CL images for remaining grains were revisited to select which spots were most likely emplacement related. CL images for zircon grains analysed from each sample in this study are presented in the Section 4.2. The reader is encouraged to refer to all figures in Section 4.2 for examples of the textural features outlined here. Emplacement spots were defined texturally most confidently as spots on the outermost rims of grains. Spots on the next inner zone where the outermost rims were too narrow for a ~30 µm spot and there was no textural evidence for resorption between the outermost part of the rim and inner parts (e.g., Carsphairn samples) were also considered as more likely than not representing growth at the time of emplacement. Although these inner rim spots may not be representative of the absolute youngest growth of the respective grains, for some of the larger sample datasets (e.g., Cheviot) this was the only option available as outermost rims were extremely narrow, only a few µm across. Finally, spots on small grains of <~50 µm with continuous magmatic zoning (Fig. 2.8 B) from the grain centre to the rim were also interpreted as probably representing growth during emplacement. For most samples a $^{206}Pb/^{238}U$ weighted mean age was calculated from rims only. For a few samples, good rims were lacking and a final $^{206}Pb/^{238}U$ weighted mean age was calculated from cores of small zircons only (e.g., CR-08) or a mix of cores and rims (e.g., mainly for minor intrusions JD-01 and SM-01).

After emplacement spot selection, what remained were typically cores which either i) were older than the confidence interval of the weighted mean age interpreted to represent an appropriate time of emplacement, representing antecrystic growth or ii) fell within the confidence interval of the weighted mean age interpreted to represent an appropriate time of emplacement but which texturally did not appear to be the last zircon growth in that crystal. The latter were deemed to be cores which probably experienced Pb loss at the time of emplacement. A few rims also plotted at visibly older ages compared to the selected emplacement spots. These considerably affected the weighted mean statistics (see below) and were interpreted as probably representing antecrystic growth.

Throughout this systematic process, weighted mean $^{206}Pb/^{238}U$ ages were monitored, including the confidence interval and the mean standard weighted deviation statistic (MSWD) (Wendt and Carl, 1991)**.** Figure 3 of Spencer et al. (2016) was used to ensure that all final points included in the weighted mean $^{206}Pb/^{238}U$ age represented a statistically acceptable zircon population (Fig.3.1). The MSWD statistic is intrinsic to the IsoplotR workflow and its calculation and range of acceptable values for a given size of geochronological dataset are outlined in Spencer et al. (2016) and Wendt and Carl (1991). A MSWD value of ~1 associated with any proposed final $^{206}Pb/^{238}U$ age indicates that data are considered as distributed within a single population, and that the analytical uncertainties are neither over- nor under-reported for the size of the dataset. In practice, the ~1-2 % data point errors inherent in laser ablation analysis indicate that for large datasets, final weighted means with MSWD between ~0 – 1 are typical, reflecting the inclusion of multiple points with similar absolute ages but large analytical errors.

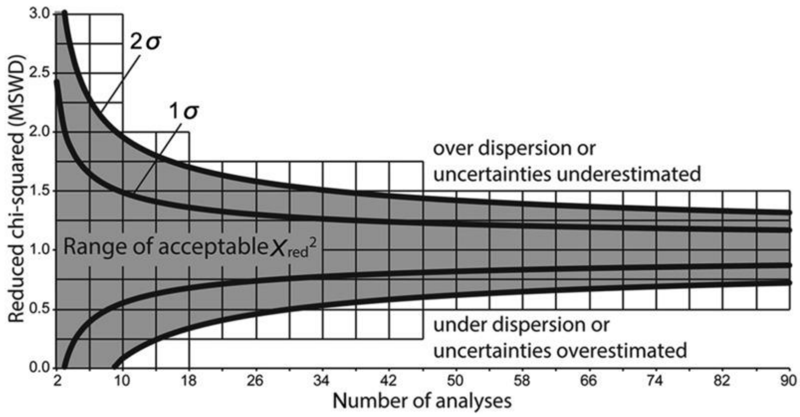

Figure 3.1: Summary figure of Spencer et al. (2016) outlining the range of statistically acceptable MSWD values for a given number of analyses for 1σ and 2σ.

3.3.5. Trace element data acquisition

Samples CR-07, CR-08 and CH-01 were selected for trace element analysis due to their large number of zircons, spot location availability and associated geochronological data. All three samples were analysed in one LA-ICP-MS run. Trace element spots were positioned immediately next to spots interpreted as either emplacement related or antecrystic related based on obtained geochronological data where there was enough space for another ~30 µm laser spot. Trace element analyses were calibrated to NIST-610, 91500, Pleŝovice, Mount Dromedary and an in-house reference material with ^{91}Zr selected as an internal standard (Allen and Campbell, 2012; Faithfull et al. 2018; Sláma et al. 2008; Wiedenbeck et al. 1995). Standards were distributed between zircon analyses. The LA-CIP-MS settings for trace element data acquisition are outlined in Table 3.2

Trace element data was processed in Iolite (v.4) using the 3D elements data reduction scheme (Paton et al. 2011; Paul et al. 2023)**.** Reference materials NIST 610 and 91500 were selected as the primary standards. A multi-reference calibration was used because whilst the 91500 standard is matrix matched; it does not contain all measured elements whereas NIST 610 contains all measured elements but is not matrix matched. During data reduction, all data in which the LA-ICP-MS counts were below baseline were removed and data where the 1σ % error (% error as given in Appendix E) was <50% (i.e., where the 2σ > 100%) were also excluded.

Trace element concentration data were normalised according to chondrite values of McDonough and Sun (1995) and were presented on chondrite normalised plots for investigation. The titanium (Ti)-in-zircon temperature was calculated (Fig. 3.2) for all analysed trace element spots using the equation of Watson et al. (2006). Errors noted included the published errors for the Ti-in-zircon calibration alongside the 1δ errors in analysed Ti concentration. All Iolite-processed trace element data are provided in Appendix E.

Table 3.2: Summary of LA-ICP-MS parameters used for trace element analysis of zircons.

Acquisition parameters	
Spot size	30 µm
Ablation time	30 seconds
Fluence	3.5 J/cm^2
Repetition rate	10 Hz
Isotope channels measured	^{49}Ti, ^{51}V, ^{57}Fe, ^{63}Cu, ^{66}Zn, ^{88}Sr, ^{91}Zr, ^{93}Nb, ^{109}Ag, ^{118}Sn, ^{139}La, ^{140}Ce, ^{141}Pr, ^{146}Nd, ^{147}Sm, ^{153}Eu, ^{157}Gd, ^{89}Y, ^{159}Tb, ^{163}Dy, ^{165}Ho, ^{166}Er, ^{169}Tm, ^{172}Yb, ^{175}Lu, ^{178}Hf, ^{181}Ta, ^{182}W

$$\log(Ti_{zircon}) = (6.01 \pm 0.03) - \frac{5080 \pm 30}{T(k)}$$

$$\frac{5080 \pm 30}{T(k)} = (6.01 \pm 0.03) - \log(Ti_{zircon})$$

$$\frac{T(k)}{5080 \pm 30} = \frac{1}{(6.01 \pm 0.03) - \log(Ti_{zircon})}$$

$$T(k) = 5080 \pm 30\left(\frac{1}{(6.01 \pm 0.03) - \log(Ti_{zircon})}\right)$$

Figure 3.2: Ti-in-zircon temperature calculation of Watson et al. (2006). Note that Ti$_{zircon}$ refers to the concentrations (ppm) of Ti in analysed zones and T*(k)* refers to the Ti-in-zircon temperature in units of kelvin. Calculation obtained from Dardier et al. (2021).

4. Results

4.1. Sample overview

Sample petrography is summarised in Table 4.1 below. Hand specimen and thin section images are provided in Appendix A.

Table 4.1: Petrographic descriptions for samples analysed from the Carsphairn pluton, Black Stockarton Moor subvolcanic complex and the Cheviot pluton.

Sample (grid reference)	**Major mineralogy**	**Alteration assemblage**	**Grain size**	**Miscellaneous (any other notable petrographic features)**	**QAPF classification**
CR-05 **(NX 59450 98020)**	Alkali-feldspar (40%), quartz (30%), plagioclase (20%), biotite (10%). Accessory apatite and zircon ± titanite.	Alteration of plagioclase to sericite and epidote. Alteration of biotite to chlorite.	0.1 – 3.0 mm	N/A	Granite
CR-06 **(NX 59088 97913)**	Plagioclase (35 %), quartz (35%), alkali feldspar (20%), biotite (10%). Accessory zircon ± apatite.	Alteration of plagioclase to sericite. Clay alteration of major mineralogy present throughout.	0.2 – 2.5 mm	Very fractured in thin section. Potentially due to possible shear/fault related zone at Carsphairn. Areas interpreted as clay alteration could be gaps within the thin section.	Granite - granodiorite
CR-07 **(NX 58862 97768)**	Plagioclase (40%), biotite (30%), quartz (20%) alkali feldspar (10%). Accessory zircon ± titanite.	Alteration of feldspars to sericite. Partial replacement of biotite by epidote(?) and/or chlorite(?) and of other major minerals by clay.	0.1 – 3.0 mm	Fractured in thin section. Areas interpreted as clay alteration could be gaps within the thin section.	Granodiorite
CR-08 **(NX 58562 97559)**	Plagioclase feldspar (30%), biotite (25%), alkali feldspar (20%), quartz (20%), clinopyroxene? (5%). Accessory zircon and apatite.	Alteration of plagioclase to sericite. Partial replacement of biotite by epidote(?) and/or chlorite(?) and of other major minerals by clay.	0.1 – 3.0 mm	Very fractured in thin section. Interpreted as clinopyroxene (over amphibole) as grains lacked intersecting 70^0 cleavages, exhibited total extinction at $\sim40^0$ and moderate – high relief in PPL. Areas interpreted as clay alteration could be gaps in the thin section. Interpreted as epidote based on blue/green pleochroism in PPL, straight extinction and high order interference colours in XPL. Interpreted as chlorite by green – yellow pleochroism in PPL, anomalous interference colours (e.g., cream grey, white – grey blue).	Monzo-granite
JD-01 **(NX 70947 53015)**	Plagioclase feldspar (67%), amphibole (20%), alkali feldspar (5%), quartz (5%), chlorite? (3%). Accessory zircon, apatite and monazite.	Alteration of plagioclase feldspars by sericite. Replacement of amphibole with chlorite(?). Calcite partially replaces amphibole and feldspars.	2.0 – 3.0 mm	Significant alteration, difficult to identify primary mineralogy.	Quartz diorite
SM-02	Plagioclase feldspar (70%), amphibole (20%), alkali feldspar	Alteration assemblage of calcite, chlorite and sericite.	<0.1 – 2.5 mm	Significant alteration, difficult to identify primary mineralogy.	Quartz diorite

(NX 72427 54975)	(5%), quartz (5%). Accessory apatite, titanite and zircon.				
SM-01 **(NX 73293 54509)**	Plagioclase feldspar (70%), quartz (10%), alkali-feldspar (5%), amphibole (5%), other (10%). Accessory zircons.	Alteration of plagioclase to sericite. Calcite, chlorite and epidote(?) as secondary minerals.	0.1 – 2.5 mm	Significant alteration, difficult to identify primary mineralogy.	Quartz diorite
BG-01 **(NX 772 538)**	Plagioclase feldspar (47%), biotite or amphibole (20%), alkali feldspar (20%), quartz (10%). Accessory zircon, apatite, titanite and monazite.	Alteration plagioclase to sercite. Other secondary minerals include calcite, chlorite and clay.	<0.3 – 5 mm	Significant alteration, difficult to identify primary mineralogy.	Quartz monzo-diorite
CH-01 **(NT 9369 2041)**	Alkali feldspar (35%), plagioclase feldspar (25%), biotite (25%), quartz (15%), tourmaline (%?). Accessory zircon and apatite.	Alteration of plagioclase to sericite. Replacement of biotite by chlorite and epidote(?). Clay alteration of primary minerals.	0.5 – 4.0 mm	Tourmaline interpretation based on pleochroism in PPL, simple twinning, 2^{nd} – 3^{rd} order interference colours including deep blues, greens, pinks in XPL. Phenocrysts up to 11 mm in length.	Quartz monzonite
CH-02 **(NT 9232 2047)**	Alkali feldspar (45%), quartz (20%), biotite (20%), plagioclase feldspar (15%). Accessory zircon and apatite.	Alteration of feldspars to sericite and replacement of biotite with chlorite and epidote. Clay alteration of major mineralogy.	0.1 – 5.0 mm	N/A	Syenogranite

4.2. Geochronology

4.2.1. Cairnsmore of Carsphairn

4.2.1.1. CR-08

A total of 119 grains were mounted for CR-08. Of the 105 grains imaged, 55 grains were identified as suitable for laser ablation. The reader is directed to Appendix B_CG23-CR-08_CL images and Appendix C_zircon textures - table 10, for annotated CL images and detailed textural descriptions of all CR-08 grains. CR-08 zircons are texturally ambiguous, and cores and rims cannot always be clearly distinguished. Most analysed grains are subhedral (Fig.4.1 e). Cores are generally larger than overgrowths in most grains (Fig. 4.1 a - e). Grains vary between *c.* 100 µm – *c.* 275 µm in length. Zircons are variably fractured (Fig. 4.1 a-e). Most grains exhibit localised loss of zonation and/or bright patches in CL images throughout magmatic overgrowths and/or cores related to fractures (Fig.4.1 a - e). Most grains contain inclusions of variable size (Fig.4.1 a - e).

Where cores can be distinguished, they are semi-homogeneous, and most are zoned. Faint patchy oscillatory zoning dominates (Fig. 4.1 a - e). Many cores are complex in shape (Fig.4.1 a). Potential partial resorption is observed in some cores; however, it is difficult to distinguish between what is resorption, what is a mineral inclusion and what may be an inherited core due to the textural complexity of CR-08 zircons (Appendix C - table 10).

Few magmatic overgrowths can be clearly defined CR-08 (Fig.4.1 b, e). Where these are distinguished, overgrowths are unzoned. Where zoning is observed, very faint patchy oscillatory zoning dominates. The width and texture of CR-08 magmatic overgrowths is variable. In many grains, the overgrowth consists of a very narrow to broad semi-homogeneous unzoned dark rim (Fig.4 a), partial in a few grains. This might not be reflective of latest growth, rather could be fluid-related growth. In these grains overgrowths are smaller and border a larger core (Fig.4 a). In fewer grains in addition to the dark outermost rim, the overgrowth is more heterogeneous and slightly larger, bordering a larger or equally sized core. Those grains not included in LA-ICP-MS analysis were rejected based on complex internal structures (Fig.4.1 e -29), the inability to properly distinguish between cores and rims in most grains (Fig.4.1 e -18), fractures and associated alteration. In several grains, the grain is too small, or individual zones are too narrow and/or irregular and there are too many inclusions for a 30 µm laser spot (Appendix C - table 10).

A total of 74 points (n = 74) over 55 grains were analysed for CR-08 (Appendix B_CG23-CR-08). Most concordant and near concordant points plot between ~408 Ma and ~421 Ma on the Wetherill Concordia (Fig.4.1 f). 53 points were omitted due to common Pb, probable Pb loss, because spots were significantly older than expected emplacement-related spots and/or due to incorrect core – rim relationships (Fig.4.1 f) as outlined in the Methodology (see Chapter 3.3.3.4). The remaining 21 concordant and near-concordant spots were recalculated using the Stacey Kramers common Pb correction model and plotted on a $^{206}Pb/^{238}U$ weighted mean plot (Fig.4.1 g).

CL images indicated that the remaining 21 spots were all on zircon cores (Fig.4.1 a-c). Such grains did not have clear rims, were broadly larger than ~50 µm and lacked continuous well-developed oscillatory zoning from the grain centre to the rim (Fig. 4.1 a-c). Only core spots were included in the $^{206}Pb/^{238}U$ weighted mean age calculation as no acceptable rims were identified in CR-08. Including all cores, spread from ~407 – 421 Ma, gave an age of 413.8 ± 1.2 (n = 21, MSWD = 2.6) which is statistically unacceptable (i.e., over-dispersed; Spencer et al. 2016) and not representative of one zircon population (Fig.4.1 g). The significance of this age will be discussed in Chapter 5, 5.2.1.2. The oldest core produced an uncorrected $^{206}Pb/^{238}U$ age of 420.4 ± 5.5 Ma (Fig.4.1 c, g).

The single omitted oldest spot with an uncorrected $^{206}Pb/^{238}U$ age of 427.2 ± 4.9 Ma (Fig. 4.1 d) is significantly older and outwith analytical error of the final weighted mean age and predates final deposition into the Southern Uplands prism, thus is interpreted as representing xenocrystic zircon growth.

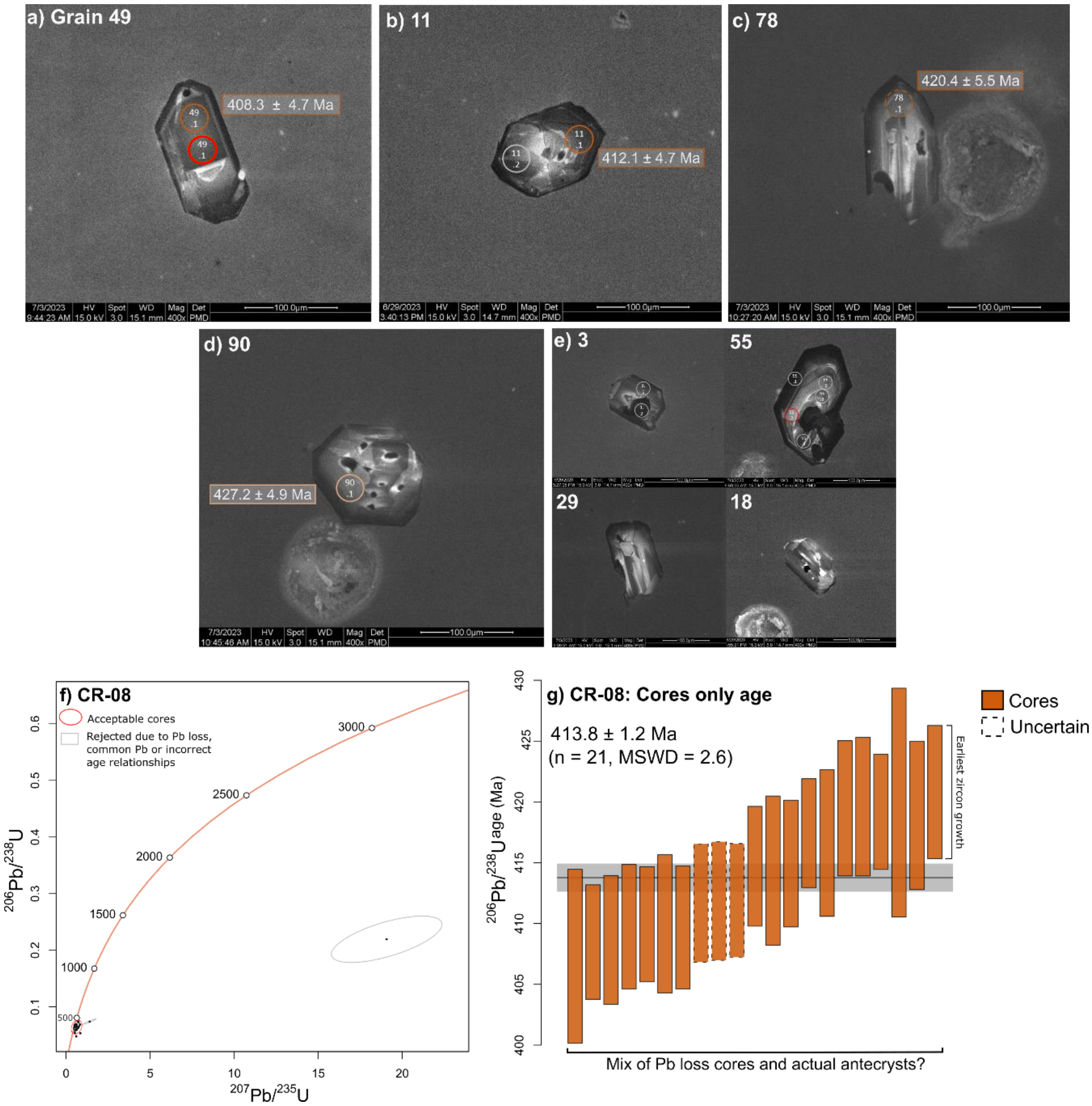

Figure 4.1: CG23-CR-08. CL images of analysed and acceptable zircons, grains analysed but rejected due to probable Pb loss, common Pb or incorrect age relations (light grey) and zircons not analysed by LA-ICP-MS (not annotated). Grains presented include (a) 49 (b) 11 (c) 78: oldest zircon in CR-08 (d) 90 (e) 3, 55, 29, 18. Uncorrected (as per Chapter 3) $^{206}Pb/^{238}U$ ages are labelled for cores (orange) and xenocrysts (beige). Ages are not labelled for rejected spots. Analysed trace element spots are also annotated (red). Higher resolution versions of select CL images are provided in Appendix B_CG23-CR-08_CL images. (f) Annotated Wetherill Concordia plot shown prior to Stacey Kramers common Pb correction, contains all analysed acceptable and rejected U-Pb spots. (g) $^{206}Pb/^{238}U$ weighted mean plot following application of the common Pb correction, highlights all acceptable cores included in the weighted mean age for CR-08. Note that spots annotated as "uncertain" (dashed outline) refer to texturally ambiguous grains.

4.2.1.2. CR-07

A total of 110 grains were mounted for CR-07. Of the 102 grains imaged, 70 of these grains were deemed suitable for laser analysis (Appendix B_CG23-CR-07_CL images, Appendix C_zircon textures – table 9). Most grains are subhedral and cores are dominantly larger than overgrowths throughout grains (Fig.4.2 a - e). Grains vary between *c.* 113 µm – *c.* 675 µm in length with most grains ranging between *c.*113 µm and *c.* 375 µm. Grains are variably fractured with most grains exhibiting moderate degrees of fracturing (Appendix C - table 9). Most grains exhibit fractured-related localised alteration throughout cores and/or magmatic overgrowths (Fig.4.1 c, e). Inclusions are common within most grains (Fig.4.1 a, c).

Cores in CR-07 are dominantly semi-homogeneous and unzoned (Fig.4.1 a, b). Where cores exhibit zoning, faint patchy oscillatory zoning dominates (Fig.4.1 c). Most cores are complex in shape (Fig.4.1 a - e). Magmatic overgrowths in CR-07 are broadly semi-homogeneous (Fig.4.1 a - e) and contain very faint patchy oscillatory zoning (Fig.4.1 a - d). A dark outermost unzoned overgrowth of variable width is observed in most analysed grains. Several grains are broken (Fig.4 b, d). Grains excluded from laser ablation were rejected based on complex internal structures, chaotic irregular zoning, zones and/or grains being too small for a 30 µm laser spot, the fractured nature of grains and fracture-related alteration (Fig.4.1 e, 23, 77; Appendix C - table 9).

A total of 100 points (n = 100) over 70 grains were analysed for CR-07 (Appendix B_CG23-CR-07_CL images; Appendix D). Most visibly concordant and near concordant points plot between ~411 Ma and ~424 Ma on the Wetherill Concordia (Fig.4 f). 62 points were omitted due to common Pb, probable Pb loss, because spots were significantly older than expected emplacement-related spots (i.e., are probably xenocrystic) and/or due to incorrect core – rim relationships, as outlined in the Methodology (Chapter 3, 3.3.4). Following application of the Stacey Kramers common Pb correction (Stacey and Kramers, 1975), the remaining 38 concordant and near-concordant spots were plotted on a $^{206}Pb/^{238}U$ weighted mean plot (Fig.4.2 g).

Following close investigation of zircon textures for the remaining 38 spots, those most likely to have grown during emplacement were texturally constrained as spots positioned on inner overgrowths as the outermost narrow (few ~µm) dark overgrowths were too small for a ~30 µm laser spot (Fig.4.2 a - c). These “inner rim” spots were included in the weighted mean age calculation as there was no textural evidence for resorption between the “inner rim” zone and the outermost narrow rim (Fig.4.2 a - c). These were the only rim spots available for CR-07. A total of 9 rim spots were identified in CR-07 and are spread from ~412 Ma – 424 Ma (Fig.4.2 g), producing a statistically justified $^{206}Pb/^{238}U$ weighted mean age of 415.3 ± 1.7 Ma (MSWD = 1.8, n = 9). The significance of this age will be discussed in Section 5.2.1.2 (Fig.4.1 g).

After emplacement spot selection and the weighted mean calculation, a large spread of 29 spots remained, positioned on cores and plotting between ~412 Ma and ~424 Ma (Fig.4.2 g). The youngest 12 core spots plotted between ~412 Ma and ~417 Ma and fell within the confidence interval (i.e., age error) of the weighted mean age above (Fig.4.2 g). The oldest 17 cores plotted between ~417 Ma and ~424 Ma are outwith the confidence interval of the weighted mean age and are interpreted as representing antecrystic zircon growth (Fig.4.2 g).

The ten omitted oldest spots with corrected $^{206}Pb/^{238}U$ ages of ~425 Ma, ~430 to ~437 Ma, ~445 Ma and ~455 Ma are significantly older and outwith analytical error of the final weighted mean age. Most of these spots (excluding ~425 Ma which could be within error of final sedimentation in the accretionary prism at *c.* 420 Ma) significantly predate final deposition into the Southern Uplands prism (*c.* 420 Ma, Oliver et al. 2008), thus are interpreted as representing xenocrystic zircon growth.

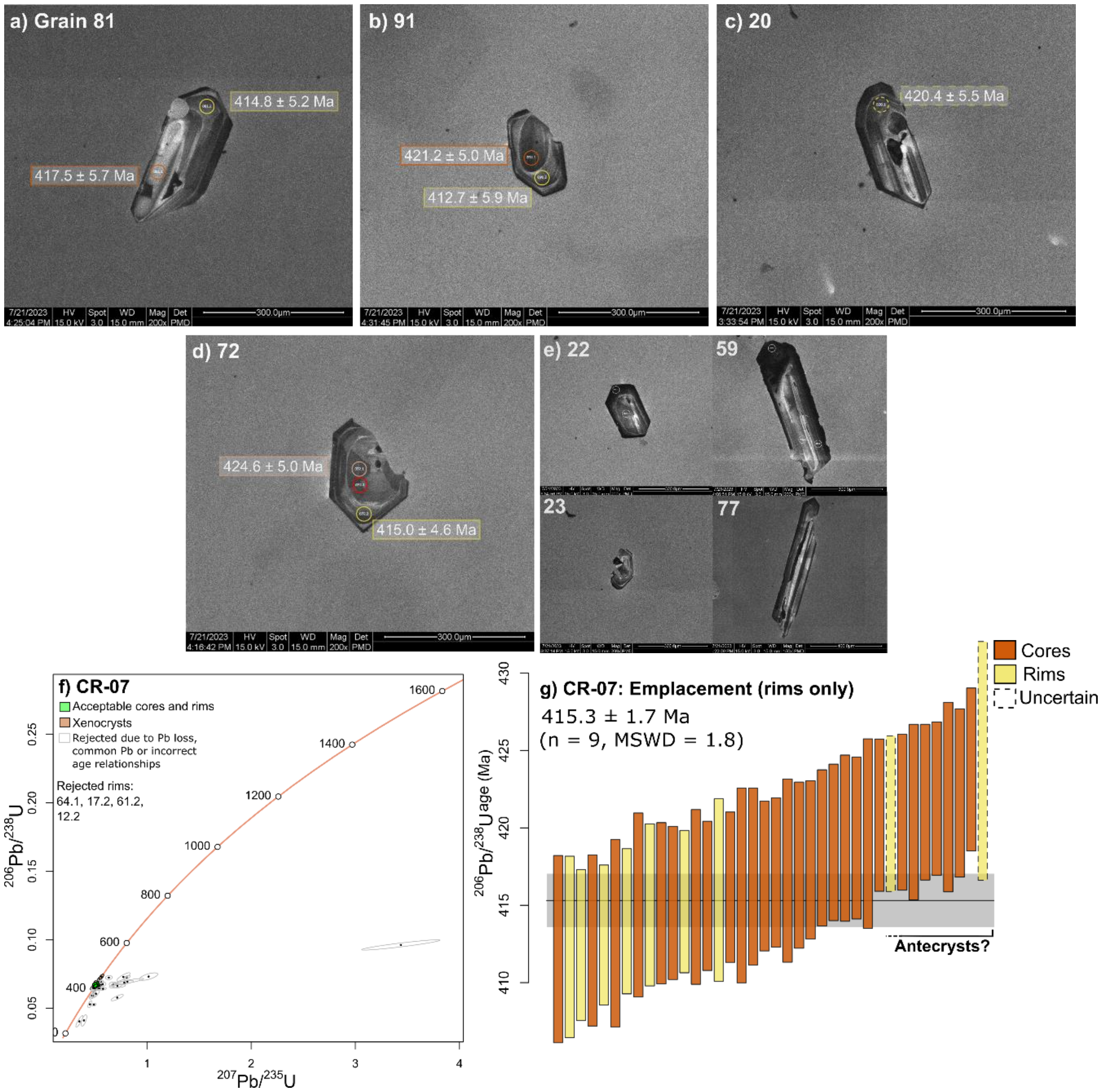

Figure 4.2: CG23-CR-07. (a) – (e) CL images of analysed and acceptable zircons (a – d), analysed but rejected (e – 22, 59) and zircons not analysed (e – 23, 77). Uncorrected $^{206}Pb/^{238}U$ ages labelled for emplacement rims (yellow), antecrystic cores (orange), potential antecrystic rims (dashed yellow) and xenocrysts (beige). Ages not labelled for spots rejected due to Pb loss, common Pb or incorrect age relations (light grey). Analysed trace element spots are labelled (red). Higher resolution versions of select CL images are provided in Appendix B_CG23-CR-07_CL images. (f) Annotated Wetherill Concordia plot shown prior to Stacey Kramers common Pb correction, contains all analysed acceptable and rejected U-Pb spots. Rims rejected at the age calculation stage due to evidence of Pb loss in Iolite are listed and are not plotted on the weighted mean plot. (g) $^{206}Pb/^{238}U$ weighted mean plot following application of common Pb correction. All acceptable concordant and near-concordant rims and cores are shown. All acceptable rims are included in the CR-07 weighted mean age. Rims annotated as uncertain (dashed outline) refer to older potentially antecrystic rims as discussed in text.

4.2.1.3. CR-06

A total of 110 grains were mounted for CR-06. Of the 66 grains imaged, 42 were deemed suitable for laser analysis (Appendix B_CG23-CR-06_CL images, Appendix C_zircon textures – table 8). Complex internal textures are observed in most grains (Fig.4.3 a - e). Most grains are subhedral. Cores are dominantly larger with smaller magmatic overgrowths (Fig.4.3 a - e). Grains range between *c.* 100 µm – *c.* 350 µm and reach up to 800 µm in length. Most grains are lightly fractured (Fig.4.3 b, d). Localised alteration is observed in the cores and/or magmatic overgrowths of most grains, spatially related to fractures and/or inclusions (Fig.4.3 a, b, d). Inclusions are present in several grains (Appendix C - table 8).

Most cores in analysed grains are heterogeneous and unzoned (Fig.4.3 a, d). Where zoning is observed, it is faint and patchy and both sector and oscillatory patterns are observed (Fig.4.3 b, c). Cores are subrounded to subangular in shape. Partial resorption is observed in at least 3 grains (e.g., Fig.4.3 d) where cores are texturally complex (Appendix C - table 8).

Most overgrowths in CR-06 contain heterogeneous faint patchy oscillatory zoning (Fig.4.3 a, d). Faint patchy sector zoning is occasionally observed in some grains (Appendix C - table 8). An outermost dark overgrowth of ranging from very narrow to broad, is observed around all grains (Fig.4.3 a - e). In most grains, this overgrowth is narrow, semi-homogeneous and unzoned. This dark outermost overgrowth represents the only clear overgrowth around large to very large cores in some grains. These outermost dark overgrowths might be fluid related. Grains were rejected from laser analysis based on the altered nature of grains, the overall complex textures, overlapping and cross-cutting zones, irregular zoning, narrow zones, small size (too small to fit 30 µm laser spot) and fracturing (Fig.4.3 e – 48, 54; Appendix C - table 8).

A total of 72 points (n = 72) over 43 grains were analysed for CR-06 (Appendix B_CG23-CR-06; Appendix D). The majority of visibly concordant and near concordant points plot between ~407 Ma and ~424 Ma on the Wetherill Concordia (Fig.4.3 f). 44 spots were omitted (Fig.4.3 f) due to common Pb, probable Pb loss, because spots were significantly older than spots interpreted to be emplacement-related and/or due to incorrect core – rim relationships, as outlined in the

Methodology (see Chapter 3, 3.3.4.). Following application of the Stacey Kramers common Pb correction (Stacey and Kramers, 1975), the remaining 28 concordant and near-concordant spots were presented on a $^{206}Pb/^{238}U$ weighted mean plot (Fig.4.3 g).

Following close investigation of zircon textures for the remaining 28 spots, those most likely to have grown during emplacement were texturally constrained as spots positioned on inner overgrowths closest to the outermost narrow (few ~µm) dark overgrowths that were too small for a ~30 µm laser spot (Fig.4.3 a). These “inner rim” spots were included in the weighted mean age calculation as there was no textural evidence for resorption between the “inner rim” zone and the outermost narrow rim (Fig.4.3 a). These were the only rim spots available for CR-06. A total of 5 rim spots were identified in CR-06 and are spread from ~407 Ma – 418 Ma (Fig.4.3 g), forming a statistically justified age of 412.0 ± 4.7 Ma (MSWD = 0.73, n = 5). The significance of this age will be discussed in Section 5.2.1.2.

After emplacement spot selection and the weighted mean calculation, a total of 23 spots remained, all located on zircon cores (Fig.4.3 g). The youngest 18 core spots plotted between ~407 Ma and ~417 Ma and fell within the confidence interval of the weighted mean age (Fig.4.3 g). The oldest 5 core spots plotted between ~419 Ma and ~424 Ma, are outwith the confidence interval of the weighted mean age and are interpreted as representing antecrystic zircon growth (Fig.4.3 g).

The seven omitted oldest spots with $^{206}Pb/^{238}U$ ages of ~440 Ma, ~449 Ma, ~490 Ma, ~500 Ma, ~1430 Ma and 2 spots at ~1450 Ma, are significantly older and outwith analytical error of the final weighted mean age (Fig.4.3 f). These predate final sedimentation in the Southern Uplands prism (*c.* 420 Ma; Oliver et al. 2008), thus are interpreted as xenocrysts potentially derived from host rocks during magma ascent and emplacement (Fig.4.3 c).

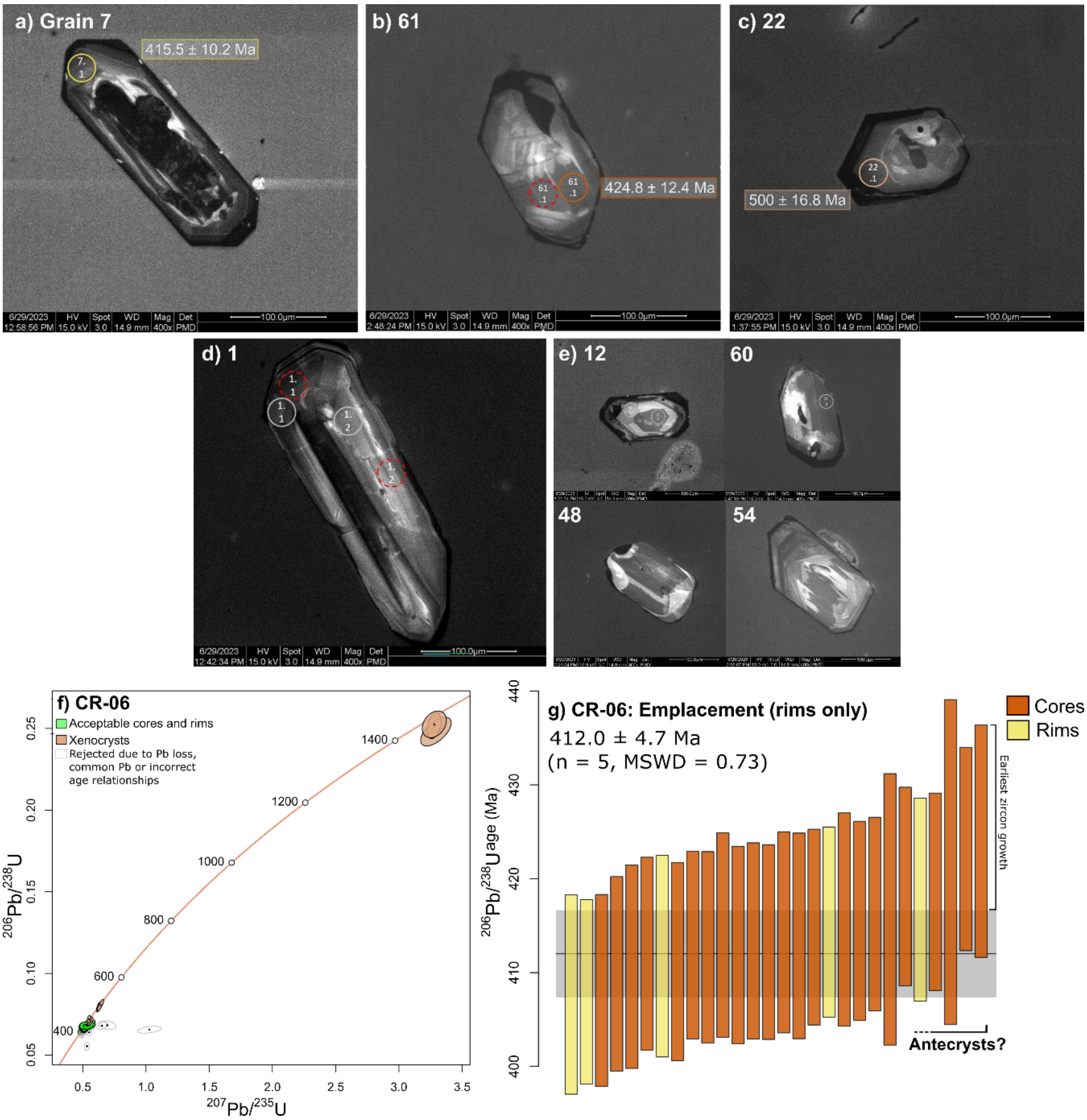

Figure 4.3: CG23-CR-06. (a) – (e) CL images of analysed and acceptable zircons (a – c), grains directly mentioned in text (d), analysed but rejected (d – e 12, 60) and zircons not analysed (e – 48, 54). Uncorrected $^{206}Pb/^{238}U$ ages labelled for emplacement rims (yellow), antecrystic cores (orange) and xenocrysts (beige). The earliest zircon crystallised in CR-06 is presented (b). Ages not labelled for spots rejected due to Pb loss, common Pb or incorrect age relations (light grey). Potential trace element spots for future analysis are labelled (dashed red). Higher resolution versions of select CL images are provided in Appendix B_CG23-CR-06_CL images. (f) Annotated Wetherill Concordia plot shown prior to Stacey Kramers common Pb correction, contains all analysed acceptable and rejected U-Pb spots. No rims were rejected due to Pb loss at the age calculation stage. (g) $^{206}Pb/^{238}U$ weighted mean plot following application of common Pb correction. All acceptable concordant and near-concordant rims and cores are shown. All acceptable rims are included in the CR-06 weighted mean age.

4.2.1.4 CR-05

A total of 120 grains were mounted for CR-05. Out of the 66 grains imaged, 53 of these grains were deemed suitable for laser ablation (Appendix B_CG23-CR-05_CL images, Appendix C_zircon textures – table 7). All grains exhibit complex internal structures and are dominantly subhedral (Fig. 4.4 a – e). In most grains, cores are larger with smaller magmatic overgrowths (e.g., Fig.4.4 a). Cores cannot always be distinguished due to the complex internal structure of several grains (Appendix B_CG23-CR-05). Grains vary from *c.* 100 µm – *c.* 350 µm in length and exhibit variable degrees of fracturing. Most grains are moderately fractured with fractures extending across the entire length of most grains (Appendix C - table 7). Localised loss of zonation is observed in most grains, closely associated with fractures (Fig.4.4 a, b). Inclusions are observed in many grains (Fig.4.4 d).

Cores in CR-05 are predominantly heterogeneous (Fig.4.4 a, d, e - 33). Cores exhibit variable types and degrees of zoning. Most cores are unzoned (Fig.4.4 b). Where zoning is present, both oscillatory and sector patterns are observed (Fig.4.4 c). Zoning is broadly faint and patchy in CR-05 zircon cores (Fig.4.4 a - d). Most cores are subrounded - angular in shape. At least two cores exhibit partial resorption (e.g., Fig.4.4 d). Inclusions overlap cores in two grains (Appendix B_CG23-CR-05, e.g., 1, 19).

Rims in CR-05 zircon grains are generally heterogeneous. Most overgrowths exhibit faint heterogeneous oscillatory zoning (Fig.4.4 a), and zoning is generally patchy. Sector zoning is also observed in some overgrowths (Appendix C - table 7). A dark unzoned outermost narrow - broad overgrowth is present around all CR-05 grains (Fig.4.4 a – e). In some grains this outermost overgrowth is the only overgrowth that can be clearly defined. It is generally unzoned, homogeneous and narrow as opposed to the larger cores. However, most grains contain the narrow - broad dark outermost overgrowth in addition to other variably zoned overgrowths around a larger core (Fig.4.4. a, b). This outermost overgrowth might be fluid related. Grains not analysed were rejected due to heterogeneous and complex internal structures, very poorly developed patchy zoning or a lack of zoning, small grain size and narrow zones (i.e., too small for ~30 µm spot), alteration and/or the heavily fractured nature of these rejected grains (Fig.4.4 e – 6, 53; Appendix C - table 7).

A total of 82 points (n = 82) over 53 grains were analysed for CR-05 (Appendix B_CG23-CR-05; Appendix D). Most concordant and near concordant points plot between ~405 Ma and ~421 Ma on the Wetherill Concordia (Fig.4.4 f). 48 points were omitted due to common Pb, probable Pb loss, because spots were significantly older than expected emplacement-related spots and/or due to incorrect core – rim relationships (Fig. 4.4 f) as outlined in the Methodology (Chapter 3, 3.3.4.). Following application of Stacey Kramers common Pb correction, the remaining 34 concordant and near-concordant spots were plotted on a $^{206}Pb/^{238}U$ weighted mean plot (Fig. 4.4 g).

Following close investigation of zircon textures for the remaining 34 spots, those most likely to have grown during emplacement were texturally defined as spots positioned on inner overgrowths closest to the outermost narrow (few ~µm) dark overgrowth that was too small for a ~30 µm laser spot (Fig.4.4 a, b). These “inner rim” spots were included in the weighted mean age calculation as there was no textural evidence for resorption between the inner overgrowths and the outermost narrow overgrowths (Fig.4.4 a, b). These “inner rim” spots were the only analysable overgrowth spots available for CR-05. A total of 13 rim spots were identified and interpreted as most representative of emplacement growth, ranging between ~405 Ma - ~414 Ma (Fig.4.4 g). The $^{206}Pb/^{238}U$ weighted mean age of the 13 rim spots is 410.5 ± 1.8 Ma (MSWD = 0.78, n = 13) which is a statistically acceptable population according to Spencer et al. (2016).

After emplacement spot selection and the weighted mean calculation, a total of 21 spots remained, all positioned on zircon cores (Fig.4.4 g). The youngest 10 spots plotted between ~407 Ma and ~411 Ma and fell within the confidence interval of the weighted mean age interpreted to represent an appropriate time of emplacement (Fig.4.4 g). The oldest 11 core spots plotted between ~414 Ma and ~422 Ma and are outwith the confidence interval of the weighted mean age, are therefore interpreted as antecrysts (Fig.4.4 g).

The two omitted oldest spots with $^{206}Pb/^{238}U$ ages of ~426 Ma and ~427 Ma (Fig.4.4 f) are significantly older and outwith analytical error of the final weighted mean age.

and may predate final sedimentation in the Southern Uplands prism, thus are interpreted as xenocrystic zircon growth (Fig.4.4 c).

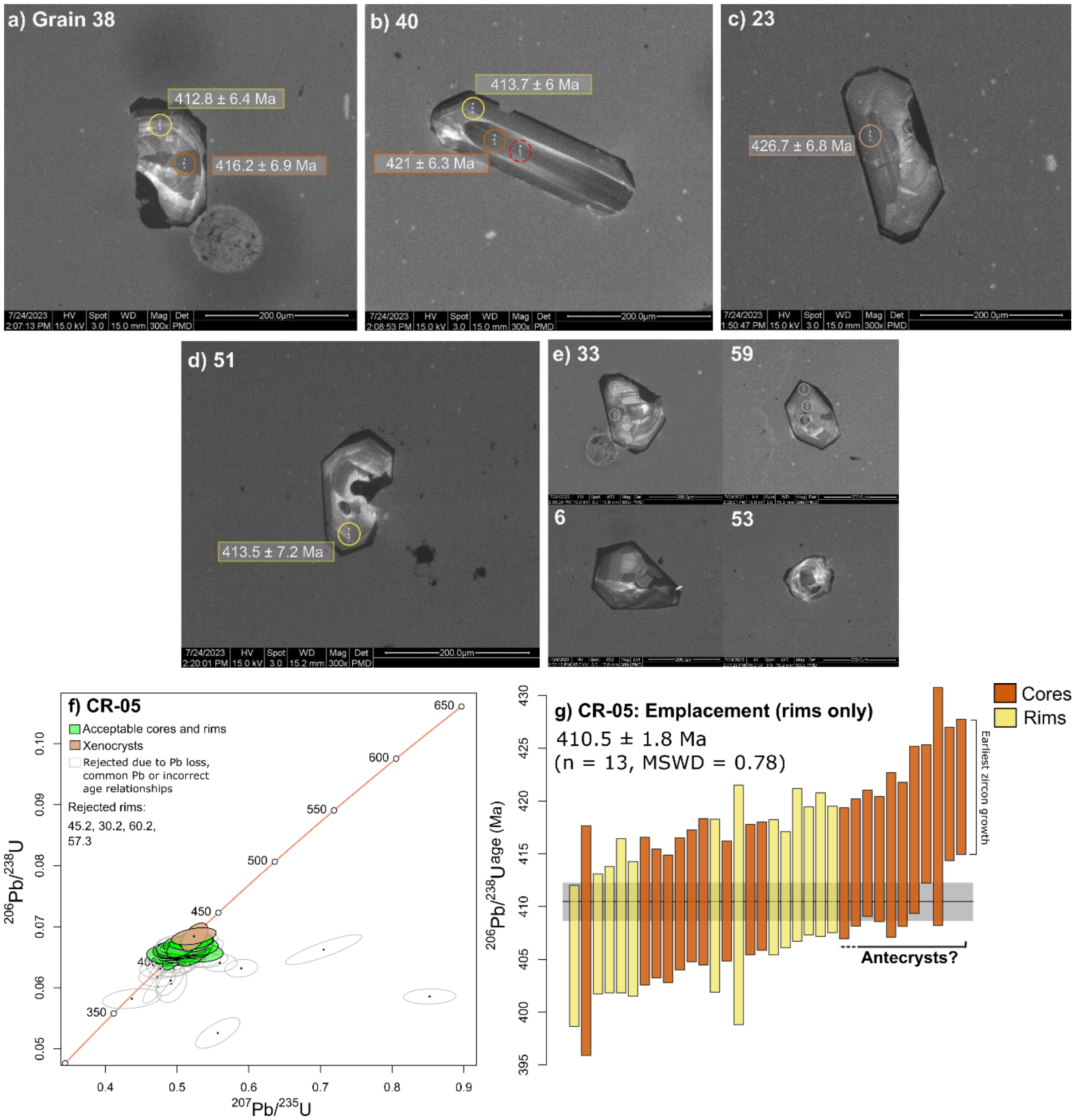

Figure 4.4: CG23-CR-05. (a) – (e) CL images of analysed and acceptable zircons (a – d), grains directly mentioned in text (d), analysed but rejected (e - 33, 59) and zircons not analysed (e – 6, 53). Uncorrected $^{206}Pb/^{238}U$ ages labelled for emplacement rims (yellow), antecrystic cores (orange) and xenocrysts (beige). Ages not labelled for spots rejected due to Pb loss, common Pb or incorrect age relations (light grey). Potential trace element spots for future analysis are labelled (dashed red). Higher resolution versions of select CL images are provided in Appendix B_CG23-CR-05_CL images. (f) Annotated Wetherill Concordia plot prior to Stacey Kramers common Pb correction, contains all analysed acceptable and rejected U-Pb spots. Rims rejected at the age calculation stage due to evidence of Pb loss are listed. (g) $^{206}Pb/^{238}U$ weighted mean plot following application of common Pb correction. All acceptable concordant and near-concordant rims and cores are shown. All acceptable rims are included in the CR-05 weighted mean age.

4.2.2. Black Stockarton Moor and Bengairn

4.2.2.1. JD-01

A total of 134 grains were mounted for JD-01. Out of the 86 grains imaged, 22 of these grains were suitable for analysis (Appendix B_CG22-JD-01_CL images, Appendix C_zircon textures – table 6). Most grains are subhedral (Fig.4.5 a - g). The relative core to rim size is variable. In most grains, this cannot be established due to the complex internal structure of grains. Where core – rim boundaries can be defined, cores are generally larger with smaller magmatic overgrowths (Fig.4.5 d). Grains range from *c.* 63 µm – 275 µm in length. Grains exhibit variable degrees of fracturing (Appendix C - table 6). Evidence for alteration and/or recrystallisation (e.g., loss of original zoning structures, overprinting by homogeneous pale patches, bright spots and patches throughout grains) is observed in the cores and/or overgrowths of most grains and is usually closely associated with fractures (Fig.4.5 b, f, g).

Cores in analysed grains are broadly semi-homogeneous to heterogeneous, range from unzoned to faintly zoned and where visible, though often patchy, zoning is oscillatory (Appendix C - table 6). Cores are texturally variable and are round (Fig. 4.5 a) to subrounded in shape. The core – rim boundary can be defined in some grains (Fig. 4.5 a, b, e). There were a few grains with poorly defined core – rim boundaries and very faint complex zoning which produced highly discordant uninterpretable results (Fig. 4.5 g, h). A degree of fracture-related alteration and/or recrystallisation is observed in the cores of most JD-01 zircons (Appendix C - table 6). Partial resorption is observed within the core (e.g., Fig. 4.5 g - m2_34) and along the core - rim boundary of two grains (Appendix B_CG22-JD-01 e.g., m1_13.1).

Overgrowths are texturally heterogeneous and generally contain variable oscillatory zoning and occasionally, faint sector zoning (Fig.4.5 c). Zoning is faint or prominent and patchy in some grains (Appendix C - table 6). Grains deemed unsuitable for analysis were rejected to individual zones being too small for a 30 µm laser spot, the complex internal structure of many grains, a high degree of fracturing and partial resorption, alteration and/or recrystallisation (Fig.4.5 g – m1_20, m2_33).

A total of 34 points (n = 34) over 22 grains were analysed for JD-01 (Appendix B_CG22-JD-01; Appendix D). Most concordant and near concordant points plot between ~417 Ma and ~424 Ma on the Wetherill Concordia (Fig.4.5 i). 27 points were omitted due to common Pb, probable Pb loss and/or due to incorrect core – rim relationships, as outlined in the Methodology (see Chapter 3, Section 3.3.4). Following application of the common Pb correction, the remaining 7 concordant and near-concordant spots were plotted on a $^{206}Pb/^{238}U$ weighted mean plot (Fig.4.5 j).

CL images indicated that the remaining 7 spots were mainly on the cores of small (~<100 µm) grains with only one rim spot (Fig.4.5 a - g). Overall, spots ranged between ~416 Ma and ~424 Ma (Fig.4.5 j). The rim produced an uncorrected $^{206}Pb/^{238}U$ age of 417.4 ± 11.1 Ma (n = 1). Due to the lack of acceptable rims, all 7 spots were included in the $^{206}Pb/^{238}U$ weighted mean age calculation giving a combined core – rim age of 419.1 ± 4.1 Ma (MSWD = 0.25, n = 7), a statistically acceptable population according to Spencer et al. (2016). The oldest core age was ~423 Ma (Fig.4.5 b, j). The significance of age data will be discussed in Chapter 5, Section 5.2.2.2.

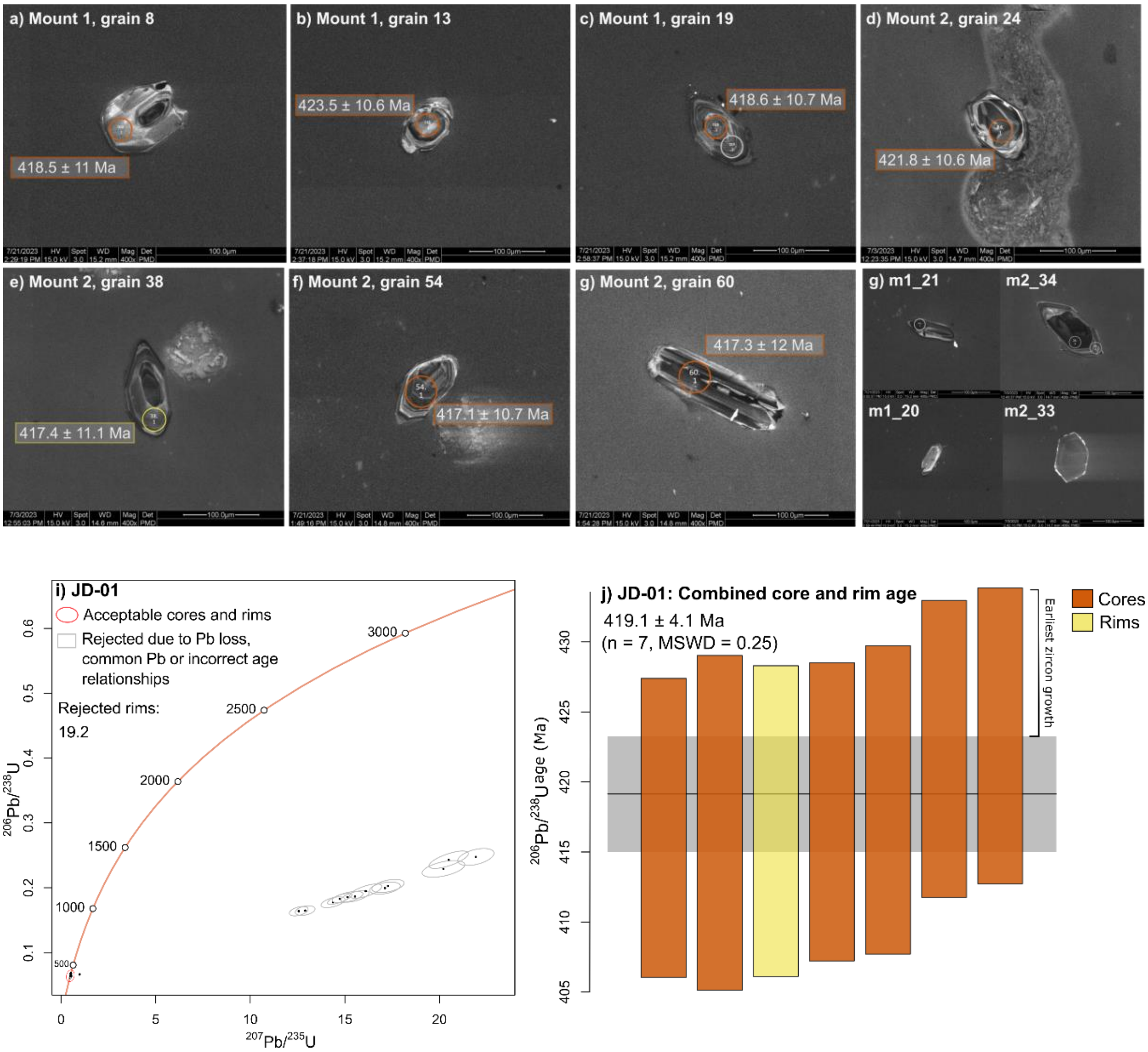

Figure 4.5: CG22-JD-01. (a) – (h) CL images of all analysed grains included in the weighed mean age calculation for JD-01, including six cores (a – d, f, g), one rim (e), grains analysed but rejected due to Pb loss, common Pb and/or incorrect age relations (h – m1_21, m2_34) and grains that were not analysed (h – m1_20, m2_33). Note that m1 refers to JD-01 Mount 1 and m2 refers to JD-02 Mount 2 as outlined in Appendix B, CG22-JD-01_CL images. Uncorrected $^{206}Pb/^{238}U$ ages are labelled for the acceptable analysed rim (yellow) and cores (orange). Ages not labelled for rejected spots (light grey). Higher resolution versions of select CL images are provided in Appendix B_CG22-JD-01. (f) Annotated Wetherill Concordia plot prior to Stacey Kramers common Pb correction, contains all analysed accepted and rejected U-Pb spots. (g) $^{206}Pb/^{238}U$ weighted mean plot following application of common Pb correction. All acceptable concordant and near-concordant rim and core spots are shown. The acceptable rim and all cores are included in the JD-01 weighted mean age.

4.2.2.2. SM-02

A total of 70 grains were mounted for SM-02. Following grinding, polishing and laser spot selection, 22 of these grains were deemed suitable for laser ablation (Appendix B_CG22-SM-02_CL images, Appendix C_zircon textures – table 5). Overall, SM-02 zircons are texturally heterogeneous. Most analysed grains are subhedral in shape (Fig.4.6 a - e). In most grains, cores cannot be distinguished from rims due to complex internal structures (Fig.4.6 c). Where cores and rims can be distinguished, the core to rim boundary is poorly defined and most cores are larger than overgrowths (Appendix C - table 5). However, cores are smaller than overgrowths in some grains. Zircons range from *c.* 75 µm – *c.* 275 µm in length. Most grains are unfractured (Fig.4.6 a, d), however, where observed, grains are lightly to heavily fractured (Appendix C - table 5). Localised alteration and/or recrystallisation is observed and is closely associated with fractures and inclusions in most grains (Fig.4.6 b, c, e – 12).

SM-02 cores are complex and texturally semi-homogeneous or heterogeneous (Fig.4.6 a, b, d). Cores are unzoned, faintly zoned or prominently zoned across those few grains in which cores can be defined (Appendix C - table 5). Sector zoning dominates in cores. Most cores exhibit sub-rounded complex shapes (Fig.4.6 a). Potential partial resorption is observed along the core – rim boundary in one grain (Fig. 4.6 c). Oscillatory zoning is mostly patchy in the magmatic overgrowths (Fig.4.6 a – d) though highly prominent or faint (Fig.4.6 d) in a few grains. Sector zoning is also observed (Fig.4.6 d). Those grains identified as unsuitable for laser ablation were rejected based on the heavy fracturing as well as many of these grains being too small or complexly zoned to fit a 30 µm laser spot. Most rejected grains are also partially altered and/or recrystallised (Fig.4.6 e – 1, 17)

A total of 41 points (n = 41) over 21 grains were analysed for SM-02 (Appendix B_CG22-SM-02; Appendix D). Most concordant and near concordant spots plot between ~401 Ma and ~416 Ma on the Wetherill concordia (Fig.4.6 f). 27 points were omitted due to common Pb, probable Pb loss and/or due to incorrect core – rim relationships (Fig.4.6 f) as outlined in the Methodology (see Chapter 3, Section 3.3.4). Following application of the Stacey Kramers common Pb correction (Stacey and Kramers, 1975), the remaining 14 concordant and near-concordant spots were plotted on a $^{206}Pb/^{238}U$ weighted mean plot (Fig.4.6 g).

Following close investigation of zircon textures for the remaining 14 spots, those interpreted to have grown during emplacement were texturally defined as spots positioned on the outermost rims (x 2) and “inner” rims (x 1) of grains (Fig.4.6 a, b). An “inner rim” spot was included in the age calculation due to the lack of acceptable outermost rims in SM-02 zircons. A total of 3 rim spots were identified and interpreted as most representative of emplacement growth with uncorrected $^{206}Pb/^{238}U$ ages of 406.8 ± 4.7 Ma, 407.1 ± 4.7 Ma and 409.8 ± 5.6 Ma (Fig.4.6 a, b). The $^{206}Pb/^{238}U$ weighted mean age of the 3 rim spots is 407.8 ± 2.9 Ma (MSWD = 0.53, n = 3) which is a statistically acceptable population according to Spencer et al. (2016).

After emplacement spot selection and the weighted mean calculation, a total of 11 spots remained, all positioned on the cores of grains with poorly defined core – rim boundaries (Fig.4.6 b - d, g). The youngest 5 core spots plotted between ~400 Ma and ~410 Ma (Fig.4.6 g), three of which fell within the confidence interval of the weighted mean age interpreted to represent an appropriate time of emplacement (Fig.4.6 b, d). The oldest 6 core spots formed a visibly older spread between ~411 Ma and ~416 Ma (Fig.4.6 g), are outwith the confidence interval of the weighted mean age and are interpreted as representing antecrystic zircon growth (Fig.4.6 a, c).

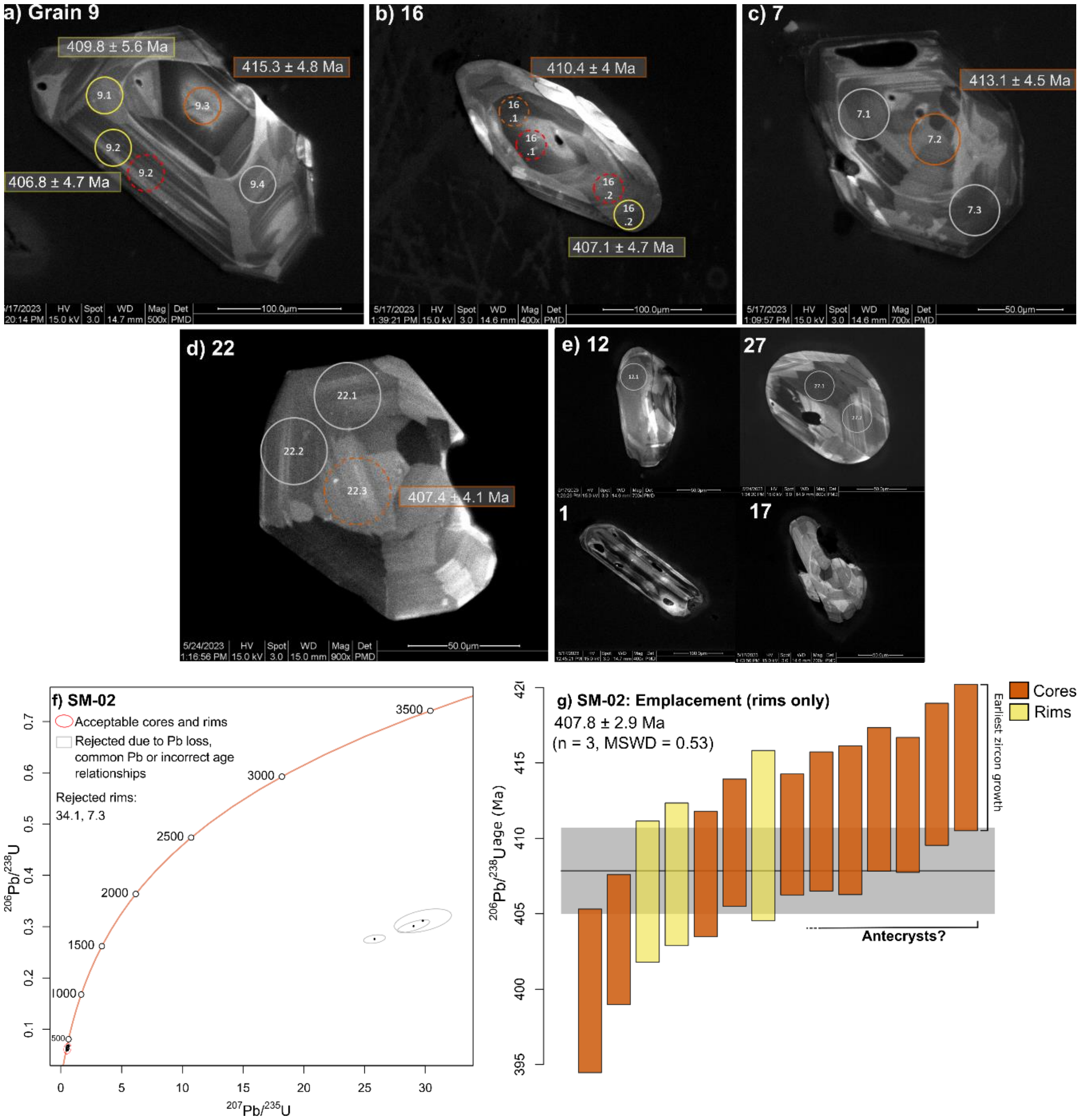

Figure 4.6: CG22-SM-02. (a) – (e) CL image of analysed and acceptable zircons (a – b), grains addressed in text (c, d), grains analysed but rejected (e – 12, 27) and grains that were not analysed (e – 1, 17). Uncorrected $^{206}Pb/^{238}U$ ages labelled for emplacement rims (yellow), probable Pb loss cores (dashed orange) and antecrystic cores (solid orange). The earliest zircon crystallised in SM-02 is presented (a – 9.3). Ages not labelled for rejected spots (light grey). Potential spots for future trace element analysis labelled (dashed red). Higher resolution versions of select CL images are provided in Appendix B_CG22-SM-02_CL images. (f) Annotated Wetherill Concordia plot prior to the Stacey Kramers common Pb correction, containing all analysed acceptable and rejected U-Pb spots. Rims rejected at the age calculation stage due to evidence of Pb loss in Iolite are listed and are not plotted on the weighted mean plot. (g) $^{206}Pb/^{238}U$ weighted mean plot following application of common Pb correction. All rims included in the weighted mean calculation for SM-02.

4.2.2.3. BG-01

A total of 200 zircon grains were mounted for BG-01. 31 of these grains were deemed suitable for laser ablation (Appendix B_CG22-BG-01_CL images, Appendix C_zircon textures – table 1). Detailed descriptions for all zircons yielded from BG-01 are provided in Appendix C - table 1. Analysed grains are dominantly euhedral in shape (Fig.4.7 b, d) with only a few subhedral grains observed (Fig.4.7 a, c). Generally, cores and magmatic overgrowths could be distinguished in each grain (Fig.4.7 a – d). Zircons within BG-01 range from 40 µm – 138 µm in width. Cores are larger than rims in most grains (Fig.4.7 c, d). Fractures were also observed in most grains (Fig.4.7 c, e) and are possibly related to the proximity of BG-01 to a mapped fault. CL images indicate alteration, closely associated with fractures in some grains (Fig.4.7 c, e – B1_5, B2_20).

BG-01 zircon cores are broadly heterogeneous (Fig.4.7 a - d). Cores vary from unzoned to faintly zoned to prominently zoned. Where present, core zoning includes oscillatory and sector patterns and is often patchy. Most cores are euhedral with a few exceptions where cores are resorbed and exhibit complex shapes (Fig.4.7 c). In most grains, oscillatory zoning was most prominent in the overgrowths (Fig.4.7 a, b, d). Faint sector zoning was occasionally observed (Fig.4.7 d). Rejected and not analysed grains were moderately to heavily fractured and were more altered, recrystallised and/or resorbed (Fig.4.7 e – B1).

A total of 59 points (n = 59) over 31 grains were analysed for BG-01 (Appendix B_CG22-BG-01; Appendix D). Most concordant and near concordant points plot between ~407 Ma and ~417 Ma on the Wetherill Concordia (Fig.4.7 f). 40 points were omitted due to common Pb, probable Pb loss, because spots were significantly older than interpreted emplacement-related spots, spots were not on the outermost rims of grains and/or due to incorrect core – rim relationships as outlined in the Methodology (see Chapter 3, Section 3.3.4). After application of the Stacey Kramers common Pb correction (Stacey and Kramers, 1975), the remaining 19 concordant and near-concordant spots were plotted on a $^{206}Pb/^{238}U$ weighted mean plot (Fig.4.7 g).

Following close investigation of zircon textures for the remaining 19 spots, those interpreted to have grown during emplacement were texturally defined as spots on the outermost rims of grains (Fig.4.7 a, b). A total of 6 texturally acceptable rim spots were identified and interpreted as most representative of emplacement growth, ranging between ~407 Ma - ~414 Ma (Fig.4.7 g). The $^{206}Pb/^{238}U$ weighted mean age of the 6 rim spots is 410.2 ± 1.7 Ma (MSWD = 1.4, n = 6) which is a statistically acceptable population according to Spencer et al. (2016).

After emplacement spot selection and the weighted mean calculation, a total of 13 core spots remained (Fig.4.7 g). The youngest 2 spots (~402 Ma) plotted outwith the confidence interval of the weighted mean age (Fig.4.7 g). The next youngest 6 spots plotted between ~409 Ma and ~412 Ma fell within the confidence interval of the weighted mean age interpreted to represent an appropriate time of emplacement (Fig.4.7 g). The oldest 5 core spots plotted between ~413 Ma and ~423 Ma, are outwith the confidence interval of the weighted mean age and are interpreted as representing antecrystic zircon growth (Fig.4.7 a – 9.3).

The omitted oldest spot with an uncorrected $^{206}Pb/^{238}U$ age of 426.4 ± 6.6 Ma (Fig.4.7 b, f) is significantly older and outwith analytical error of the weighted mean age and might predate final deposition into the Southern Uplands prism, thus is interpreted as representative of xenocrystic zircon growth.

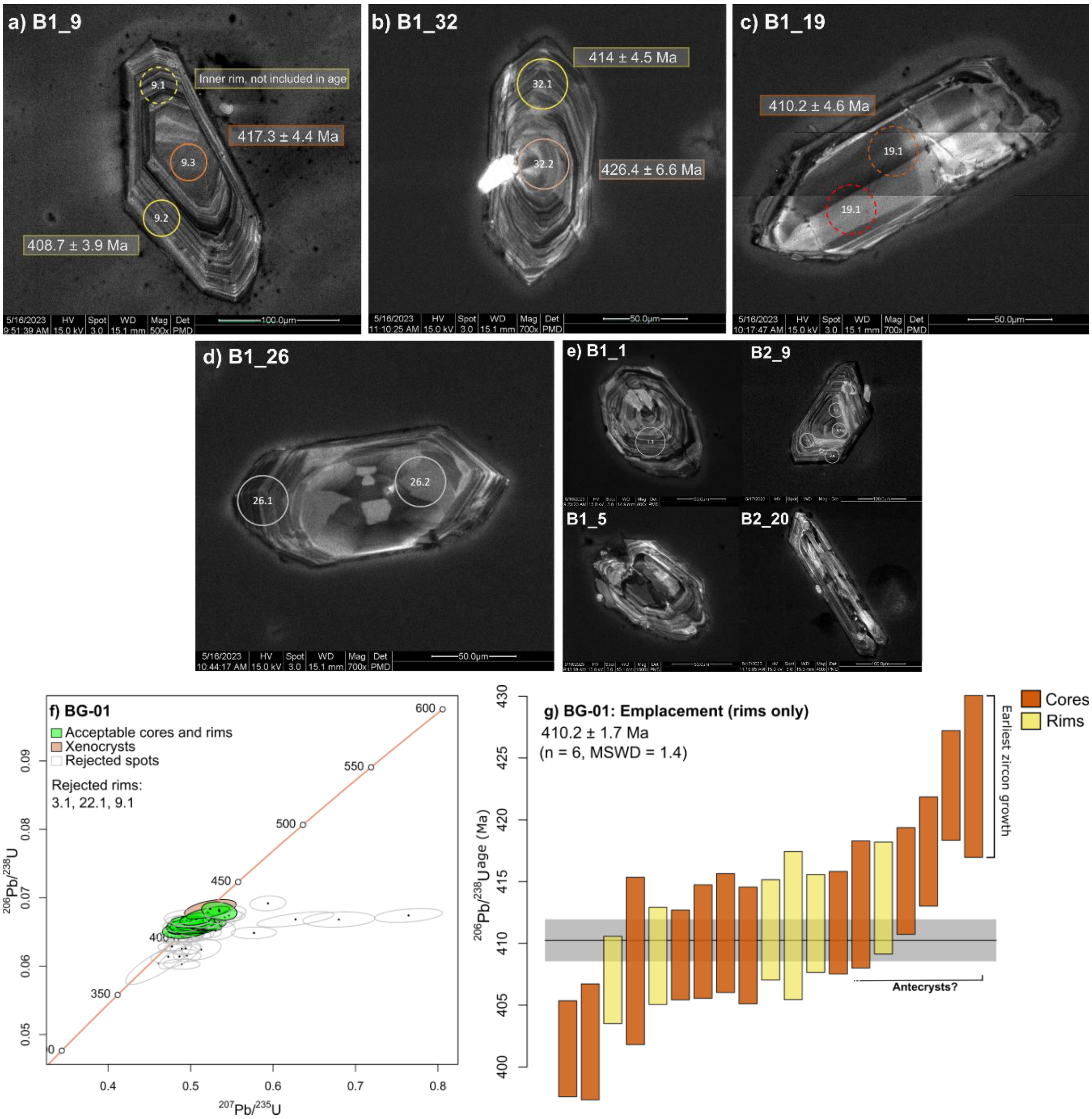

Figure 4.7: CG22-BG-01. (a) – (e) CL images of analysed and acceptable zircons (a, b), grains directly mentioned in text (c, d), analysed but rejected (e – B1_1, B2_9) and zircons not analysed (e – B1_5, B2_20). Uncorrected $^{206}Pb/^{238}U$ ages labelled for emplacement rims (yellow), older, possible antecrystic rims (dashed yellow), antecrystic cores (orange), probable Pb loss cores (dashed orange) and xenocrysts (beige). Ages not labelled for rejected spots (light grey). Potential trace element spots for future analysis are annotated (dashed red). Higher resolution versions of select CL images are provided in Appendix B_CG22-BG-01_CL images. (f) Annotated Wetherill Concordia plot shown prior to Stacey Kramers common Pb correction, contains all analysed acceptable and rejected U-Pb spots. Three rims were rejected due to Pb loss and the suspicion that one rim is antecrystic (a – 9.1). (g) $^{206}Pb/^{238}U$ weighted mean plot following application of common Pb correction. All acceptable concordant and near-concordant rims and cores are shown. All acceptable rims are included in the BG-01 weighted mean age.

4.2.2.4. SM-01

A total of 65 grains were picked and mounted for SM-01. 3 of these grains were identified as suitable for laser ablation (Appendix B_CG22-SM-01_CL images, Appendix C_zircon textures – table 4). Grains are euhedral to subhedral, and smaller cores can be distinguished from larger magmatic overgrowths in all grains (Fig.4.8 a - c). Grains are approximately 130 µm, 250 µm and 313 µm in length. Very light to light fracturing is observed. Localised loss of zonation is observed in all grains, associated with fractures (Fig.4.8 a – c).

SM-01 zircon cores are semi-homogeneous to heterogeneous and vary from unzoned to faintly zoned (Fig.4.8 a - c). Oscillatory zoning dominates cores. Cores exhibit both round and subrounded shapes. An inherited core is observed in grain 2 (Fig.4.8 b). Potential recrystallisation and/or resorption is observed at the core - rim boundary and within the outer magmatic overgrowth of this grain, spatially related to a fracture (Fig.4.8 b). Heterogeneous oscillatory zoning is observed in all magmatic overgrowths (Fig.4.8 a – c).

A total of 9 points (n = 9) over three grains were analysed for SM-01 (Appendix B_CG22-SM-01; Appendix D). Most concordant and near concordant points plot between ~404 Ma and ~418 Ma on the Wetherill concordia (Fig.4.8 d). 4 points were omitted due to common Pb and because spots were significantly older than expected emplacement-related spots, as outlined in the Methodology (see Chapter 3, Section 3.3.4). Following application of the Stacey Kramers common Pb correction (Stacey and Kramers, 1975), the remaining 5 concordant and near-concordant spots were plotted on a $^{206}Pb/^{238}U$ weighted mean plot (Fig. 4.8 e).

Following close investigation of zircon textures for the remaining 5 spots, those most likely to have grown during emplacement were texturally defined as spots positioned on the “inner rims” (Fig.4.8 b). These “inner rim” spots were included in the weighted mean age calculation as there were no acceptable outermost rim spots for SM-01. A total of 3 rim spots in only one grain were identified, with uncorrected $^{206}Pb/^{238}U$ ages of 407.9 ± 3.7 Ma, 412.6 ± 3.2 Ma and 416.4 ± 4.4 Ma (Fig.4.8 b). The $^{206}Pb/^{238}U$ weighted mean age of the 3 rim spots is 411.5 ± 2.1 Ma (MSWD = 5.7, n = 3) which is not a valid statistical population (Spencer et al. 2016). Including only the two youngest “inner rim” spots gave a $^{206}Pb/^{238}U$ weighted mean age of 410.2 ±

2.4 Ma (MSWD = 6.9, n = 2) which is also statistically unacceptable. See Chapter 5, Section 5.2.2.2. for a discussion on the significance and caveats of ages.

Two core spots remained, the youngest of which was younger than and fell outwith the confidence interval of the weighted mean age interpreted as representing an appropriate time of emplacement (Fig.4.8 e) and within the confidence interval of the youngest 2 rims age. It gave an uncorrected $^{206}Pb/^{238}U$ age of 404.1 ± 4.1 Ma (Fig.4.8 a). The oldest core spot was positioned on a small grain (~50 µm wide; Fig.4.8 c) with continuous zoning throughout. It gave an uncorrected $^{206}Pb/^{238}U$ age of 418.1 ± 3.5 Ma that is older and outwith the confidence interval of both weighted mean ages and is interpreted as representing antecrystic growth.

It is highly probable that the overall oldest omitted spot with an uncorrected $^{206}Pb/^{238}U$ age of 886.0 ± 12.1 Ma (Fig.4.8 b, d) is xenocrystic.

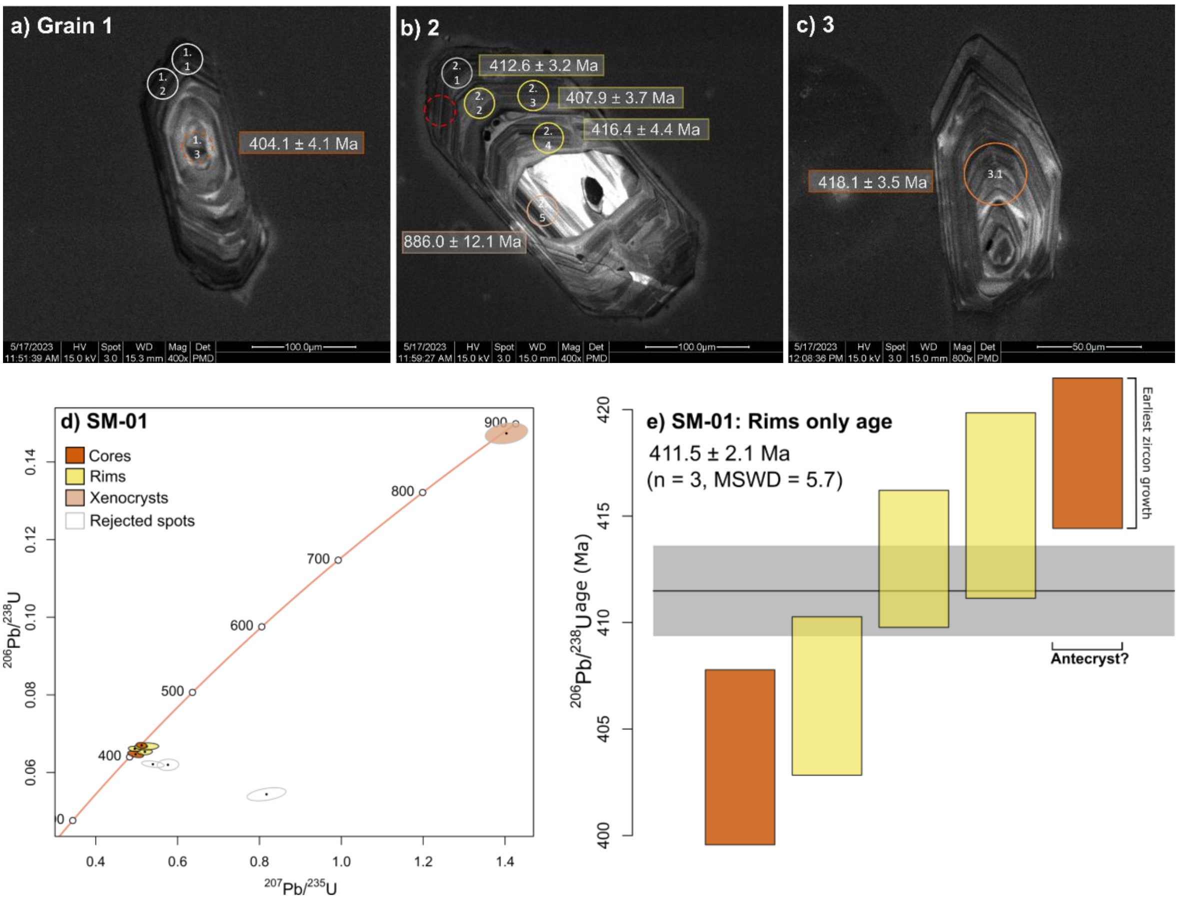

Figure 4.8: CG22-SM-01. (a – c) CL images of all grains analysed for SM-01. Acceptable rims (yellow), cores (orange), probable Pb loss cores (dashed orange) and xenocrysts (beige) are shown. Uncorrected $^{206}Pb/^{238}U$ ages are labelled for the acceptable analysed rims and cores. Ages not labelled for rejected spots (light grey). Spots for future trace element analysis labelled (dashed red). Higher resolution versions of select CL images are provided in Appendix B_CG22-SM-01_CL images. (d) Wetherill Concordia plot prior to Stacey Kramers common Pb correction, contains all analysed accepted and rejected U-Pb spots. (g) $^{206}Pb/^{238}U$ weighted mean plot following application of common Pb correction. All acceptable concordant and near-concordant rim and core spots are shown.

4.2.3. Cheviot

4.2.3.1. CH-01

A total of 117 grains were mounted for CH-01 and 54 were deemed suitable for laser ablation after grinding, polishing and laser spot selection (Appendix B_CG23-CH-01_CL images, Appendix C_zircon textures – table 2). Most grains are subhedral (Fig.4.9 a - e). Cores and rims can be distinguished in most grains, though some have continuous oscillatory zoning or more complex internal structures (Fig.4.9 b; Appendix C - table 2). Zircons range from 95 µm – 350 µm in length. The core to rim size is variable (Fig.4.9 a – e). In most grains, the core is larger (Appendix C – table 2, e.g., grains 1, 7, 8, 14) or is of equal size (Appendix C – table 2, e.g., grains 6, 26, 32) to the overgrowth. Most grains are lightly fractured (Fig.4.8 e – 3, 5). Alteration, recrystallisation and/or resorption is associated with fractures and inclusions in most grains (Fig.4.9 b, c, e). Small inclusions are common throughout all grains.

Cores textures in CH-01 are variable with some exhibiting homogeneous textures (Fig.4.9 a, e – 32) whilst others are heterogeneous (Fig.4.9 b, d, e – 40). Cores vary from unzoned to faintly zoned. Both oscillatory and sector zoning are observed (Appendix C - table 2). Zoning is generally patchy (Appendix C - table 2 e.g., grain 45, 62). Most cores exhibit complex shapes with only a few euhedral cores observed. Partial resorption is observed along several core – rim boundaries (Fig.4.9 e - 3). Magmatic overgrowths in CH-01 zircons contain heterogeneous oscillatory zoning (Fig.4.9 a – e). Sector and convolute zoning (Fig.4.9 e – 3) are also observed. Both faint and prominent zoning is observed in zircon overgrowths (Appendix C - table 2). Those grains deemed as unsuitable for laser ablation (Appendix C – table 2) were rejected based on individual zones measuring <30 µm, the moderate – heavy fractured nature of several grains and associated alteration (Fig.4.9 e – 5, 32).

A total of 97 points (n = 97) over 54 grains were analysed for CH-01 (Appendix B_CG23-CH-01; Appendix D). Most concordant and near concordant points plot between ~397 Ma and ~418 Ma on the Wetherill Concordia (Fig.4.9 f). 61 points were omitted due to common Pb, probable Pb loss and/or due to incorrect core – rim relationships as outlined in the Methodology (see Chapter 3, Section 3.3.4). Following application of the Stacey Kramers common Pb correction (Stacey and

Kramers, 1975), the remaining 36 concordant and near-concordant spots were plotted on a $^{206}Pb/^{238}U$ weighted mean plot (Fig.4.9 g).

Following close investigation of zircon textures for the remaining 36 spots, those interpreted as having grown during emplacement were texturally defined as spots positioned on both the outermost rim and some “inner rims”. These “inner rim” spots were included in the weighted mean age as there was no textural evidence for cross-cutting or overlapping of zones and these were some of the only few rims available for CH-01. A total of 9 rim spots were identified ranging between ~397 Ma - ~407 Ma (Fig.4.9 g). The $^{206}Pb/^{238}U$ weighted mean age of the 9 rim spots is 401.6 ± 4.3 Ma (MSWD = 0.44, n = 9) which is a statistically acceptable population according to Spencer et al. (2016). Omitting the two oldest rim spots which texturally do not lie on the outermost overgrowth (Fig.4.9 c, d) gives a $^{206}Pb/^{238}U$ weighted mean age of 400.1 ± 4.7 Ma (MSWD = 0.25, n = 7) which is a statistically acceptable population (Fig.4.9 g). The significance of these ages will be discussed further in Chapter 5, Section 5.2.3.2.

The remaining 27 spots are positioned on zircon cores (Fig.4.9 a, d, g). The youngest 21 spots plotted between ~397 Ma and ~405 Ma and fell within the confidence interval of the weighted mean ages (Fig.4.9 g). The oldest 6 core spots plotted between ~407 Ma and ~417 Ma, are outwith the confidence interval of the weighted mean ages and are interpreted as representing antecrystic zircon growth (Fig.4.9 d, g).

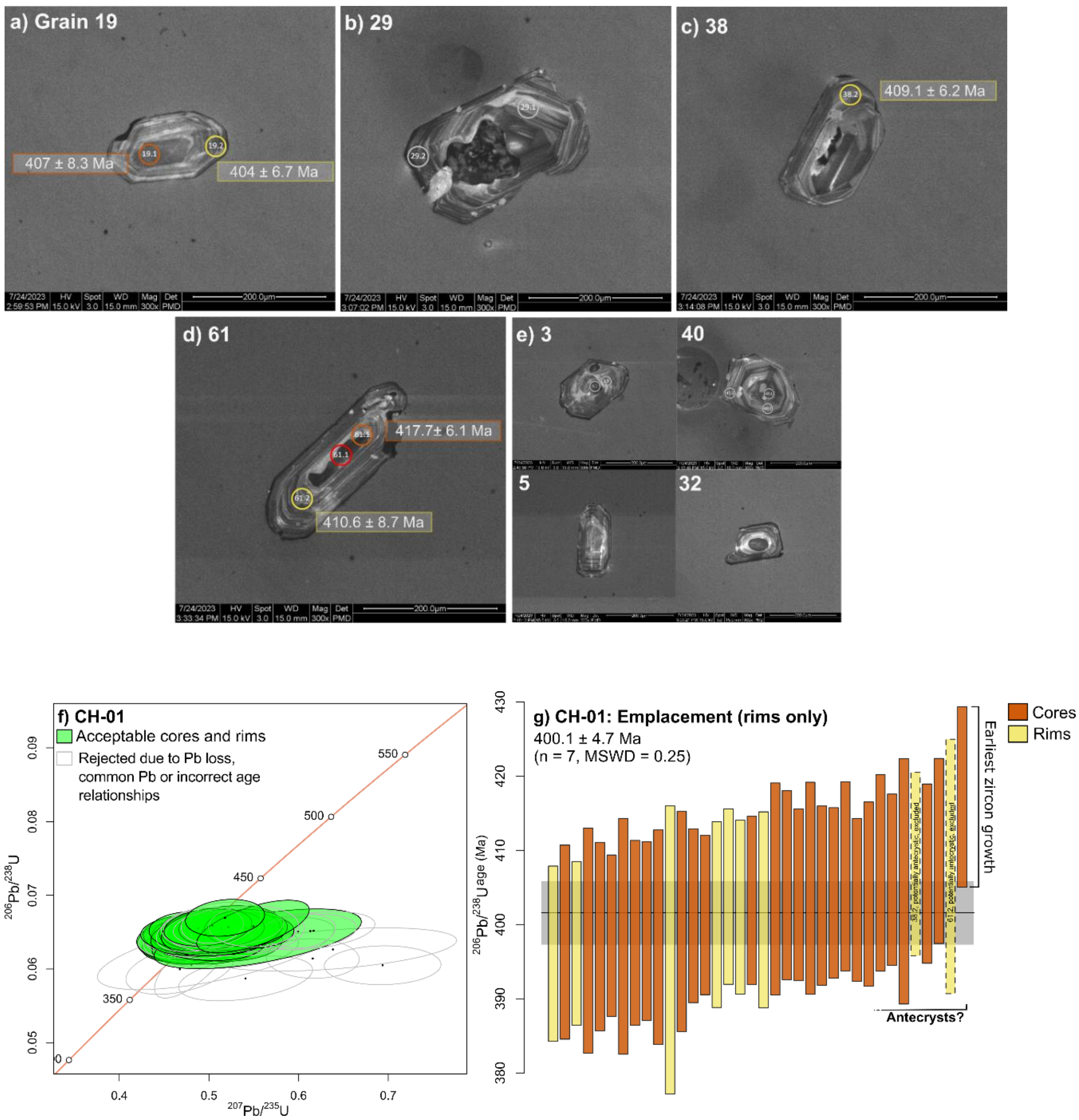

Figure 4.9: CG23-CH-01. (a) – (e) CL images of analysed and acceptable zircons (a), grains directly mentioned in text (b – d), zircons analysed but rejected due to common Pb, Pb loss or incorrect age relations (e – 3, 40) and grains not analysed (e – 5, 32). Uncorrected ^{206}Pb/^{238}U ages labelled for emplacement rims (yellow) and antecrystic cores (orange). Ages are not labelled for rejected spots (light grey). The earliest zircon crystallised in CH-01 is shown (d). Analysed trace element spots are labelled (red). Higher resolution versions of select CL images are provided in Appendix B_CG23-CH-01_CL images. (f) Wetherill Concordia plot prior to Stacey Kramers common Pb correction contains all analysed acceptable and rejected U-Pb spots. (g) ^{206}Pb/^{238}U weighted mean plot following application of common Pb correction. All acceptable concordant and near-concordant rims and cores are shown. The oldest two rims are excluded from the weighted mean age.

4.2.3.2. CH-02

A total of 124 grains were mounted for CH-02 and 56 of these grains were deemed suitable for laser ablation (Appendix B_CG23-CH-02_CL images, Appendix C_zircon textures – table 3). Most grains are subhedral (Fig.4.10 a – e). Cores and rims are observed in most grains in which the core to rim size varies between a small core and a large magmatic overgrowth and vice versa (Fig.4.10 a, b). Grains range from *c.*150 µm – *c.*300 µm in length. Most grains are very lightly fractured (Appendix C – table 3). Alteration is closely associated with fracture and/or inclusions in most CH-02 zircons (Appendix C – table 3).

Cores in CH-02 grains are texturally heterogeneous (Fig.4.10 a, c, d). Most grains are poorly zoned though some faint oscillatory and sector zoning patterns are observed (Fig 4.10 e - 7). Core shapes are variable (Fig.4.10 a - c). Most shapes are complex with only a few euhedral cores observed (Fig.4.10 b). Partial resorption is observed along the core – rim boundary in one grain (Fig.4.10 c). Heterogeneous oscillatory zoning dominated magmatic overgrowths (Fig.4.10 a, b, d). Sector zoning and convolute zoning are present in some grains (Appendix B_CG23-CH-02). Localised recrystallisation and/or alteration is observed within and across many overgrowth zones (Appendix C -table 3). Those grains rejected prior to laser ablation (Appendix C – table 3) were excluded based on small grain size, complex zoning, heavy fracturing and significant alteration (Fig.4.10 e – 15, 83).

A total of 92 points (n = 92) over 56 grains were analysed for CH-02 (Appendix B_CG23-CH-02; Appendix D). Most concordant and near concordant points plot between ~393 Ma and ~414 Ma on the Wetherill Concordia (Fig.4.10 f). 57 points were omitted due to common Pb, probable Pb loss and/or due to incorrect core – rim relationships as outlined in the Methodology (see Chapter 3, Section 3.3.4). Following application of the Stacey Kramers common Pb correction (Stacey and Kramers, 1975), the remaining 35 concordant and near-concordant spots were plotted on a $^{206}Pb/^{238}U$ weighted mean plot (Fig.4.10 g).

Following close investigation of zircon textures for the remaining 35 spots, those interpreted as having grown during emplacement were texturally defined as spots positioned on both the outermost overgrowth and some “inner rims” (see Chapter 3, Section 3.3.4; Fig.4.10 d). A total of 13 rim spots were identified, ranging between

~396 Ma and ~406 Ma (Fig.4,10 g). The $^{206}Pb/^{238}U$ weighted mean age of all 13 spots is 400.3 ± 2.8 Ma (MSWD = 0.34, n = 13) which represents a statistically acceptable population (Spencer et al. 2016). Omitting an older inner rim spot because an outermost rim spot is available (Fig.4.10 g – 90.1), gives a $^{206}Pb/^{238}U$ weighted mean age of 400.0 ± 2.9 Ma (MSWD = 0.35, n = 12) which is a statistically acceptable population according to Spencer et al. (2016). The significance of these ages will be discussed further in Chapter 5, 5.2.3.2.

The remaining 23 spots were positioned on mainly cores and one rim (Fig.4.10 g). The youngest 4 core spots plotted younger than (<~395 Ma) and outwith the confidence interval of the weighted mean age (Fig.4.10 g). The next-youngest 11 core spots plotted between ~397 Ma and ~403 Ma and fell within the confidence interval of the weighted mean age interpreted to represent an appropriate time of emplacement (Fig.4.10 g). The oldest 7 spots plotted between ~403 Ma and ~415 Ma are outwith the confidence interval of the weighted mean age and are interpreted as representing antecrystic zircon growth (Fig.4.10 a, b).

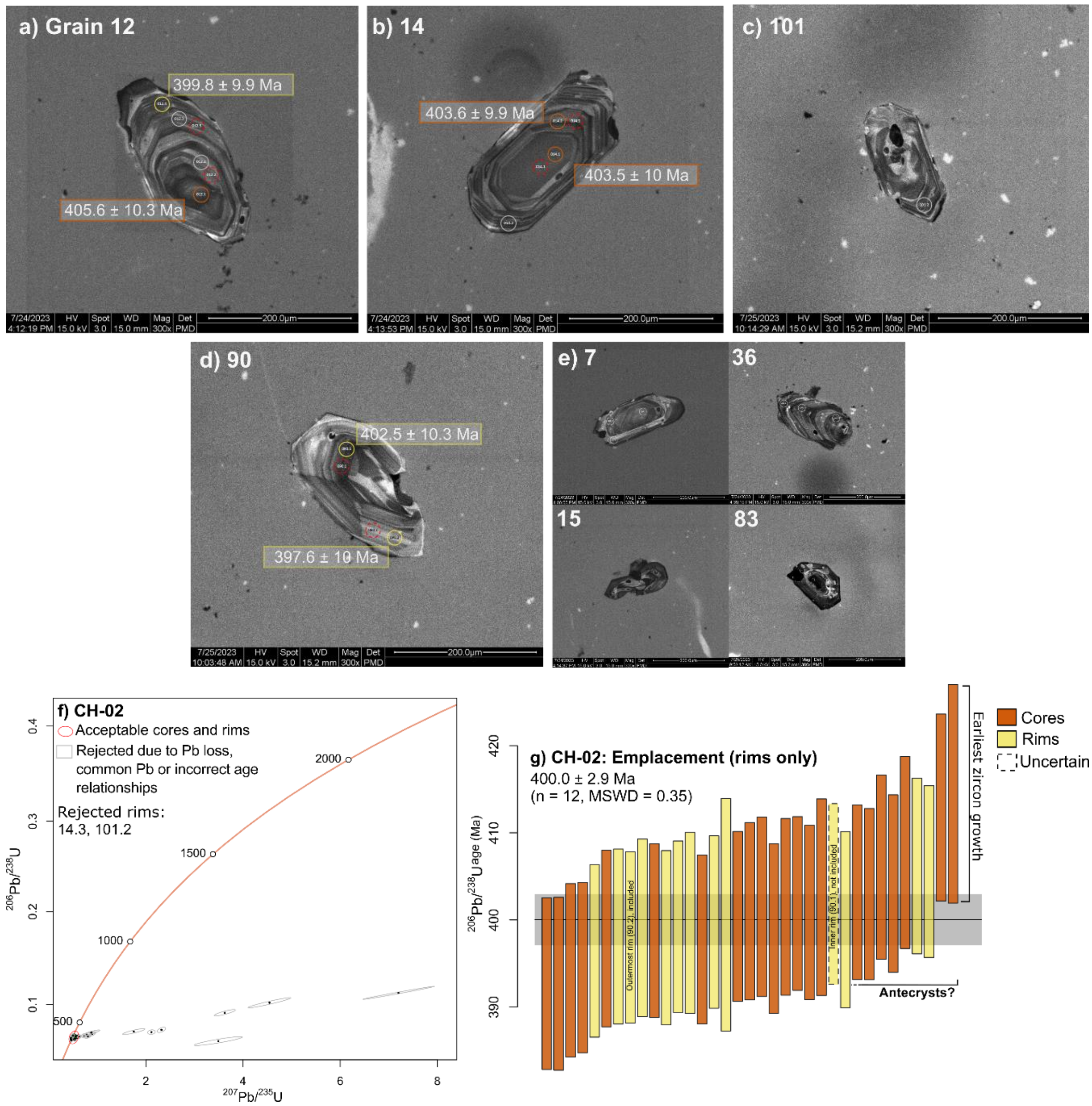

Figure 4.10: CG23-CH-02. (a) – (e) CL images of analysed and acceptable zircons (a), grains directly mentioned in text (b – d), zircons analysed but rejected due to common Pb, Pb loss or incorrect age relations (e – 7, 36) and grains not analysed (e – 15, 83). Uncorrected $^{206}Pb/^{238}U$ ages labelled for emplacement rims (yellow) and antecrystic cores (orange). Ages are not labelled for rejected spots (light grey). Suitable locations for future trace element analysis are labelled (dashed red). Higher resolution versions of select CL images are provided in Appendix B_CG23-CH-02_CL images. (f) Wetherill Concordia plot prior to Stacey Kramers common Pb correction contains all analysed acceptable and rejected U-Pb spots. (g) $^{206}Pb/^{238}U$ weighted mean plot following application of common Pb correction. All acceptable concordant and near-concordant rims and cores are shown. Rims annotated as uncertain (dashed outline) refer to older potentially antecrystic rims as outlined in text.

4.3. Geochemistry

4.3.1. Carsphairn

4.3.1.1. CR-08

A total of 16 core spots were analysed for trace elements in CR-08. A caveat is that 5 spots were positioned on grains in which it was difficult to texturally distinguish between core and rim (Fig.4.11, labelled as "uncertain"). Uncertain spots were previously interpreted as cores; therefore, they are considered as cores here. CR-08 cores are LREE depleted (~0.05 x – 88 x chondritic values) and HREE enriched (up to ~4000 x chondritic values) (Fig.4.11). All core spots exhibit positive Ce and negative Eu anomalies (Fig.4.11). The Ti-in-zircon temperatures of CR-08 cores dominantly range between ~753°C – 851°C, producing a mean Ti-in-zircon temperature of 805.2°C ± 61 °C (2sigma, n = 14). Two cores have significantly higher temperatures of ~909 °C and ~1020 °C. The significance of these anomalous high temperature cores will be discussed in Section 5.2.4.

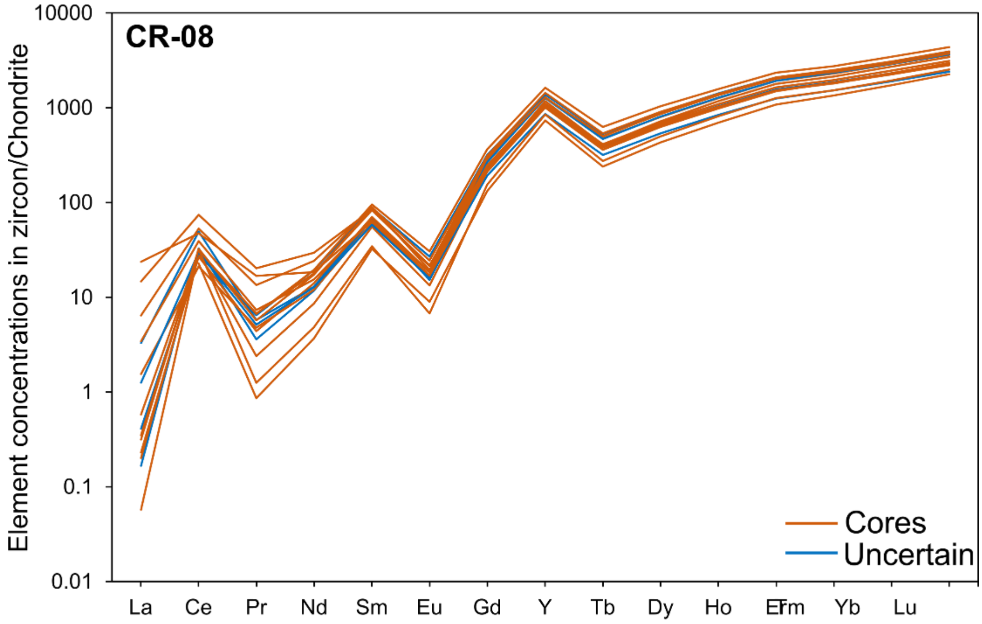

Figure 4.11: Trace element data for CR-08 zircons. Data normalised according to the chondrite values of McDonough and Sun (1995). The spots labelled as uncertain were interpreted as cores with the caveat that cores and rims could not be easily distinguished in these grains. Uncertain spots include CR08_6.1, 34.1, 36.1, 75.1 and 101.1 (see Appendix B – CG23-CR-08_CL images).

4.3.1.2. CR-07

A total of 10 spots were analysed for trace elements in CR-07, including 1 rim spot, 8 core spots and 1 xenocrystic core spot, omitted on the basis that it is not representative of emplacement or antecrystic zircon growth. The CR-07 rim spot was LREE depleted (~0.03 x to ~5.5 x chondritic values), HREE enriched (up to ~3700 x chondritic values) (Fig.4.12 a). This rim gave a Ti-in-zircon temperature of ~704 ºC (Fig.4.12 c). However, this rim provided an uncorrected $^{206}Pb/^{238}U$ age of 424.7 ± 6.6 Ma, so is feasibly part of an antecrystic grain. It will be treated as a core from hereon in.

CR-07 cores are generally LREE depleted (~0.2 x – 57 x chondritic values) and HREE enriched (up to ~2970 x chondritic values). Four core spots are LREE enriched (~8 x – 111 x chondritic values) compared to the rest of the dataset but plot at similar MREE and HREE enrichments (Fig.4.12 a). The Ti-in-zircon temperatures of CR-07 cores generally range between ~723ºC – 828ºC, producing a mean Ti-in-zircon temperature of 763.4ºC ± 84 ºC (2sigma, n = 8). One core has a significantly higher temperature of 1287 ºC (Fig.4.12 b – 27.1) and correlates with a LREE enriched outlier on Figure 4.12 a. All core and rim spots exhibit positive Ce and negative Eu anomalies (Fig.4.12 a). There is a strong negative correlation (R^2 = 0.95) between Ti-in-zircon temperature and chemistry (Fig.4.12 b vs c). The significance of this relationship will be discussed in Section 5.2.4.

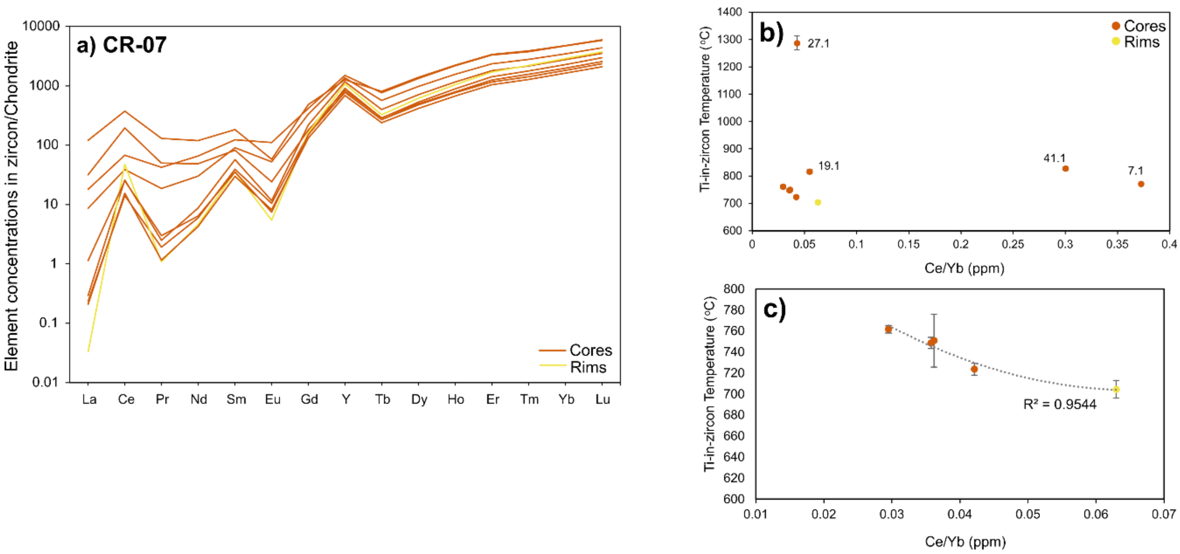

Figure 4.12: CG23-CR-07. (a) Trace element data for CR-07 zircons. (b) Ti-in-zircon temperature vs chemistry plot with outliers. The 4 annotated outliers correlate to the 4 LREE enriched outliers on the chondrite normalised plot. (c) Ti-in-zircon temperature vs chemistry plot with 4 outliers removed. Error bars labelled in (b) and (c) include errors in Ti (ppm) concentration and the Ti-in-zircon temperature equation of Watson et al. (2006).

4.3.2. Cheviot

4.3.2.1. CH-01

A total of 14 spots were analysed for trace elements in CH-01 with the caveat that 1 spot was positioned on a grain in which it was difficult to texturally distinguish between core and rim (Fig.4.13 a). Uncertain spots were previously interpreted as cores (Section 4.2.3.1.), therefore they are considered as cores from hereon. 9 rim spots and 4 other core spots were also analysed for trace elements.

CH-01 rims broadly plot along a LREE depleted (~0.02 x to ~75 x chondritic values) and HREE enriched (up to ~1700 x chondritic values) REE pattern with two visible outliers plotting at anomalous LREE concentrations (up to ~ 2800 x chondritic values) (Fig.4.13 a). CH-01 rims produce Ti-in-zircon temperatures between ~731^{o}C – 961^{o}C (n = 9), producing a mean Ti-in-zircon temperature of 802.7^{o}C ± 157.9 ^{o}C (2sigma, n = 9) (Fig.4.13 b).

CH-01 cores are generally also LREE depleted (~2.5 x – 175 x chondritic values) and HREE enriched (up to ~5400 x chondritic values). Overall, CH-01 cores plot at systematically higher REE values than CH-01 rims, probably a product of the overall evolution of the magmatic system (Fig.4.13 a). The Ti-in-zircon temperatures of CH-01 cores range between ~786^{o}C – 858^{o}C, producing a mean Ti-in-zircon temperature of 817.8^{o}C ± 68 ^{o}C (2sigma, n = 4). Overall, there is no significant difference in temperature between CH-01 rims and cores, although cores broadly have higher Yb concentrations than rims (Fig.4.13 b). Most cores and rim spots exhibit positive Ce and negative Eu anomalies (Fig.4.13 a).

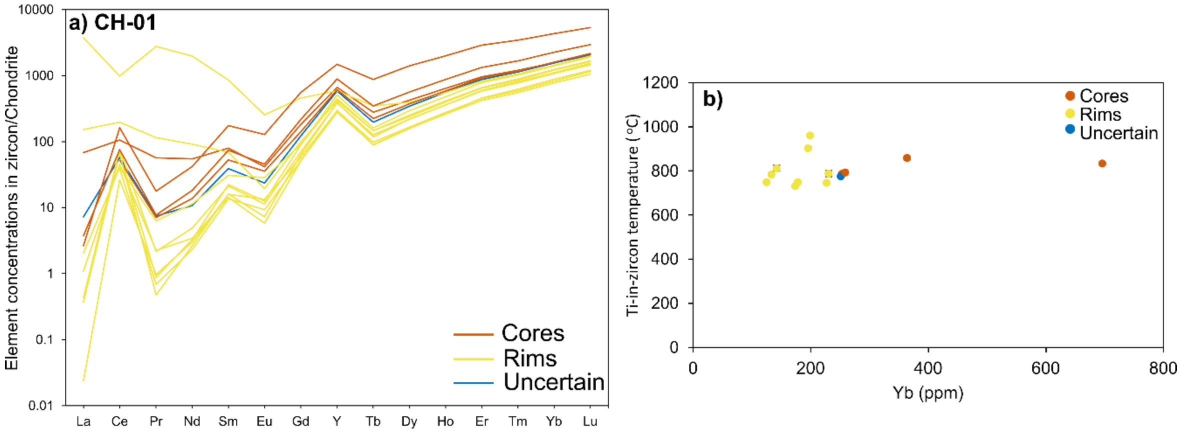

Figure 4.13: (a) Trace element data for CH-01 zircons. Data normalised according to the chondrite values of McDonough and Sun (1995). The spots labelled as uncertain were interpreted as cores with the caveat that cores and rims could not be easily distinguished in these grains. Uncertain spots include CH01_28.1 (see Appendix B – CG23-CH-01_CL images). (b) Ti-in-zircon temperature vs Yb data for analysed trace element spots. Error bars include errors in Ti (ppm) concentration and the Ti-in-zircon temperature equation of Watson et al. (2006).

5. Discussion

5.1. How we interpret appropriate ages of emplacement vs earlier zircon growth

As a reminder of the approach followed for age interpretation (see Chapter 3, Section 3.3.4.), the following points apply:

- Zircon crystallisation ages interpreted as representing appropriate times of **emplacement** were defined by choosing **1)** spots on the outermost overgrowths of grains **2)** spots on the next-inner zone where the outermost overgrowth was too narrow for a ~30 µm spot and/or **3)** spots on small grains (< ~50 µm) with continuous zoning from grain centre to rim. Chosen points were checked by MSWD to determine if they belonged to a statistical single population.

- Cores and occasionally rim spots whose individual spot ages were older and outwith the confidence interval of the weighted mean age interpreted to represent an appropriate time of emplacement, but <~425 Ma were interpreted as **antecrystic**. Chemical similarity between pre-emplacement (i.e., antecrystic) zircons and zircons interpreted to be grown at emplacement gives confidence to their interpretation as antecrystic. An additional consideration is that the maximum possible age of antecrystic growth would correspond with termination of sedimentation in the accretionary prism (~425 Ma). Prior to that time, the Southern Uplands would have been part of the cold fore-arc and magmatism would not be expected. Whilst the justification for defining grains as antecrysts is outlined above, it is important to consider that this interpretation has its own drawbacks due to the limitations of SEM-CL (i.e., only provides image of zircon surface and not the grain at depth) and LA-ICP-MS (i.e., uncertainty around zircon zones ablated at depth) methodology. Alternative analysis such as higher precision multi-collector LA-ICP-MS or ion probe would be required to confirm that cores are definitely antecrysts as opposed to representing autocrysts or Pb loss xenocrysts.

- In turn, **xenocrystic** zircon ages were interpreted as spots with ages >425 Ma. Textural features (e.g., inherited cores) supported xenocrystic interpretation in some samples (Appendix B, C). I am following the definition as per Miller et al. (2007) that a “xenocryst” is a zircon grain that was incorporated into the magma through host rock interaction during upwelling and eventual emplacement. Zircon grains interpreted as xenocrysts are typically older (~a few myrs to many myrs) than those younger zircons interpreted as magmatic and antecrystic or emplacement related.

5.2. Geological interpretation

5.2.1. Cairnsmore of Carsphairn

5.2.1.1. Evidence for relative order of emplacement

Deer (1935) originally proposed a ‘hybridisation model’ for the evolution of Carsphairn, proposing successive emplacement of quartz diorite (‘pyroxene-biotite hybrids’, ‘hornblende hybrids’ of Deer, 1935; CR-08*, this study*) and granodiorite (‘tonalite’ of Deer, 1935; CR-07, *this study*) followed by the microgranite (‘acid hybrid’ of Deer, 1935; CR-06, *this study*) and granite (CR-05, *this study*) based on field relationships, petrography and petrological study (Fig. 2.6). Tindle et al. (1988) supports the original emplacement order and argued on the basis of new field evidence and whole-rock and mineral geochemistry, that Carsphairn was emplaced as 4 phases (Fig. 2.6), beginning with the marginal quartz diorite (CR-08, dated here at 413.8 ± 1.2 Ma) which fractionated in situ to produce the inner granodiorite (CR-07, dated here at 414.0 ± 1.9 Ma or 415.3 ± 1.7 Ma). Further fractionation of magma at depth produced the inner microgranite (CR-06, dated here at 412.0 ± 4.7 Ma) and the innermost coarse-grained granite (CR-05, dated here at 410.5 ± 1.8 Ma). The geochronology data obtained from the four distinct Carsphairn phases**,** each containing varying numbers of concordant Caledonian zircons (Chapter 4.2.1.), are interpreted within this relative framework. Samples are discussed in order of relative emplacement understanding as outlined above.

5.2.1.2. Interpretation of U-Pb zircon geochronology for Carsphairn

The lack of rims in **CR-08** might be explained by CR-08 zircons spending too little time at emplacement depths to grow well developed emplacement rims. The statistically unacceptable cores only age of 413.8 ± 1.2 Ma (n = 31, MSWD = 2.6) is interpreted as probably including a mix of Pb loss cores and true antecrysts (Fig.4.1 g). Therefore, as this age is probably not representative of one geological population (i.e., cannot definitively attribute all grains to emplacement or antecrystic growth), it is interpreted as geologically meaningless, but it is the best possible age for CR-08 with data available in this study. The oldest core with an age of ~421 Ma indicates that the earliest possible onset of magmatism at CR-08 was from ~421 Ma (Fig.4.1 g). A plausible interpretation, based on their similar chemistry, is that CR-08 cores originated from a lower crustal hot zone (i.e., deeper levels) (Section 5.2.4.).

If all rim spots (n = 9) in **CR-07** are of one emplacement-related population, then the zircon crystallisation age of 415.3 ± 1.7 Ma (n = 9, MSWD = 1.8; Fig.4.2 g) is interpreted as representing the time of emplacement. However, if the oldest two rims with uncorrected $^{206}Pb/^{238}U$ ages of 419.5 ± 5.2 Ma (see Appendix D, CR-07_20.1) and 424.0 ± 7.7 Ma (CR-07_70.1) are omitted on the suspicion that they are antecrystic, this leaves a crystallisation age of 414.0 ± 1.9 Ma (n = 7, MSWD = 0.3) interpreted to represent an appropriate time of emplacement. The statistical overlap in ages between CR-08 (413.8 ± 1.2 Ma) and the lowest n age of CR-07 (414.0 ± 1.9 Ma) supports Tindle et al's (1988) interpretation that the marginal quartz diorite (CR-08, *this study*) fractionated in-situ to produce the inner granodiorite (CR-07, *this study*). Textures (Fig.4.2 a – e) and overall age statistics (Fig.4.2 g) provide confidence that all included zircon rims belong to one population. The youngest CR-07 core spots are within the confidence interval of the weighted mean age interpreted to represent an appropriate time of emplacement (Fig.4.2 g)**.** The oldest core spots which range from ~417 Ma to ~424 Ma and lie outwith the time of emplacement confidence interval are interpreted as representing antecrystic zircon growth (Fig.4.2 g). Therefore, the earliest onset of zircon crystallisation as indicated by cores is ~424 Ma for CR-07. Similar REE patterns between the one rim (Section 5.2.4.) and core spots support the plausible interpretation that these cores probably originate from the same magmatic system as CR-07 rims.

The weighted mean rims only zircon crystallisation age of 412.0 ± 4.7 Ma (n = 5, MSWD = 0.73) for **CR-06** is interpreted as representing an appropriate time of emplacement (Fig.4.3 g). This age is in the correct order relative to CR-05 (below) and CR-07 and CR-08 zircon crystallisation ages interpreted as representing appropriate times of emplacement, supportive of the interpretation of Tindle et al. (1988). Textures (Fig.4.3 a – e) and overall age statistics (Fig.4.3 g) provide confidence that all included zircon rimsbelong to one population, interpreted here as an emplacement population. The youngest CR-06 core these spots (~407 Ma **-** ~417 Ma) fall within the confidence interval of the weighted mean age interpreted to represent an appropriate time of emplacement. It is outwith the scope of this study to determine the reason for this. (Fig.4.3 g). The oldest core spots (~419 Ma to ~424 Ma) lie outwith the age of emplacement confidence interval, and are interpreted as antecrysts(Fig.4.3 g). The earliest onset of zircon crystallisation determined from cores is therefore ~424 Ma for CR-06 (Fig.4.3 g).

The weighted mean rims only zircon crystallisation age of 410.5 ± 1.8 Ma (MSWD = 0.78, n = 13) is interpreted as best representative of the time of emplacement of **CR-05** (Fig.4.4 g). Zircon textures (Fig.4.4 a – e) and overall age statistics (i.e., acceptable MSWD) provide confidence that all included zircon rims belong to one population, interpreted here as the emplacement population. The youngest CR-05 core spots (~407 Ma **-** ~411 Ma) fell within the confidence interval of the weighted mean crystallisation age interpreted as representing the time of emplacement and a definite reason for this cannot be determined in this study (Fig.4.4 g). The oldest core spots (~414 Ma **-** ~422 Ma), plotting outwith the confidence interval of the age interpreted to represent an appropriate time of emplacement, are interpreted as antecrysts (Fig.4.4 g). The earliest onset of zircon growth determined from cores in CR-05 is therefore ~422 Ma (Fig.4.4 g).

All Carsphairn samples contain xenocrystic zircons (see Section 4.2.1). CR-05 and CR-08 only contain a few xenocrystic spots whereas CR-06 contains a wide spread of xenocrystic spots (~440 Ma – 1,450 Ma) (Fig.4.3 f)**.** CR-07 also contains a spread of Caledonian xenocrystic spots (*c.* 453 – *c.* 425 Ma; Fig.4.2 f). Caledonian zircons were probably transported and deposited into the Southern Uplands accretionary prism whilst sedimentation was ongoing, but older xenocrystic zircons probably date back to a distinct geodynamic environment, before the Southern Uplands accretionary prism formed (from *c.* 455 Ma Oliver et al. 2008). Previous studies (Waldron et al. 2014, 2008) have identified a dominantly Laurentian provenance for Mesoproterozoic and Paleoproterozoic detrital zircons from across the Southern Uplands, thus some of the xenocrystic zircons of Carsphairn may also be of Laurentian provenance.

5.2.1.3. Integration of all Carsphairn data

The new data presented in this study indicate that three zones of the Carsphairn pluton crystallised and were likely emplaced between ~410 Ma and ~415 Ma (Table 5.1). The data presented support previous field emplacement and petrogenetic understanding (Deer, 1935; Tindle et al. 1988). CR-07, CR-06 and CR-05 crystallisation ages interpreted as representing appropriate times of emplacement, do not overlap with the original Rb-Sr age of 418.6 ± 4.1 Ma for Carsphairn (updated according to Villa et al. 2015), representing a mean of 2 samples, one from the mapped quartz diorite zone (Thirlwall classes as 'tonalite', CR-08 of this study) and the other from the granodiorite zone (classes as ‘Adamellite’, CR-07 of this study) (Thirlwall, 1988). However, a caveat to Rb-Sr dating is that it can produce ages that are older than the actual age interpreted to represent an appropriate time of emplacement, due to mixing of different magmatic suites with their own isotopic signatures and a lack of isotopic equilibration between both at or near emplacement (Nebel, 2013). These new data indicate that the onset of magmatism below Carsphairn occurred from as early as ~424 Ma (Table 5.1), followed by the first emplacement event ~9 myr later. Alternatively, others might argue that the U-Pb ages are too young and have all to some extent been affected by small amounts of Pb loss. The ultimate solution to this problem would be to conduct careful chemical pre-treatment of zircons using chemical abrasion methods (Widmann et al. 2019; Yang et al. 2024).

Table 5.1: $^{206}Pb/^{238}U$ weighted mean crystallisation ages interpreted as representing suitable times of emplacement for each sample analysed in this study. All samples marked with an Asterix (*) indicate ambiguous samples for which a highly confident crystallisation age could not be reached using available data. All ages presented were calculated following application of the Stacey Kramers common Pb correction. Multiple ages are provided where necessary, as discussed in text (e.g., CR-07, SM-01).

Sample	Final $^{206}Pb/^{238}U$ age interpreted as an appropriate time of emplacement	Earliest onset of magmatism
CR-08	*413.8 ± 1.2 Ma (n = 31, MSWD = 2.6)	~421 Ma
CR-07	414.0 ± 1.9 Ma (n = 7, MSWD = 0.3,)	~424 Ma
	415.3 ± 1.7 Ma (n = 9, MSWD = 1.8)	
CR-06	412.0 ± 4.7 (n = 5, MSWD = 0.73)	~424 Ma
CR-05	410.5 ± 1.8 (n = 13, MSWD = 0.78)	~422 Ma
JD-01	*419.1 ± 4.1 Ma (n = 7, MSWD = 0.25),	~423 Ma
SM-02	407.8 ± 2.9 Ma (n = 3; MSWD = 0.53)	~416 Ma
BG-01	410.2 ± 1.7 Ma (n = 6, MSWD = 1.4)	~423 Ma
SM-01	*411.5 ± 2.1 Ma (n = 3, MSWD = 5.7)	~418 Ma
	*413.9 ± 2.6 Ma (n = 2, MSWD = 0.86).	
	*410.2 ± 2.4 Ma (n = 2, MSWD = 6.9)	
CH-01	400.1 ± 4.7 Ma (n = 7, MSWD = 0.25)	~418 Ma
CH-02	400.0 ± 2.9 Ma (n = 12, MSWD = 0.35)	~415 Ma

5.2.2. Black Stockarton Moor and Bengairn

5.2.2.1. Field evidence for relative order of emplacement

Previous field observations indicate an emplacement order of JD-01 (phase 1 dykes of Leake and Cooper, 1983) > SM-02 (phase 1 sheets) > BG-01 (supposedly post-dates phase 1 intrusions) > SM-01 (phase 2 dykes). The geochronology data from four BSM samples, each yielding different amounts of concordant Caledonian zircon (Section 4.2.2.), are interpreted within this relative context. Samples are discussed in the emplacement order indicated by field relationships.

5.2.2.2. Interpretation of U-Pb zircon geochronology for Black Stockarton Moor and Bengairn

Field relationships indicate that **JD-01** should be a similar age to or older than SM-02. The statistically acceptable weighted mean rim and core age of 419.1 ± 4.1 Ma (MSWD = 0.25, n = 7) for JD-01 includes only one acceptable rim (see Section 4.2.2.1; Fig.4.5 j) JD-01 zircons are small and are derived from a small minor intrusion at BSM, thus might have been emplaced and cooled too quickly, spending little time at emplacement depths to grow large emplacement rims. There is no obvious age clustering and no consistent textural evidence (e.g., large number of rims) to justify an acceptable crystallisation age and therefore no possible time of emplacement could be determined. The oldest core, with a corrected age of ~423 Ma indicates that the earliest possible onset of magmatism at JD-01 was from ~423 Ma (Fig.4.5 j; Table 5.1).

The $^{206}Pb/^{238}U$ weighted mean rims-only zircon crystallisation age of 407.8 ± 2.9 Ma (MSWD = 0.53, n = 3) is interpreted as best representing an appropriate time of emplacement for **SM-02** (Fig.4.6 g). The small number of acceptable rims is probably caused by rapid cooling at emplacement depths. Whilst this age is statistically acceptable, it should be cautioned that it only includes spots from two grains, two spots within inner and outer rims of grain 9 (Fig.4.6 a) and one on the outermost portion of grain 16 (Fig.4.6 b). Textural ambiguity throughout SM-02 zircons prevents confident distinction between cores vs rims thus, distinction between emplacement vs antecrystic zircon growth, therefore a crystallisation age representing an appropriate time of emplacement could not be determined based on available data (Fig.4.6 g). The oldest core is ~416 Myr old, younger than in JD-01, and thus does not constrain the time of onset of magmatism beneath BSM (Fig.4.6 g).

The weighted mean rims only zircon crystallisation age of 410.2 ± 1.7 Ma (MSWD = 1.4, n = 6) is interpreted as best representing an appropriate time of emplacement for **BG-01** (Fig.4.7 g)**.** Zircon textures (Fig.4.7 a – e) and overall age statistics provide confidence that all included zircon rims belong to one population, interpreted here as the emplacement population. The earliest onset of zircon core growth in BG-01, interpreted as antecrystic, is ~423 Ma (Fig.4.7 g).

SM-01 yielded a low number of small zircons (n = 3) with small rims, again likely due to the sample coming from a small minor intrusion. The weighted mean $^{206}Pb/^{238}U$ all rims age of 411.5 ± 2.1 Ma (n = 3, MSWD = 5.7) for SM-01 does not represent a statistically acceptable population (Fig.4.8 e). A major caveat for SM-01 is that all rim spots are from the same grain (Fig.4.8 b). Excluding the youngest rim spot because it is a similar age to what is a suspiciously young core (Fig.4.8 e) gives an age of 413.9 ± 2.6 Ma (n = 2, MSWD = 0.86). However, there is no clear evidence for Pb loss or textural justification for omitting the youngest rim. Excluding the oldest rim spot because it is similar in age to the oldest core, is positioned on the innermost rims and therefore probably isn't as representative of the time of emplacement, produces an age of 410.2 ± 2.4 Ma (n= 2, MSWD = 6.9). However, the two youngest remaining rims are positioned on the same rim portion of the grain but are very different in age, with spot 2.2 giving an uncorrected age of 412.6 ± 3.2 Ma and spot 2.3 an uncorrected age of 407.9 ± 3.7 Ma (Fig.4.8 b, e). The significance of the youngest two spots is therefore uncertain. There is moderate confidence in the interpretation that the oldest core spot reflects antecrystic zircon growth, because it is older and outwith the confidence interval of all the rims. Therefore, the earliest onset of zircon crystallisation for SM-01 as determined from a zircon core occurred from ~418 Ma which lies within the range of magmatic ages at BSM (Fig.4.8 e).

Xenocrysts were only dated in **BG-01** and **SM-01** at Black Stockarton Moor (Fig.4.7 f; Fig.4.8 d). The individual xenocryst in BG-01 is Caledonian in age, with an uncorrected age of 426.4 ± 6.6 Ma (Fig.4.8 b). The individual SM-01 xenocryst with an uncorrected age of 886.0 ± 12.1 Ma was probably transported and deposited into the prism during active sedimentation, possibly originating from Laurentia (Waldron et al. 2014, 2008). The one zone that the SM-01 spot interpreted to be xenocrystic was posisitioned on (Fig. 4.8, spot 2.5) contained oscillatory zoned and therefore might be igneous in origin.

5.2.2.3. Integration of all BSM zircon data

The exact timescale of emplacement magmatism at BSM is ambiguous and cannot be fully constrained using the new data presented in this study (Table 5.1). Field relationships indicate an emplacement order of JD-01 > SM-02 > BG-01 > SM-01. The JD-01 age of 419.1 ± 4.1 Ma (MSWD = 0.25, n = 7), whilst in line with field relationships (Leake and Cooper, 1983), is anomalous and cannot be related to an entirely antecrystic or emplacement-related population. The SM-02 crystallisation age of 407.8 ± 2.9 Ma (MSWD = 0.53, n = 3), interpreted as an appropriate time of emplacement, contradicts field evidence in that it is younger than the supposed later phases. However, there is low confidence in this age because it was calculated using only two grains. The BG-01 crystallisation age of 410.2 ± 1.7 Ma (MSWD = 1.4, n = 6), interpreted as representing a suitable time of emplacement, is the only age for which there is a high confidence at BSM. Miles et al. (2014) classes the Bengairn pluton as Zone 1 of the adjacent Criffel-Dalbeattie complex **(**Miles et al. 2014 - Figure 2a) and reports a weighted mean $^{206}Pb/^{238}U$ ion microprobe age of 408 ± 14 Ma (n = 9) for this zone. This age overlaps within error of the time of emplacement interpreted for BG-01. However, their Bengairn sample was collected approximately ~20 km from the supposed Bengairn – Criffel contact and >20 km NE of where the BG-01 sample was collected for this study, thus the comparability of the Miles et al. (2014) age to BG-01 remains unclear. SM-01 should be the youngest phase according to field evidence (Leake and Cooper, 1983), however all SM-01 ages presented in this study are older than earlier phases (Table 5.1). There is low confidence that any crystallisation ages for SM-01 represent emplacement because these are based on only one grain. What can be said is that magmatism began as early as ~423 Ma at BSM, with onset of emplacement into the shallow crust occurring ~13 myr later (Table 5.1)

5.2.3. Cheviot

5.2.3.1. Field evidence and relative ages debate

According to Jhingran and Tomkeieff (1942) and Robson's (1976) mapping, CH-01 is of the 'Standrop' facies and CH-02 belongs to the 'Granophyric' variety (Fig. 2.6). Later study (Al-Hafdh, 1985) interpreted both CH-01 and CH-02 to belong to a unified 'Standrop' facies despite earlier observed petrographic differences between the original 'Standrop' and 'Granophyric' varieties within these rocks (Jhingran and Tomkeieff, 1942). Al-Hafdh, (1985) replaced Jhingran and Tomkeieff's (1942) original 'Granophyre' variety with the 'Hedgehope' facies. According to Jhingran and Tomkeieff (1942), the 'Standrop' facies (CH-01, *this study*) was emplaced prior to the 'Granophyric' ('Hedgehope' facies of Al-Hafdh, 1985) variety (CH-02, *this study*). The geochronology data from samples CH-01 and CH-02 are interpreted within this relative context. Both samples have large yields of concordant Caledonian zircons (n = ~50) as outlined in Section 4.2.3.

5.2.3.2. Interpretation of U-Pb zircon geochronology for Cheviot

Per the results above, if the oldest two rims with uncorrected $^{206}Pb/^{238}U$ ages of 409.1 ± 6.2 Ma and 410.6 ± 8.7 Ma are omitted on the suspicion that they are antecrystic, the zircon crystallisation age of 400.1 ± 4.7 Ma (MSWD = 0.25, n = 7) (Fig.4.9 g) is interpreted as representing a suitable time of emplacement. The oldest CH-01 core spots (~407 Ma - ~418 Ma) plotting outwith the confidence interval of the age interpreted to represent an appropriate time of emplacement are interpreted as reflecting antecrystic zircon growth (Fig.4.9 g). The earliest onset of zircon growth in CH-01 as determined from cores is therefore ~418 Ma (Fig.4.9 g).

A statistically acceptable $^{206}Pb/^{238}U$ zircon crystallisation age of 400.0 ± 2.9 Ma (MSWD = 0.35, n = 12) as determined by zircon rims is interpreted as representing an appropriate time of emplacement for CH-02 (Fig.4.10 g). Overall, core ages in CH-02 ranged between ~395 Ma and ~415 Ma. The oldest core spots (~403 Ma - 415 Ma), plotting outwith the confidence interval of the zircon crystallisation age interpreted as representing an appropriate time of emplacement are interpreted as antecrysts (Fig.4.10 g). The earliest onset of zircon growth in CH-02 as determined by zircon cores is ~415 Ma (Fig.4.10 g).

5.2.3.3. Integration of all Cheviot data

Zircon crystallisation ages interpreted as representing appropriate times of emplacement indicate that the Cheviot pluton was crystallised and was likely emplaced at approximately ~400 Ma. Both CH-01 and CH-02 ages statistically overlap (Table 5.1) and overlap with a previous Rb-Sr emplacement age of 403.8 ± 3.0 Ma (n = 3) (Thirlwall, 1988). The new crystallisation ages interpreted as best representing the time of emplacement support Jhingran and Tomkeieff (1942) and Robson's (1976) field-based interpretation that CH-01 and CH-02 are of two petrographically distinct facies (Table 4.1) and are not incompatible with Al-Hafdh (1985) interpretation that the 'Standrop' variety (of Jhingran and Tomkeieff, 1942, *CH-01*) was emplaced before the 'Granophyric' facies (of Jhingran and Tomkeieff, 1942, *CH-02*). Higher precision analysis such as CA-ID-TIMS or chemical abrasion pre-treatment of zircons followed by multi-collector LA-ICP-MS or ion probe analyses is recommended to address any lingering uncertainty over partial Pb loss and to attempt to statistically distinguish the crystallisation ages and thus, time of emplacement of the different facies. New data do currently indicate that the onset of magmatism below the Cheviot pluton occurred from as early as ~418 Ma as determined from zircon cores, followed by the first emplacement event ~18 myr later (Table 5.1).

5.2.4. Interpretation of trace element data

Trace element geochemistry from the dated zircon zones can also contribute to interpretation of geochronological data. The LREE depleted, HREE enriched pattern observed in both Carsphairn (CR-08, CR-07; see Section 4.3.1.) and Cheviot (CH-01; see Section 4.3.2.) is a common REE pattern in zircons caused by the highly incompatible behaviour of LREEs and the highly compatible behaviour of HREEs in zircon (Belousova et al. 2002). The ionic radii of HREEs is smaller than LREEs, thus HREEs can substitute into the zircon crystal lattice a lot easier than LREEs, causing their enrichment (Belousova et al. 2002).

Strong positive Ce anomalies are consistent across most spots in CR-08, CR-07 and CH-01, excluding outliers (Fig.4.11; 4.12 a; 4.13 a). Ce anomalies are generally related to the high oxidation state of magma which causes trivalent Ce^{3+} to become Ce^{4+}. Oxidised Ce is more compatible in zircon, thus can substitute into and will be enriched in the crystal lattice of zircon, causing positive Ce anomalies (Belousova et al. 2002; Loader et al. 2022). Prominent negative Eu anomalies are observed in most spots across CR-08, CR-07 and CH-01, excluding outliers (Fig.4.11; 4.12 a; 4.13 a)**.** Depletion in Eu is usually controlled by the fractionation of plagioclase alongside zircons in the magma. Divalent unoxidised Eu^{2+}, expected in evolved rocks such as granitoids, is much less compatible in zircon than its oxidised variant Eu^{3+}, thus will preferentially enter the crystal lattice of plagioclase (by substituting with Ca^{2+}) over zircon, causing the negative Eu anomalies observed in Carsphairn and Cheviot (Belousova et al. 2002; Loader et al. 2022). LREE enriched outlier spots are observed in CR-07 (Fig.4.12 a) and CH-01 (Fig.4.13 a) are interpreted as accidental laser ablation analysis of LREE-enriched inclusions such as monazite, titanite or allanite (Belousova et al. 2002; Siegel et al. 2018; Burnham, 2020; Loader et al. 2022). Outliers are excluded from further discussion.

The Ti-in-zircon temperatures for analysed trace element spots indicate approximate temperatures of crystallisation of cores, and some rims, in these samples (Siégel et al. 2018). CR-08 cores produced a narrow range of temperatures (~753^{o}C – 851^{o}C, see Section 4.3.1.1.) as do CR-07 cores (~723^{o}C – 828^{o}C, see Section 4.3.1.2.). Ti-in-zircon temperatures are only available for one rim spot in CR-07. This rim produced a temperature (~704 ^{o}C) lower than the respective cores. CR-07 cores exhibit consistent chemistry with only little variation in Ti-in-zircon temperatures with outliers excluded (Fig.4.12 b, c). There is an apparent relationship between Ti-in-zircon temperature and REE ratios once outliers are excluded (Fig.4.12 c), but this is based on very few analyses, thus it would not be appropriate to make broad interpretations.

Temperature ranges for CR-08 and CR-07 cores are quite low, at the lower end of the scale of zircon saturation temperatures (T_{Zr}) for a range of granite types (Miller et al. 2003). The temperatures are broadly supportive of zircon growth at near-solidus conditions, rather than growth in a hotter, more recently mantle-derived batch of magma. Previous amphibole-plagioclase thermometry (see Miles et al. 2013 and refs therein) also support the concept that Southern Uplands magmas may have been stored at near-solidus conditions for a protracted period of time without major influxes of mafic magma at the time of zircon crystallisation.

Trace element analyses of CH-01 zircons do indicate that cores and rims are chemically somewhat distinct, with cores having higher concentrations of REE versus rims, consistent with the overall evolution of the magmatic system from more mafic to more felsic compositions, co-incident with fractionation of REE-loving major and accessory mineral phases (Fig.4.13 a).

The general pattern from these data, albeit limited, is that zircon cores, generally considered to represent antecrystic growth appear to have crystallised at slightly higher temperatures than rims. Furthermore, cores tend to have higher concentrations of REE than rims (Fig.4.13 a). It is key to note that using Ti-in-zircon thermometry as method to determine magma temperature at the time of crystallisation has its own limitations (see Crisp et al. 2023; Schiller and Finger, 2019; Siégel et al. 2018). The accuracy of the Ti-in-zircon temperature results can be negatively influenced by the natural variation in concentrations of TiO_2 in separate zircon grains, alteration triggering Ti concentration reset or poor accuracy of the calibration of the thermometer itself (Fu et al. 2008).

5.3. How do these new data influence existing regional geodynamic models?

5.3.1. Summary of findings

In this section, the new crystallisation ages interpreted as representing appropriate times of emplacement and total durations of zircon growth are integrated with existing data from across the Southern Uplands-Down-Longford Terranes and associated geodynamic models, to determine what impact these new data have. Data for Figure 5.1 were collected for the Southern Uplands-Down-Longford Terrane plutons from available sources and plotted relative to their distance north of the suture and their position along strike of the suture. Distance was measured from the Iapetus Suture to the centre of each body on Digimap. Ages plotted reflect the duration of antecrystic and emplacement related zircon growth in each body (see Table 5.1; Table 5.2).

The key findings are that:

- Zircons interpreted to be grown at emplacement indicate that emplacement growth does not occur earlier than ~419 Ma at any site (Table 5.1).

- There does not appear to be a clear diachroneity in emplacement along strike of the Iapetus Suture (Fig.5.1 a) nor does there appear to be diachroneity to the emplacement from north-south towards the suture (Fig.5.1 b)

- Cores interpreted to represent antecrystsdo not indicate growth earlier than ~424 Ma anywhere across the accretionary prism (Table 5.2), therefore in the broadest terms, the crystallisation of intermediate to felsic magmas capable of zircon saturation does not appear to begin anywhere in the accretionary prism prior to ~424 Ma. The presence and preservation of cores (and occasionally rims) interpreted as antecrysts in most magmatic bodies supports the idea that magmas probably evolved in lower crustal hot zones beneath the Southern Upland Terrane (Cashman et al. 2017; Collins et al. 2020; Jackson et al. 2018). The onset of antecrystic zircon growth, as interpreted from cores, and therefore probably 'hot zone' storage from ~424 Ma coincides with the dominantly compressional tectonic regime, that is the Laurentia – peri-Gondwanan terrane collision (~428 – 423 Ma, see Mendum,

2012) because compressional setting are more likely to favour magma storage at deeper crustal levels (Richards, 2022).

- There is a potential southwards younging pattern in the onset of zircon growth from the northern bodies such as Carsphairn to the Cheviot pluton (Fig.5.1 b), however this finding is only based on two samples from Cheviot, so should be treated with caution.

- Xenocrystic zircons were identified in all phases of the Carsphairn pluton and two phases of the BSM subvolcanic complex, with corrected ages of ~425 Ma – 1450 Ma (see Sections 4.2.1; 4.2.2). Whilst some zircons are broadly Caledonian in age and might reasonably originate from volcanic detritus eroded into the accretionary prism, zircons with ages from ~880 – 1450 Ma, though very uncommon, require explanation. These ages are identified in the Grampian and Appin Groups of the Dalradian Supergroup of the Grampian Highlands (Cawood et al. 2003), consistent with the provenance of parts of the Southern Uplands Terrane within the Grampian Highlands, based on detrital garnet and muscovite compositions and ages, respectively (Oliver, 2001). Whilst a Laurentian origin for zircon xenocrysts is entirely plausible, it is worth mentioning that, underthrusting of peri-Gondwanan terranes below the Laurentian margin is also a component of tectonic reconstructions (Miles et al. 2014 and refs therein). Miles et al. (2014) reported hafnium (Hf) model ages from zircons of the Criffel and Fleet plutons (~0.9 – 1.0 Ga) which they compared to neodymium (Nd) model ages of Avalonian mantle-derived rocks, such as the Malvern Plutonic complex (~1.2 – 1.0 Ga or ~1.0 – 1.1 Ga). Those authors did acknowledge considerable uncertainties in this comparison. If peri-Gondwanan terranes were involved as a source in the genesis of granitoid magmas, then peri-Gondwanan zircon ages might be expected, as well as Laurentia-derived zircons (Schofield et al. 2016; van Staal et al. 2021; Waldron et al. 2019, 2014, 2008). This study identified a total of 22 xenocrysts across two magmatic suites, however clear attribution to a peri-Gondwanan or Laurentian origin is yet to be determined. Another caveat includes the uncertainty around the exact geological age and composition of the underthrust Ganderian terrane(s) beneath the Southern Uplands. Detrital zircon records from existing exposures in Northern England, Ireland and Canada also contain zircons of similar ages to xenocrystic zircons in this study (Schofield et al. 2016; van Staal et al. 2021; Waldron et al. 2019, 2014, 2008). Hence, whilst the idea of underthrusting is clear in the literature, and indeed supported by geophysical studies of the region (Beamish and Smythe, 1986; Kimbell and Stone, 1995), zircon-based evidence from this thesis do not progress this discussion further.

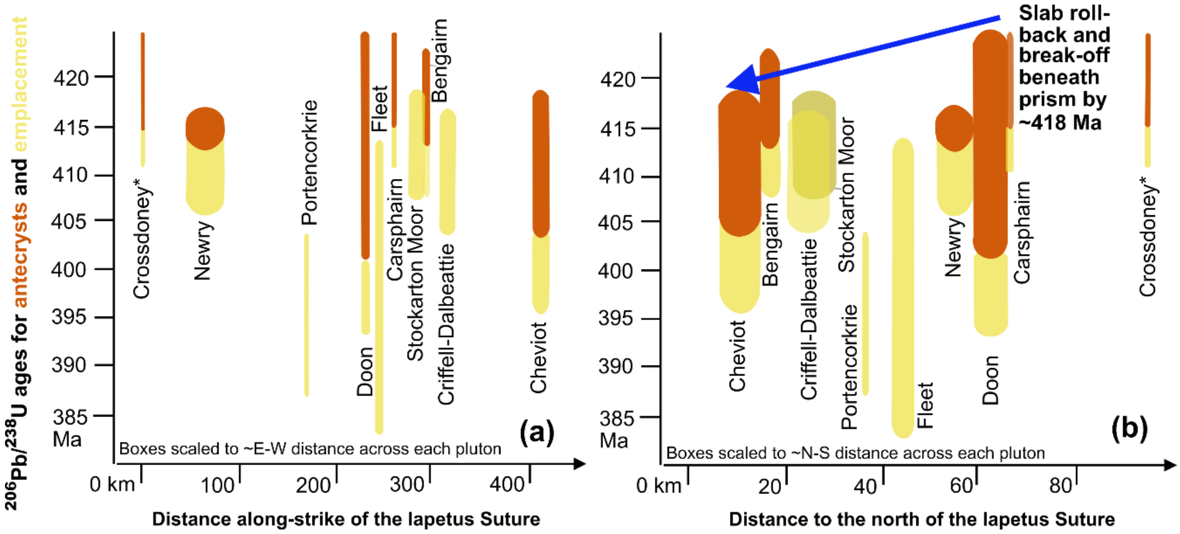

Figure 5.1: Total durations of emplacement magmatism (yellow) and antecrystic growth (orange) determined from U-Pb zircon data from all Southern Uplands-Down Longford terrane granitoids. Age data is plotted against (a) distance from west to east along the Iapetus suture zone and (b) distance to the north of the Iapetus suture. Age data for all bodies are outlined in Table 5.2 below. Reproduced and adapted in Gemmell et al. (2025).

Table 5.2: Total duration of magmatism age data and available source characteristics data from all granitoid bodies across the Southern Uplands-Down-Longford terranes. Data is presented in order of bodies furthest from to bodies closest to the Iapetus suture. Note this table has been adapted for and reproduced in Gemmell et al. (2025).

Complex and its age range from earliest zircon antecrysts to emplacement (Ma)		**Presence of mafic facies**	**U-Pb inheritance (Ma)**	**Available isotope data**	**Comments and references**
Crossdoney	~424 - 410	Not identified	~1900, ~1200, ~480 - ~425	Pb-Pb feldspar, Lu-Hf zircon	Skiba (1952) identified mafic rocks but may be hornfels or restite. Other data from Fritschle (2016).
Carsphairn	~418 – 411	Several samples <60 wt.% SiO_2	~500, ~455-~430	Rb-Sr whole-rock, feldspar, and biotite	Geochronology: this study. Geochemistry: Tindle et al. (1988), Thirlwall (1988).
Doon	~424 – 392	Many samples <60 wt.% SiO_2	~1090, ~500-470	Rb-Sr, Sm-Nd whole-rock	Geochronology: Halliday et al. (1980); Hines et al. (2018). Geochemistry: Brown et al. (1979b); Halliday et al. (1980); Tindle (1982).
Newry	~416 – 406	Average Seeconnell phase <60 wt.% SiO_2	Not evident	No data	Geochronology: Cooper et al. (2016). Geochemistry: Anderson et al. (2016).
Fleet	~414 – 383	Not identified.	Not evident	Lu-Hf-O zircon, Rb-Sr, Sm-Nd whole-rock, Rb-Sr feldspar, muscovite, biotite	Geochronology: Halliday et al. (1980), Miles et al. (2014). Geochemistry: Halliday et al. (1980); Helps (2009); Miles (2013).
Portencorkrie	~403 – 387	Several samples with <60 wt.% SiO_2.	Not evident	No data	Geochronology: Oliver et al. (2008). Geochemistry: Stone, (1995).
Stockarton Moor	~421 – 407	Mafic dykes during Phase 1, no geochemical data.	~900 and ~430	No data	Geochronology: this study. Facies: Leake and Cooper (1983).
Criffell-Dalbeattie	~416 – 402	One sample with <60 wt.% SiO_2. Contains mafic enclaves.	Not evident	Lu-Hf-O zircon, Sm-Nd Rb-Sr whole-rock, Rb-Sr feldspar, biotite	Geochronology: Halliday et al. (1980), Miles et al. (2014). Geochemistry: Halliday et al. (1980); Holden et al. (1987); Helps (2009); Miles (2013).
Bengairn	~415 – 407	One sample with <60 wt.% SiO_2. Contains mafic enclaves.	Not evident	No data	Geochronology: this study. Geochemistry: MacGregor (1937).
Cheviot	~418 – 398	Not identified.	Not evident	Rb-Sr, Sm-Nd whole-rock, Rb-Sr feldspar, clinopyroxene, biotite	Geochronology: this study. Facies: Jhingran (1942). Isotopes: Halliday et al. (1979), Thirlwall (1988).

5.3.2. The onset of collision

This study contributes to the Southern Uplands geodynamic debate, with the new onset of magmatism age data presented and the implications of this data for the position of the Iapetus slab beneath the Laurentian margin. As a reminder from Chapter 2, Section 2.3.2, there are several geodynamic models proposed for magmatism in the Scottish Grampian Highlands, Midland Valley and Southern Uplands (Table 2.2; 2.3). These include relating magmatism to Iapetus subduction (Thirlwall, 1988, 1982, 1981), slab breakoff (Atherton and Ghani, 2002; Miles et al. 2016; Oliver et al. 2008), regional transtension (Brown et al. 2008; Dewey and Strachan, 2003; Hines et al. 2018; Miles et al. 2014), lithospheric delamination (Freeman et al. 1988; O'Reilly et al. 2012) and underthrusting of Peri-Gondwanan terranes (Miles et al. 2014).

It is reasonable to presume that the onset of magmatism should post-date accelerated roll-back of the Iapetus slab (Fig.5.2 a) to allow for magmas to invade the accretionary prism (Baumann et al. 2010; Ding et al. 2017). Therefore, as the earliest recorded onset of magmatism beneath the Southern Uplands-Down-Longford Terrane is ~424 Ma (Table 5.2), collision between Laurentia and peri-Gondwanan terranes was already ongoing prior to ~424 Ma **(**Baumann et al. 2010)**,** allowing a southward shift in magmatism from the Grampian and Midland Valley Terranes to beneath the northern Southern Uplands, beginning with bodies further north of the suture (Fig.5.1 a). This hypothesis is in line with the idea that continental collision initiates accelerated rollback prior to slab breakoff (Baumann et al. 2010; Ding et al. 2017).

Timings of collision of ~428 **-** 423 Ma are proposed in Dewey and Strachan (2003) and Mendum (2012), though they contrast with Hines et al. (2018), see below. The onset of magmatism at ~424 Ma within the accretionary prism recognised in this thesis (Table 5.1), is fairly consistent with Dewey and Strachan's (2003) model.

5.3.3. Slab breakoff and other processes

Previous geodynamic interpretations for Southern Uplands-Down-LongfordTerrane magmatism emphasised slab break-off as the main trigger for magmatism of mantle origin beneath the Grampian Highlands and Southern Uplands (see Chapter 2, Section 2.3.2). Breakoff of the slab into the underlying asthenosphere does occur during continental collision (Aldanmaz et al. 2000; Chemenda et al. 2000; Ding et al. 2017; Keskin, 2003; Lin et al. 2020; Neill et al. 2015; Pearce et al. 1990; Toussaint et al. 2004; von Blanckenburg and Davies, 1995; Williams, 2004), but its timing and significance in the Southern Uplands is unclear. Some argue for very early breakoff of the Iapetus slab beneath Laurentia at ~430 Ma (Hines et al. 2018) which in the context of new ages and the previous discussion, would suggest a post-subduction origin for all magmatism in the Southern Uplands. However, this timing is inconsistent with the time of collision, estimated to be sometime between ~428 – 423 Ma (Dewey and Strachan, 2003; Mendum, 2012) and also contrasts the generally accepted idea that breakoff occurs millions of years after the onset of continental collision (van Hunen and Allen, 2011).

In direct contrast to 'early' breakoff models, the bilateral slab breakoff model of Oliver et al. (2008) argues for very late breakoff, proposing simultaneous breakoff of both Iapetus slabs dipping below terranes north and south of the suture, at ~400 Ma (Table 2.2; 2.3). Very late-stage breakoff at ~400 Ma would imply that any magmatism older than ~400 Ma was produced in a continental arc setting. This model does not seem to be consistent with the fact that pre-400 Ma magmatism took place within the accretionary prism. It therefore does not seem reasonable that continental arc magmatism should migrate into its own accretionary complex without a major geodynamic event such as continental collision having already occurred. The onset of magmatism at Cheviot at ~418 Ma strongly implies that collision pre-dates 418 Ma.

There are also some geochemical considerations to bring to this discussion. If magmatism at Cheviot and in other locations was wholly driven by crustal melting, then arguments regarding the position of the underlying slab and its effect on mantle melting beneath the prism, become open to discussion. However, whole rock elemental and whole rock and mineral-scale isotopic (e.g., Hf, Sr_i, εNd, $\delta^{18}O$, Pb isotopes) data from plutons across the Southern Uplands (see Hines et al. 2018;

Miles et al. 2014 and refs therein) do support the involvement of a mantle component in the genesis of these bodies (Table 5.2).

To get any mantle contribution into the source magmas of Cheviot, the Iapetus slab must have been absent (e.g., via breakoff earlier than ~400 Ma) or at least the lithosphere substantively thinned directly beneath the suture by ~418 Ma (Fig.5.2 b). The end of sedimentation in the accretionary prism at ~420 Ma (Oliver et al. 2008 and refs therein) may also be significant as a marker of uplift associated with collision and breakoff (Fig.5.2 b). Therefore, although an exact timing for roll-back cannot be determined, it is likely, based on the onset of magmatism beneath Carsphairn at ~424 Ma, that rollback initiated sometime before ~424 Ma (Fig.5.2 a). Whilst an exact timing for breakoff also cannot be constrained, the end of sedimentation and uplift at ~420 Ma and the onset of magmatism at Cheviot at ~418 Ma implies breakoff occurred at approximately ~420 Ma (Fig.5.2 b). If collision occurred sometime between ~428 – 423 Ma (Dewey and Strachan, 2003; Mendum, 2012), then this timing of rollback and slab break off shortly after collision seems sensible (Fig.5.2 a, b).

The other factor in driving magmatism that is widely referenced is a regional switch in tectonics from transpression (i.e., compressional) tectonics to transtension (i.e., extensional) across the British Caledonides (Brown et al. 2008; Dewey and Strachan, 2003; Soper and Woodcock, 2003) estimated to be at around ~415 Ma (Brown et al. 2008; Hines et al. 2018; Strachan et al. 2020). Again, this switch may be an effective marker for the timing of slab breakoff. Although, it is unclear what triggered regional transtension. Most of the Southern Uplands and Down-Longford complexes were emplaced after this switch (Table 2.1; 5.1) At the mid- to upper crustal levels, the onset of transtension is likely to have triggered rejuvenation and ascent of lower crustal hot zone magmas (Fig. 5.2 b) (Brown et al. 2008; Richards, 2022)**.** The lack of spatio-temporal patterns in ages interpreted as representing appropriate timings for emplacement (Fig. 5.1) does imply that such a switch triggered emplacement events local to major structures rather than magmatism being related to some deeper, regionally diachronous mechanism such as slab tearing.

5.3.4. Continental underthrusting

To reiterate, continental underthrusting and associated melting are also considered an important component of the collision story (Miles et al. 2014 and refs therein, Stone et al. 2012). Underthrusting would have removed the mantle wedge over time and prevented the fresh input of mafic magmas into the lower crust (Magni et al. 2017). The time by which the underthrust peri-Gondwanan material plausibly reached beneath the melting zone would have to be some time after ~418 Ma, to enable the involvement of a mantle-derived component in the source of the Cheviot complex (Fig.5.2 c).

Broadly, older bodies across the Southern Uplands (e.g., Carsphairn, Doon) contain greater proportions of mafic facies and therefore more direct evidence of contemporary mafic magmatism compared to younger plutons farther south (e.g., Cheviot, Fleet) which, based on available geochemical and isotopic data, are more enriched in crustal components (Table 5.2). The data supporting lower and upper crustal involvement in Southern Upland petrogenesis is extensive and extends to whole rock and mineral-scale Pb-Pb, Lu-Hf, Rb-Sr and Sm-Nd and stable O analysis (Halliday et al. 1985, 1980; Stephens and Halliday, 1984).

5.3.5. The overall timeline

This study has contributed new data to the Southern Uplands magmatism debate, including dating the timing of the onset of magmatism beneath the accretionary prism and updating ages interpreted to represent an appropriate time of emplacement for several intrusions across the Southern Uplands of Scotland (Table 5.1). In contrast to numerous previous studies which argue for a dominantly slab breakoff trigger for magmatism (Atherton and Ghani, 2002; Neilson et al. 2009; Oliver et al. 2008), this study considers slab rollback to be a major factor in the onset of magmatism, based on the above discussion. The model presented in Figure 5.2 visualises the possible geodynamic and tectonic processes discussed but not yet agreeably constrained in the literature (Table 2.2; 2.3).

To reiterate, Figure 5.2a highlights the onset of collision between peri-Gondwanan terranes and Laurentia (Mendum, 2012) and the onset of slab rollback prior to ~424 Ma. Slab rollback in turn allows for mantle wedge melting beneath the accretionary prism and crystallisation of the earliest cores (and occasionally rims) interpreted as antecrystic within the lower crust from ~424 Ma onwards (e.g., Carsphairn pluton; Fig.5.2 a). The continued attachment and drag effect of the Iapetus slab might plausibly explain continued accretionary prism sedimentation until ~420 Ma (see Bottrill et al. 2012 for an example from Iran). From this point, sedimentation in the prism ceases, magmatism occurs for the first time beneath Cheviot directly above the suture at ~418 Ma (Fig.5.2 b), and a switch to regional transtension occurs at ~415 Ma (Brown et al. 2008; Hines et al. 2018; Strachan et al. 2020). These points suggest that slab breakoff occurred at approximately ~420 Ma (Fig.5.2 b). Widespread magmatic emplacement events were concurrent with breakoff and the onset of regional transtension (Fig.5.2 b), and these continued, with increasingly felsic and crust-dominated compositions, plausibly alongside continental underthrusting, until after 400 Ma (Fig.5.2 c). Although, it is unclear if transtension drove magmatic emplacement or If emplacement triggered regional transtension. A switch from compressional tectonics to transtension would favour decompression, thus magma ascent through crustal pathways from lower crustal hot zones (Richards, 2022). This switch to transtension, the release of hot zone magmas (Fig.5.2 b, c) and the limited addition of fresh mafic magma, allowed for emplacement magmatism to occur from ~415 Ma onwards.

One final point is that mantle melting in modern collision zones is sometimes attributed to edge-driven convection caused by lithospheric thickness contrasts (e.g., Kaislaniemi and van Hunen, 2014; Missenard and Cadoux, 2012) and by different scales of delamination of subduction-modified weak lithospheric mantle (Kaislaniemi et al. 2014; Pearce et al. 1990). There might indeed be a lithospheric thickness contrast between thinner, subduction modified Laurentian lithospheric mantle and older, colder and therefore thicker peri-Gondwanan lithospheric mantle underthrusting the Laurentian margin (Fig.5.2 c). Therefore, it is possible that mantle convection processes contribute to prolonged magmatism following collision and slab breakoff, particularly further north in the Grampian Highlands (e.g., dates in Oliver et al. 2008).

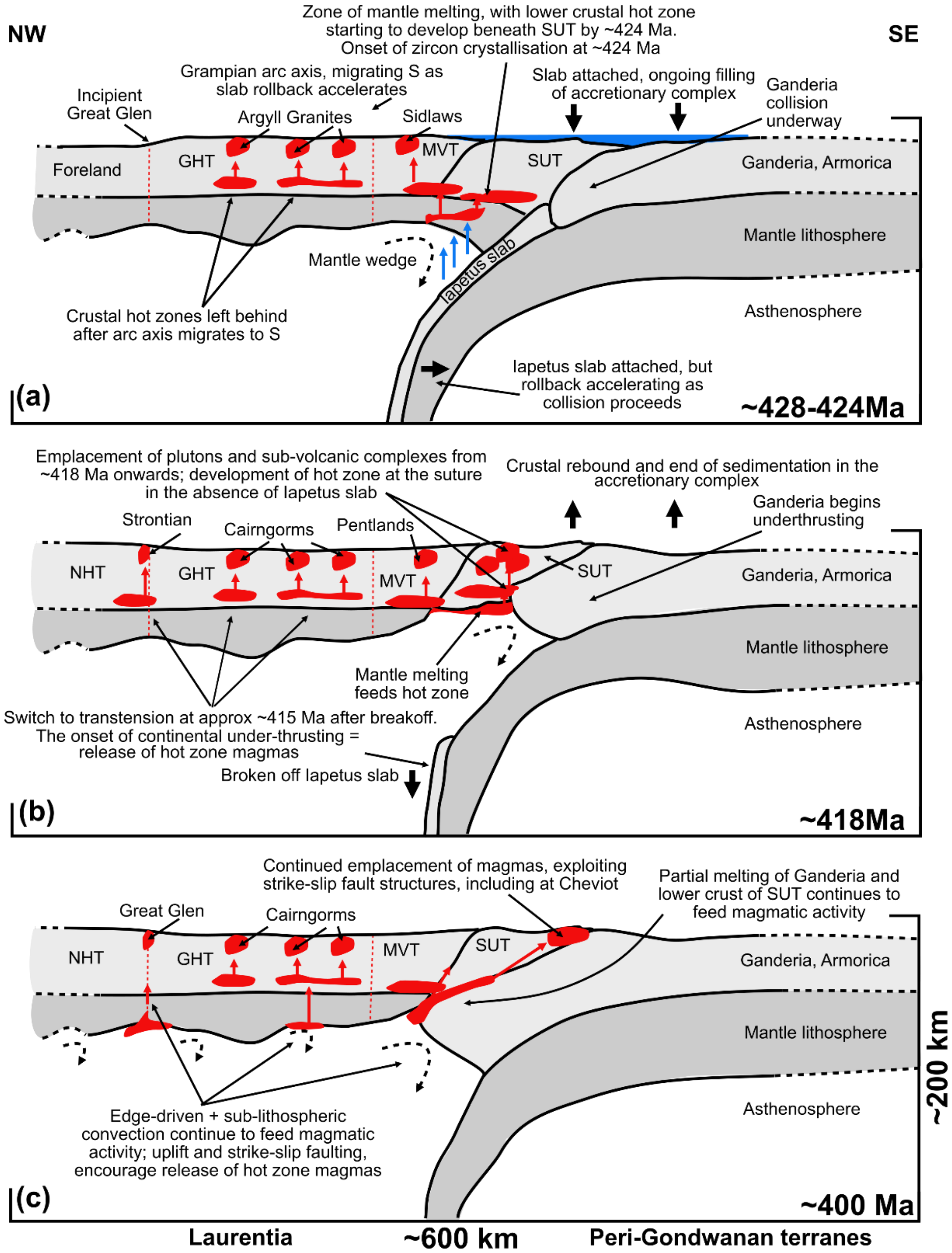

Figure 5.2: A geodynamic reconstruction from NW to SE across the Grampian Highlands Terrane (GHT), Midland Valley Terrane (MVT) and the Southern Uplands Terrane (SUT) adapted from the geodynamic interpretations of Miles et al. (2014) and Baumann et al. (2010). (a) Collision between the Laurentian continental margin and peri-Gondwanan terranes occurring between ~428 – 424 Ma (Dewey and Strachan, 2003; Mendum, 2012). Roll-back of the Iapetus oceanic slab as collision continues. Dewatering of the down-going slab (blue arrows), mantle wedge melting and onset of lower crustal hot zone development beneath the SUT prism. (b) Break-off of the Iapetus slab at ~420 Ma allows for mantle melting directly below the Iapetus suture and triggers continued hot zone development, the onset of underthrusting of peri-Gondwanan continental lithosphere, uplift and the end of sedimentation within the accretionary prism. A subsequent regional switch to transtension at ~415 Ma facilitated release of hot zone magmas and emplacement though localised structures. (c) Continued underthrusting, associated crustal melting, re-mobilisation of lower crustal hot zone magmas and further emplacement of the youngest bodies (e.g., Cheviot). Mantle melting north of the SUT accretionary prism possibly driven by edge-driven convection. NHT = Northern Highlands Terrane. Reproduced and adapted in Gemmell et al. (2025).

6. Conclusions and Future Work

6.1. Conclusions

1) Cores and rims interpreted as plausibly representing antecrystic zircon growth are recognised from the appearance of cores or rims with magmatic zoning, chemically fairly similar to younger rims, but with U-Pb laser ablation ages outwith the confidence interval of calculated ages interpreted as representing appropriate times of emplacement. Cores and rims interpreted as antecrystic are present in most facies of the Carsphairn, Bengairn and Cheviot plutons alongside the Black Stockarton Moor subvolcanic complex**.** The oldest antecryst as determined from cores and thus, the earliest onset of magmatism identified at each study area is: ~424 Ma in Carsphairn, ~423 Ma in Bengairn, ~423 Ma in Black Stockarton Moor and ~418 Ma in Cheviot**.**

2) A total of ten facies were analysed over the Carsphairn, Bengairn and Cheviot plutons and the Black Stockarton Moor subvolcanic complex. It was possible to calculate zircon crystallisation ages interpreted as representing an appropriate time of emplacement for seven of these**.** Emplacement occurred no earlier than ~415 Ma at any location**.**

3) A few xenocrystic zircons were identified in this study. The majority were Caledonian in age, confirming the general observation that xenocrysts are not common in the Southern Upland magmatic suites (Miles et al. 2014). A few xenocrysts were Proterozoic in age but were of uncertain provenance and could reasonably be of either Laurentian or peri-Gondwanan origin.

4) The preservation of zircons recording prolonged histories supports the long-term storage and evolution of magmas beneath the Southern Uplands accretionary prism, whilst also acknowledging a considerable body of work that points towards mantle melting being an integral component of Southern Uplands magmatism.

5) This study proposes that breakoff of the Iapetus slab occurred at approximately ~420 Ma, concurrent with the end of sedimentation in the prism (*c.* 420 Ma, Oliver et al. 2008) and thus, a period of uplift. The earliest onset of magmatism beneath Carsphairn is recognised from the onset of zircon growth at ~424 Ma and implies that Iapetus slab rollback must have occurred prior to this time to enable mantle melting beneath the site of emplacement (Fig.5.2 a). In contrast to existing models proposing slab breakoff as the dominant trigger for magmatism, this study proposes that prior slab rollback makes more sense in terms of the overall timing of hot zone development in the prism. The onset of magmatism directly above the Solway Line, or Iapetus Suture at Cheviot at ~418 Ma is probably the most direct magmatic evidence for slab breakoff at ~420 Ma, as magmatism on the suture would be highly unlikely by ~418 Ma if the slab were still attached to the lithosphere here. Widespread emplacement events across the Southern Uplands started at ~415 Ma and are contemporaneous with a regional switch to transtension (~415 Ma; Fig.5.2 b**;** Strachan et al. 2020). Continental underthrusting of peri-Gondwanan lithosphere is potentially an important factor of the new model proposed in this study. Underthrusting must have been significant only after ~418 Ma to allow for mantle melt involvement in the genesis of Cheviot. The co-incidence of extensive underthrusting with the onset of regional transtension at ~415 Ma may be significant. Whilst extensional tectonics facilitated remobilisation of lower crustal magmas (Fig.5.2 b), underthrusting would have prevented input of fresh mantle-derived magmas into the lower crust (Fig.5.2 c). Following underthrusting, magmatism was potentially driven by melting of the accretionary prism or peri-Gondwanan lithosphere, as evidenced by younger plutons having more felsic compositions. Further north into the Midland Valley and Grampian Highlands, the effect of deep lithospheric underthrusting has not been explored, but there is potential for development of a lithospheric thickness contrast, aiding edge-driven convection and/or lithospheric delamination processes which might sustain magmatism to ~400 Ma in these regions (Fig.5.2 c).

6.2. Future work

Whilst the data in this thesis contribute to our understanding of magmatism on the Laurentian margin and its geodynamic triggers, much of the work focuses on the extent to which the ages themselves are reliable. Greater confidence in the accuracy of these crystallisation ages interpreted as best representing the time of emplacement, and improvement in data point precision, would in turn provide sharper resolution for geodynamic models, and allow for deeper levels of investigation, such as the identification of the timescales of pluton growth and the ability to statistically distinguish between facies.

The dataset analysed in this study could be improved by considering the following recommendations:

- Individual data point precision could be improved from the lower precision ~1-2 % errors per spot produced by in-situ LA-ICP-MS analysis in this study. This improvement could be achieved by switching from a single-collector ICP-MS to a multi-collector ICP-MS which has higher sensitivity. Alternatively, ion probe methods (e.g., Miles et al. 2014) would allow for more specific targeting of smaller areas on the zircon grains, avoiding ambiguity over which growth layer was analysed, or enabling some smaller rims to be analysed. These methods without pre-treatment of zircon grains for Pb loss or rigorous corrections for common Pb will always involve some measure of uncertainty that could be averted with the use of chemical abrasion pre-treatment of zircons prior to LA-ICP-MS or ion probe analyses (Widmann et al. 2019; Yang et al. 2024). Future studies may also consider thermal annealing pre-treatment of zircons to improve the MSWD (i.e., data dispersion) and overall age accuracy (Solari et al. 2015; Yang et al. 2024). As noted by Milne et al. (2023), the prior application of LA-ICP-MS studies can be used to inform which specific polished zircons would be ideal candidates for chemical abrasion isotope dilution thermal ionisation mass spectrometry (CA-ID-TIMS)work. Cheviot is a good candidate for such analysis, due to the high yield of zircons of closely overlapping ages. However, ID-TIMS analysis may not be appropriate for several other samples where single zircon ages were less reliable and less clustered (e.g., SM01). CA-ID-TIMS is expensive but has the potential to provide ~0.1% precision on individual data points, allowing for the possibility of statistically distinguishing crystallisation and emplacement timescales. Alternatively, if CA-ID-TIMS data were available prior to laser ablation, then it would provide greater certainty as to whether LA-ICP-MS results had been affected by Pb loss, allowing for better interpretation of the lower precision distinction between zones of zircons interpreted as emplacement-related vs zircon cores and occasionally rims interpreted as antecrysts. Further analysis of zircon trace element geochemistry in all samples is strongly recommended to enable chemical distinction between zircon rims (i.e., interpreted as emplacement growth) vs cores (i.e., interpreted as antecrysts) and, more broadly, to allow for interpretation of the chemical evolution of magmas.

- Age controlled Hf and stable O isotope analysis of zircons using ion probe or isotope dilution techniques could also be applied to each pluton and complex to better constrain crustal interaction in the magmas over time.

- Further extensive sampling of each pluton and complex is recommended to try and obtain higher yields of zircon. Further sampling of the different phases at Black Stockarton Moor is encouraged, especially of larger bodies, to determine if they contain a higher yield of zircon. An attempt might also be made to obtain alternative dateable mineral phases such as apatite or titanite from each pluton and complex.

This study has recognised other future lines of work at a more regional scale of the British and Irish Caledonides. Firstly, it is strongly recommended that the workflow followed in this study, be more widely used as a starting point prior to CA-ID-TIMS analysis. Application to other areas in Scotland such as the Grampian Highlands is recommended, particularly as this terrane’s geochronology record relies heavily on a single study and generally only one sample per plutonic complex (Oliver et al. 2008). There is definitely an opportunity to better constrain the total duration of magmatism, from its onset to final emplacement events, and to track the spatial-temporal progression of magmatism and its relationship to Caledonian geodynamics over a wider sector of the orogen. Work following a similar approach is already well underway in the Northern Highlands Terrane (Milne et al. 2023; MacRae et al. 2023 *in* prep; MacRae, 2024, submitted, MacRae, Neill et al. in prep, Neill, Strachan, Roberts, new funded LA-ICP-MS and CA-ID-TIMS work started in 2024). Further research should also assess the potential for critical metal enrichment at bodies and complexes where this was previously recognised (e.g., Black Stockarton Moor; Brown et al. 1979b, Cheviot; Cameron et al. 1988) in addition to identifying the relationship between pluton history, chemical evolution, and metallogenesis. At a critical time of energy transition, it is key to note that several plutonic facies exhibit high radiogenic heat production, including the Doon, Fleet, Criffel and Cheviot plutonic complexes (McCay and Younger, 2017). It is worth exploring and identifying the temporal and chemical evolution characteristics of these bodies that enabled them to become high heat producing compared to other intrusions of a similar age.

Appendices

Appendix A – Hand specimen and thin section images

(1) Hand specimen photographs (where taken)

Cairnsmore of Carsphairn

CR-05

CR-06

CR-07

CR-08

Bengairn pluton

BG-01

Mafic enclave

(2) Thin section images in plain polarised light (LHS) and cross polarised light (RHS)

Cairnsmore of Carsphairn

See Table 4.1 for a detailed description of the petrography of all Carsphairn samples.

CR-05 (Alkali feldspar dominated granite)

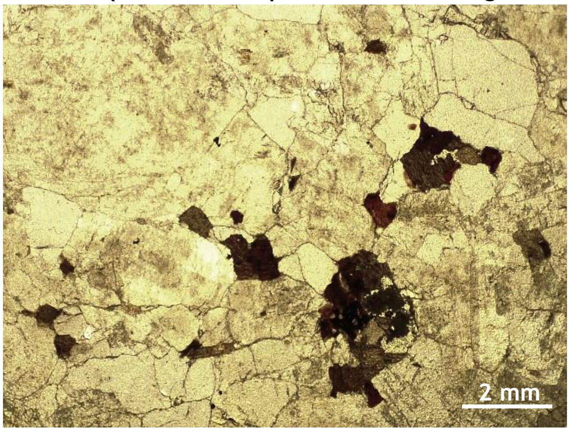

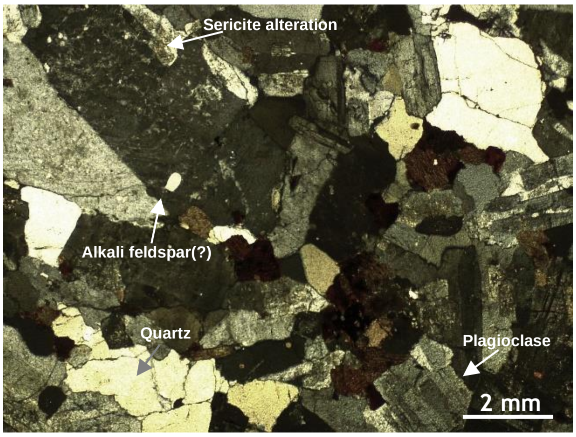

CR-06 (Plagioclase and quartz dominated granodiorite)

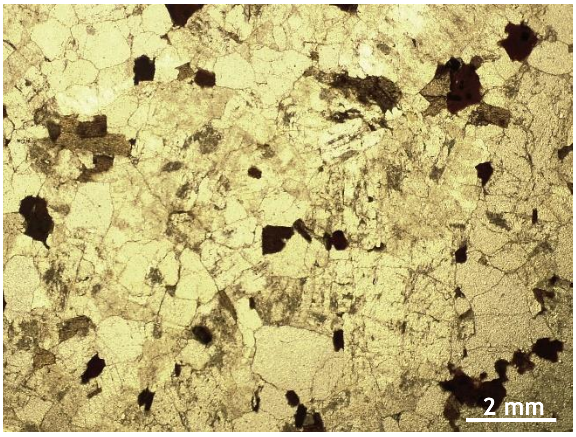

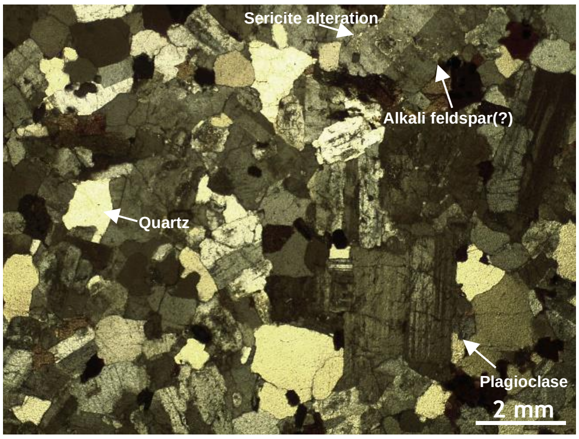

CR-07 (Plagioclase dominated granodiorite)

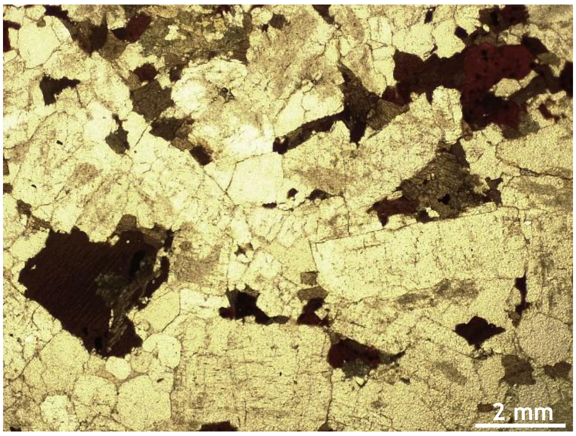

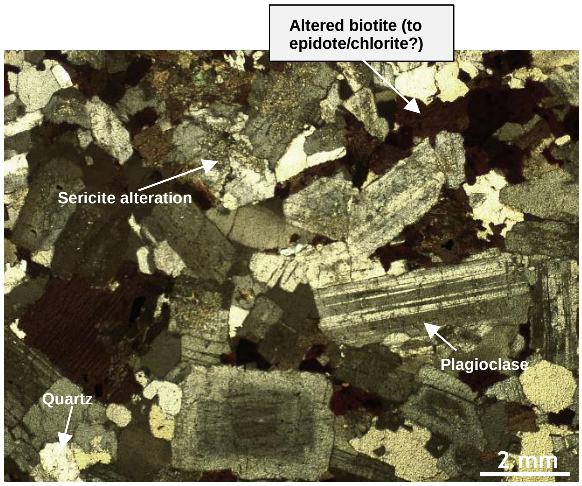

CR-08 (Plagioclase dominated monzogranite)

Primary Mineralogy

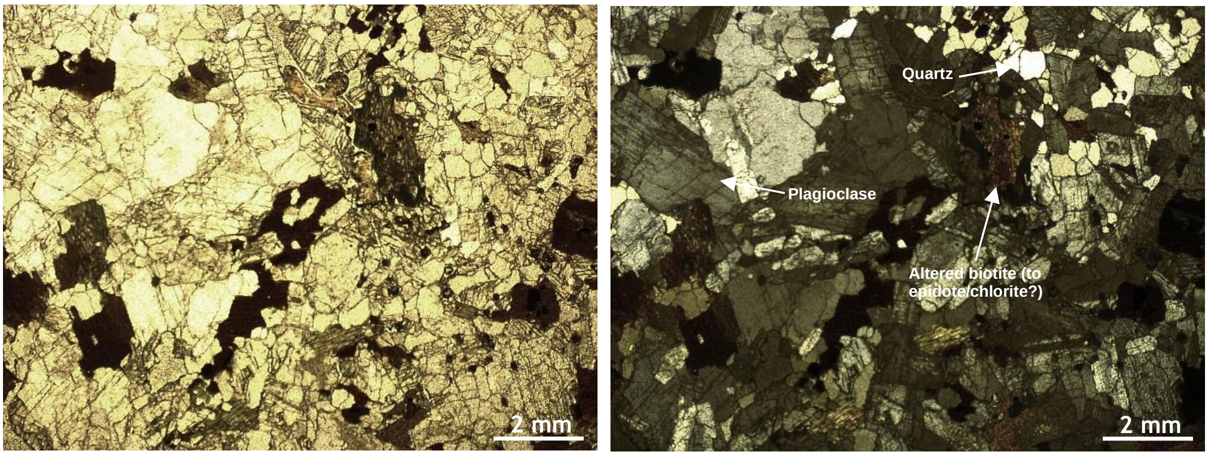

Alteration mineralogy

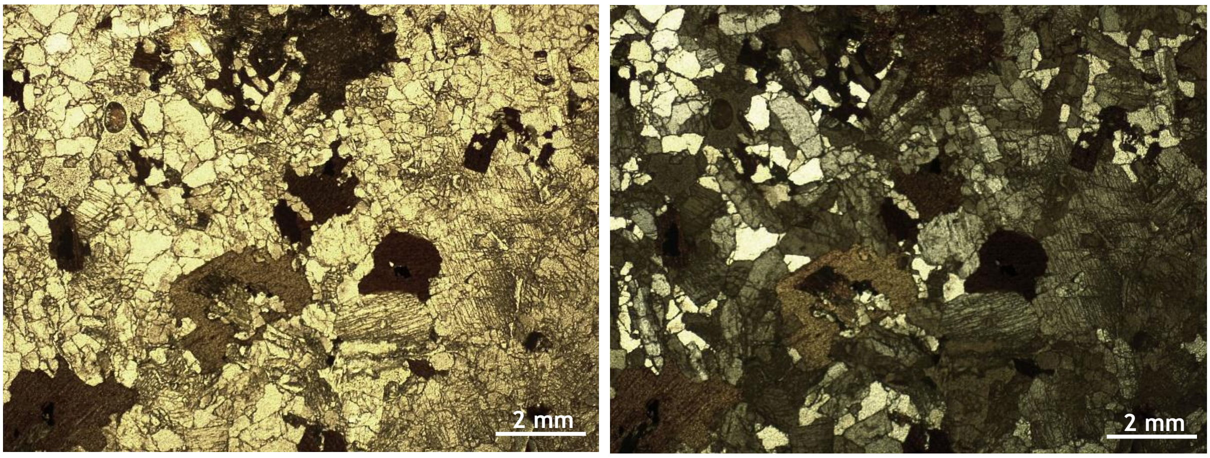

Black Stockarton Moor Subvolcanic Complex

See Table 4.1 for a detailed description of the petrography of all Black Stockarton Moor samples.

JD-01 (Plagioclase dominated quartz diorite)

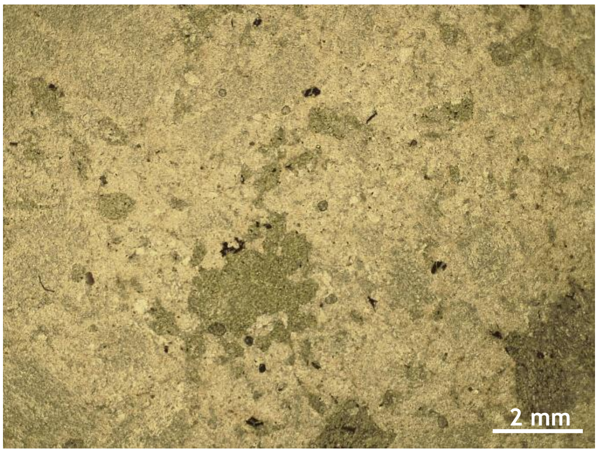

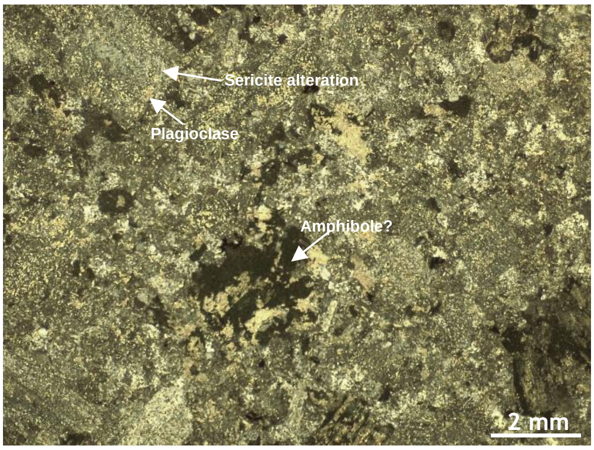

SM-02 (Plagioclase dominated quartz diorite)

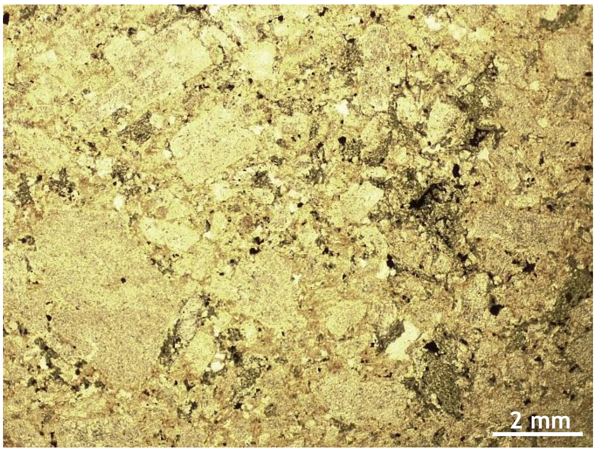

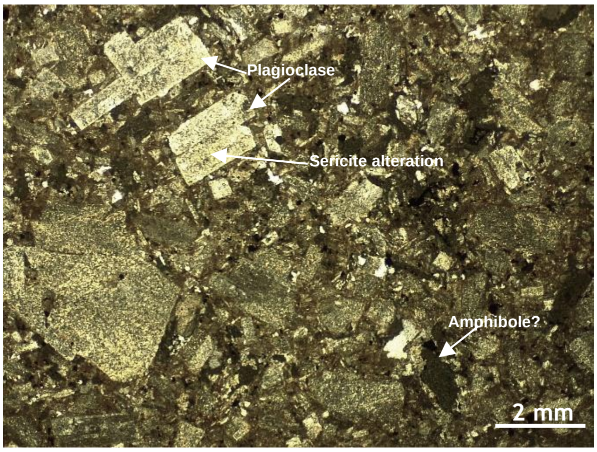

SM-01 (Plagioclase dominated quartz diorite)

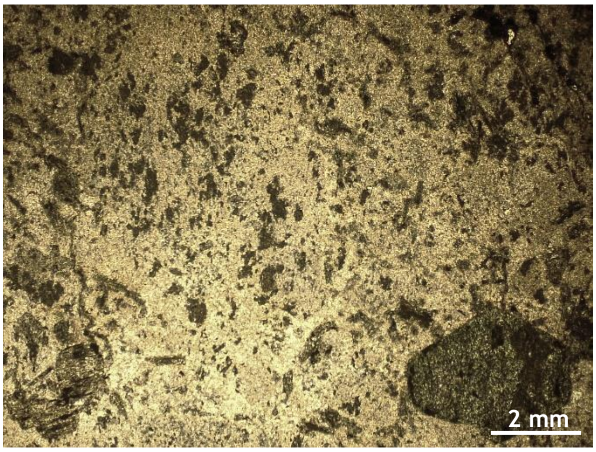

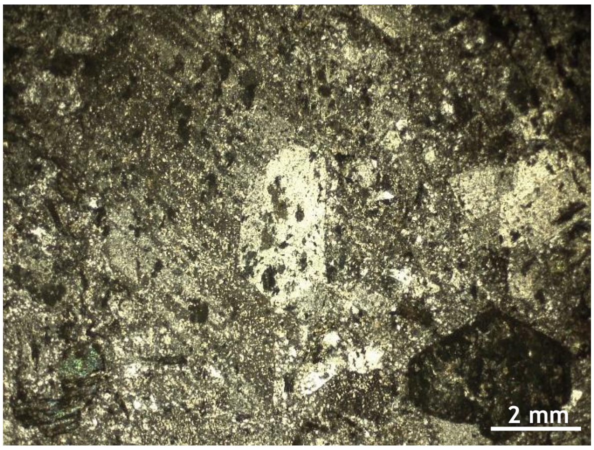

Bengairn pluton

See Table 4.1 for a detailed description of the petrography of all Bengairn samples.

BG-01 (Plagioclase dominated quartz monzodiorite)

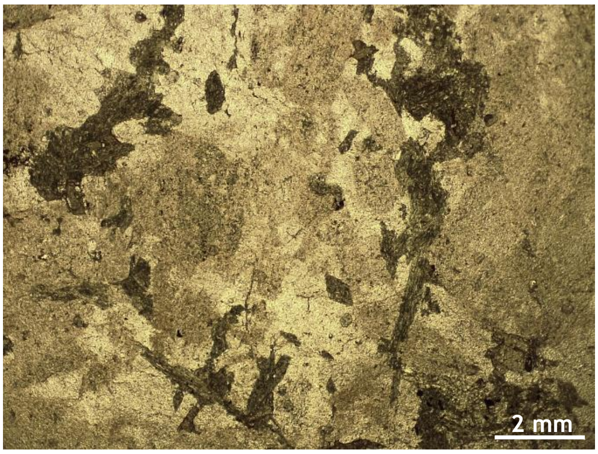

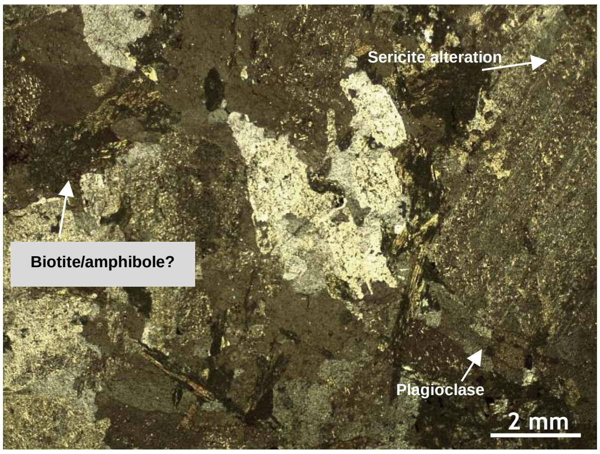

Cheviot pluton

CH-01 (Alkali feldspar dominated quartz monzonite)

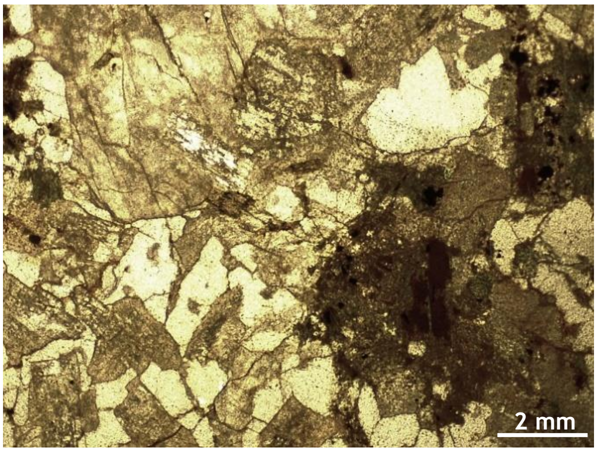

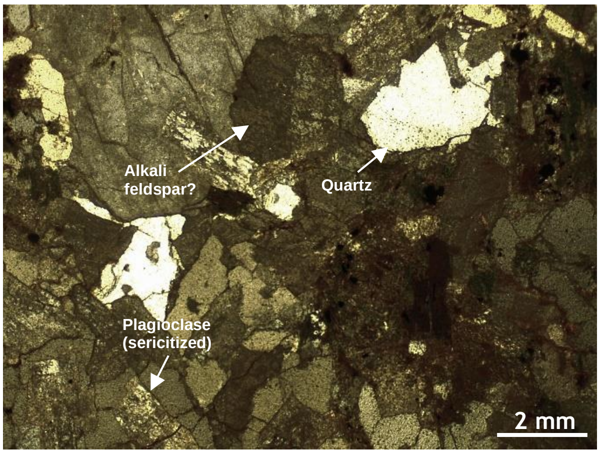

Possible tourmaline (bottom right, high order interference colours in XPL)

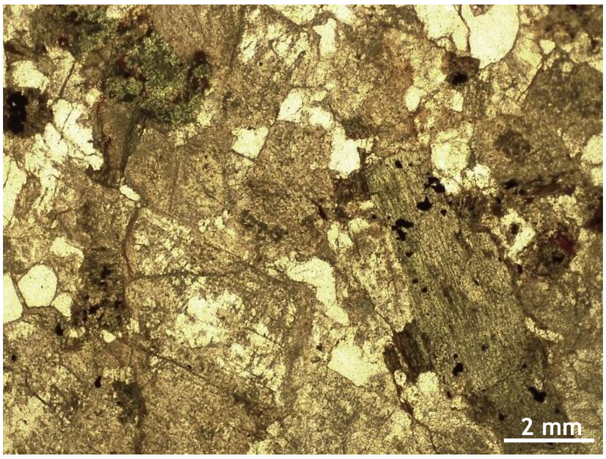

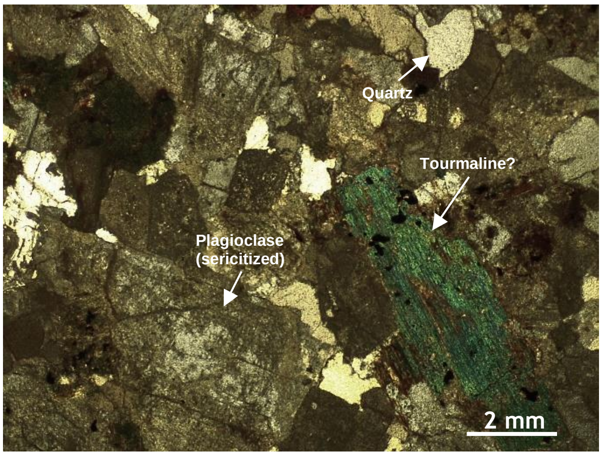

CH-02 (Alkali feldspar dominated syenogranite)

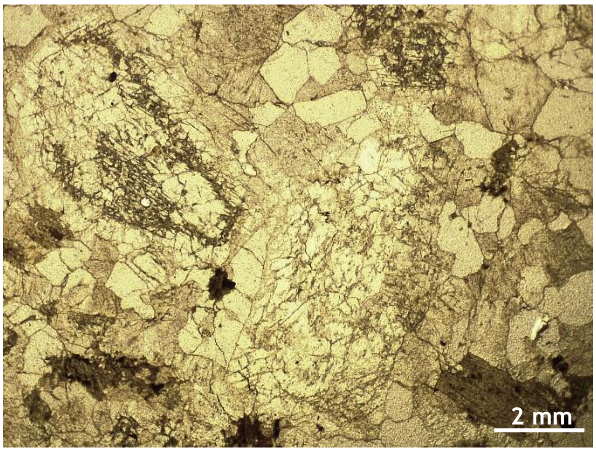

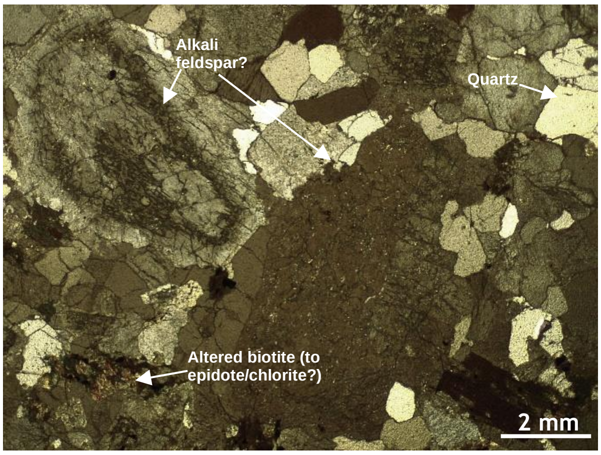

Appendix B – Cathodoluminescence images

Appendix B includes scanning electron microscope (SEM) – cathodoluminescence (CL) images for all zircons yielded from each sample. Each sample has an individual pdf file containing all SEM-CL images of yielded zircons. Spots analysed for U-Pb and trace element analysis by LA-ICP-MS are also annotated, and colour coded for emplacement, antecrystic, xenocrystic, probable Pb loss and for rejected spots. Files can be accessed from the Appendices zip folder found here: https://doi.org/10.5525/gla.researchdata.1780

Appendix C – Zircon textural tables

Appendix C includes textural descriptions for all zircons (both analysed and not analysed) yielded from all samples. It contains 10 tables, one per sample. Tables include the Zircon ID which correspond to spot numbers annotated in the pdf file for each sample in Appendix B. The table also describes other textural characteristics, including grain shape, zoning pattern, and other features such as fracturing, alteration, inclusions and recrystallisation occurrences. Appendix C can be accessed from the Appendices zip folder found here:
https://doi.org/10.5525/gla.researchdata.1780

Appendix D – Zircon U-Pb data

Appendix D includes one excel file containing all the U-Pb LA-ICP-MS zircon geochronology data after Iolite (v.4) processing for each sample. Metadata and the data reduction scheme settings are included in this file. Appendix D can be found in the Appendices zip folder found here:
https://doi.org/10.5525/gla.researchdata.1780

Appendix E – Zircon trace element data

Appendix E includes one excel file containing all the LA-ICP-MS zircon trace element data after Iolite (v.4) processing for each sample. Appendix E can be found in the Appendices zip folder found here:
https://doi.org/10.5525/gla.researchdata.1780

Appendix F – Th/U ratios

Three Th/U vs $^{206}Pb/^{238}U$ spot age plots provided for all samples analysed from the Carsphairn pluton **(Figure 1),** the Black Stockarton Moor subvolcanic complex **(Figure 2)** and the Cheviot pluton **(Figure 3).**

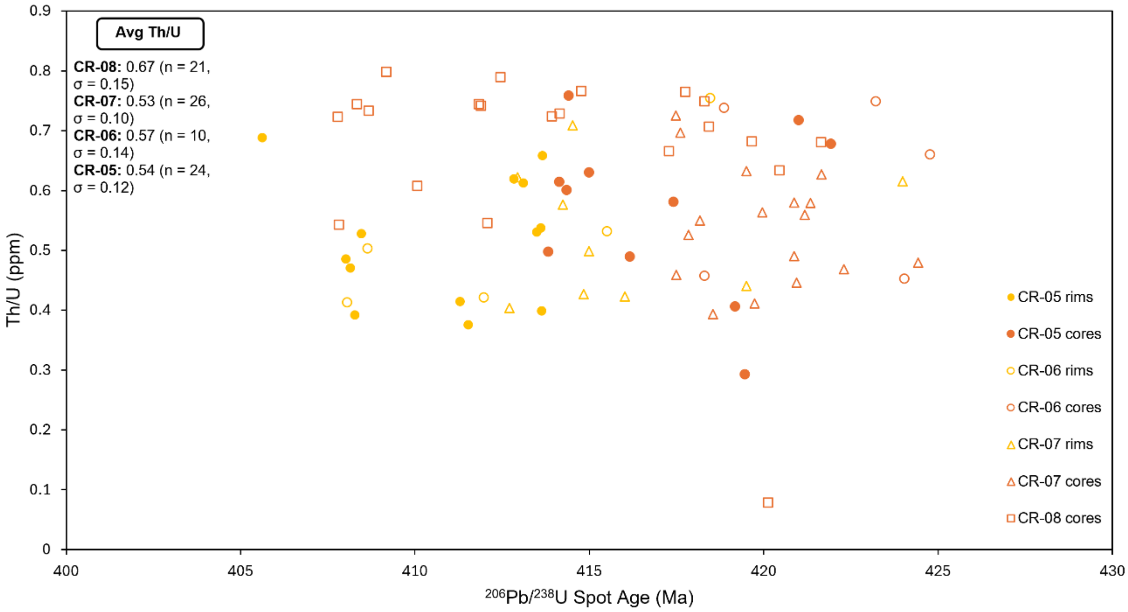

Figure 1: Th/U vs $^{206}Pb/^{238}U$ spot age plot for all acceptable rims (yellow) and cores (orange) in all Carsphairn samples. Cores falling within and younger than the confidence interval of the weighted mean ages interpreted to represent an appropriate time of emplacement for CR-08, 07, 06 and 05 (see section 4.2.1) are not shown due to the suspicion that these are probable Pb loss cores. Cores and rims shown correlate to the $^{206}Pb/^{238}U$ weighted mean plot for each sample (see Figure 4.1 g; 4.2 g; 4.3 g; 4.4 g). The average Th/U ratio value and its associated standard deviation (σ) is provided for each sample.

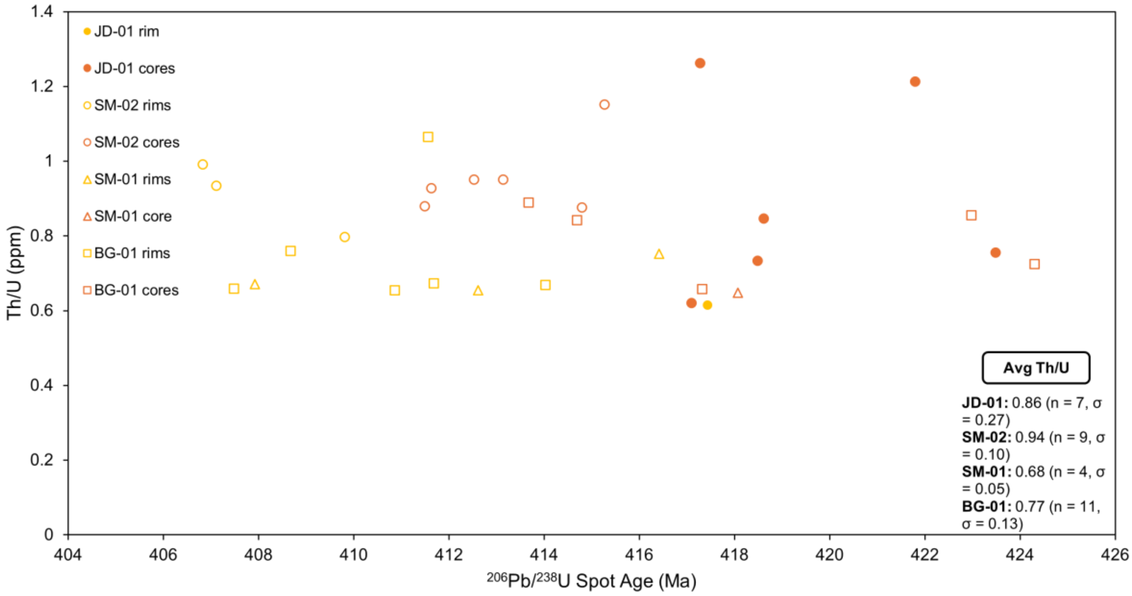

Figure 2: Th/U vs $^{206}Pb/^{238}U$ spot age plot for all acceptable rims (yellow) and cores (orange) in all Black Stockarton Moor samples. Cores falling within and younger than the confidence interval of the weighted mean emplacement ages for JD-01, SM-02, BG-01 and SM-01 (see section 4.2.2) are not shown on the suspicion that these are probable Pb loss cores. Cores and rims shown correlate to the $^{206}Pb/^{238}U$ weighted mean plot for each sample (see Figure 4.5 j; 4.6 g; 4.7 g; 4.8 e). The average Th/U ratio value and its associated standard deviation (σ) is provided for each sample.

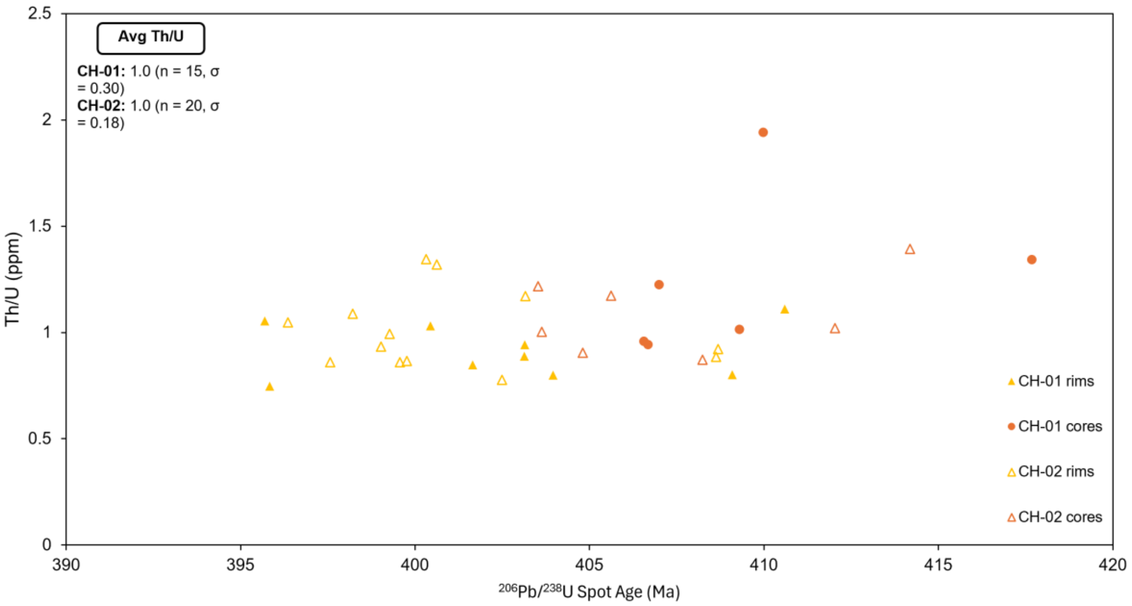

Figure 3: Th/U vs $^{206}Pb/^{238}U$ spot age plot for all acceptable rims (yellow) and cores (orange) in both Cheviot samples. Cores falling within and younger than the confidence interval of the weighted mean emplacement ages for CH-01 and CH-02 (see section 4.2.3) are not shown on the suspicion that these are probable Pb loss cores. Cores and rims shown correlate to the $^{206}Pb/^{238}U$ weighted mean plot for each sample (see Figure 4.9 g; 4.10 g). The average Th/U ratio value and its associated standard deviation (σ) is provided for each sample.

Reference List

Aldanmaz, E., Pearce, J.A., Thirlwall, M.F., Mitchell, J.G., 2000. Petrogenetic evolution of late Cenozoic, post-collision volcanism in western Anatolia, Turkey. Journal of Volcanology and Geothermal Research 102, 67–95. https://doi.org/10.1016/S0377-0273(00)00182-7

Al-Hafdh, N.M.S., 1985. The alteration petrology of the Cheviot granite (Thesis). Newcastle University.

Al-Lazki, A.I., Seber, D., Sandvol, E., Turkelli, N., Mohamad, R., Barazangi, M., 2003. Tomographic Pn velocity and anisotropy structure beneath the Anatolian plateau (eastern Turkey) and the surrounding regions. Geophysical Research Letters 30. https://doi.org/10.1029/2003GL017391

Allen, C.M., Campbell, I.H., 2012. Identification and elimination of a matrix-induced systematic error in LA–ICP–MS 206Pb/238U dating of zircon. Chemical Geology 332–333, 157–165. https://doi.org/10.1016/j.chemgeo.2012.09.038

Altunkaynak, Ş., 2007. Collision-Driven Slab Breakoff Magmatism in Northwestern Anatolia, Turkey. The Journal of Geology 115, 63–82. https://doi.org/10.1086/509268

Andersen, T., 2002. Correction of common lead in U–Pb analyses that do not report 204Pb. Chemical Geology 192, 59–79. https://doi.org/10.1016/S0009-2541(02)00195-X

Annen, C., Blundy, J.D., Sparks, R.S.J., 2006. The Genesis of Intermediate and Silicic Magmas in Deep Crustal Hot Zones. Journal of Petrology 47, 505–539. https://doi.org/10.1093/petrology/egi084

Archibald, D.B., Macquarrie, L.M.G., Murphy, J.B., Strachan, R.A., McFarlane, C.R.M., Button, M., Larson, K.P., Dunlop, J., 2021. The construction of the Donegal composite batholith, Irish Caledonides: Temporal constraints from U-Pb dating of zircon and titanite. GSA Bulletin 133, 2335–2354. https://doi.org/10.1130/B35856.1

Archibald, D.B., Murphy, J.B., 2021. A slab failure origin for the Donegal composite batholith, Ireland as indicated by trace-element geochemistry. SP 503, 347–370. https://doi.org/10.1144/SP503-2020-6

Archibald, D.B., Murphy, J.B., Fowler, M., Strachan, R.A., Hildebrand, R.S., 2022. Testing petrogenetic models for contemporaneous mafic and felsic to intermediate magmatism within the “Newer Granite” suite of the Scottish and Irish Caledonides, in: Kuiper, Y.D., Murphy, J.B., Nance, R.D., Strachan, R.A., Thompson, M.D. (Eds.), New Developments in the Appalachian-Caledonian-Variscan Orogen. Geological Society of America, pp. 375–399. https://doi.org/10.1130/2021.2554(15)

Atherton, M.P., Ghani, A.A., 2002. Slab breakoff: a model for Caledonian, Late Granite syn-collisional magmatism in the orthotectonic (metamorphic) zone of Scotland and Donegal, Ireland. Lithos 62, 65–85. https://doi.org/10.1016/S0024-4937(02)00111-1

Baumann, C., Gerya, T.V., Connolly, J.A.D., 2010. Numerical modelling of spontaneous slab breakoff dynamics during continental collision. SP 332, 99–114. https://doi.org/10.1144/SP332.7

Beamish, D., Smythe, D.K., 1986. Geophysical images of the deep crust: the Iapetus suture. Journal of the Geological Society 143, 489–497. https://doi.org/10.1144/gsjgs.143.3.0489

Belousova, E., Griffin, W., O’Reilly, S.Y., Fisher, N., 2002. Igneous zircon: trace element composition as an indicator of source rock type. Contrib Mineral Petrol 143, 602–622. https://doi.org/10.1007/s00410-002-0364-7

Bird, A.F., Thirlwall, M.F., Strachan, R.A., Manning, C.J., 2013. Lu–Hf and Sm–Nd dating of metamorphic garnet: evidence for multiple accretion events during the Caledonian orogeny in Scotland. Journal of the Geological Society 170, 301–317. https://doi.org/10.1144/jgs2012-083

Bird, P., 1978. Initiation of intracontinental subduction in the Himalaya. Journal of Geophysical Research: Solid Earth 83, 4975–4987. https://doi.org/10.1029/JB083iB10p04975

Black, L.P., Kamo, S.L., Allen, C.M., Davis, D.W., Aleinikoff, J.N., Valley, J.W., Mundil, R., Campbell, I.H., Korsch, R.J., Williams, I.S., Foudoulis, C., 2004. Improved 206Pb/238U microprobe geochronology by the monitoring of a trace-element-related matrix effect; SHRIMP, ID–TIMS, ELA–ICP–MS and oxygen isotope documentation for a series of zircon standards. Chemical Geology 205, 115–140. https://doi.org/10.1016/j.chemgeo.2004.01.003

Bottrill, A.D., van Hunen, J., Allen, M.B., 2012. Insight into collision zone dynamics from topography: numerical modelling results and observations. Solid Earth 3, 387–399. https://doi.org/10.5194/se-3-387-2012

Brown, G.C., Cassidy, J., Tindle, A.G., Hughes, D.J., 1979. The Loch Doon granite: an example of granite petrogenesis in the British Caledonides. JGS 136, 745–753. https://doi.org/10.1144/gsjgs.136.6.0745

Brown, M.J., Leake, R.C., Parker, M.E., Fortey, N.J., 1979. Porphyry style copper mineralisation at Black Stockarton Moor, south-west Scotland (Mineral Reconnaissance Programme Report No. 30). Institute of Geological Sciences.

Brown, P.E., Ryan, P.D., Soper, N.J., Woodcock, N.H., 2008. The Newer Granite problem revisited: a transtensional origin for the Early Devonian Trans-Suture Suite. Geological Magazine 145, 235–256. https://doi.org/10.1017/S0016756807004219

Burnham, A.D., 2020. Key concepts in interpreting the concentrations of the rare earth elements in zircon. Chemical Geology 551, 119765. https://doi.org/10.1016/j.chemgeo.2020.119765

Cameron, D.G., Cooper, D.C., Bide, P.J., Allen, P.M., Haslam, H.W., 1988. A geochemical survey of part of the Cheviot Hills and investigations of drainage anomalies in the Kingsseat area [WWW Document]. URL https://nora.nerc.ac.uk/id/eprint/11837/ (accessed 10.12.23).

Cashman, K.V., Sparks, R.S.J., Blundy, J.D., 2017. Vertically extensive and unstable magmatic systems: A unified view of igneous processes. Science 355, eaag3055. https://doi.org/10.1126/science.aag3055

Cawood, P.A., Nemchin, A.A., Smith, M., Loewy, S., 2003. Source of the Dalradian Supergroup constrained by U–Pb dating of detrital zircon and implications for the East Laurentian margin. JGS 160, 231–246. https://doi.org/10.1144/0016-764902-039

Chapman, J.B., Shields, J.E., Ducea, M.N., Paterson, S.R., Attia, S., Ardill, K.E., 2021. The causes of continental arc flare ups and drivers of episodic magmatic activity in Cordilleran orogenic systems. Lithos 398–399, 106307. https://doi.org/10.1016/j.lithos.2021.106307

Chappell, B.W., White, A.J.R., 2001. Two contrasting granite types: 25 years later. Australian Journal of Earth Sciences 48, 489–499. https://doi.org/10.1046/j.1440-0952.2001.00882.x

Charlier, B.L.A., Wilson, C.J.N., Lowenstern, J.B., Blake, S., Van Calsteren, P.W., Davidson, J.P., 2005. Magma Generation at a Large, Hyperactive Silicic Volcano (Taupo, New Zealand) Revealed by U–Th and U–Pb Systematics in Zircons. Journal of Petrology 46, 3–32. https://doi.org/10.1093/petrology/egh060

Chaussard, E., Amelung, F., 2014. Regional controls on magma ascent and storage in volcanic arcs. Geochemistry, Geophysics, Geosystems 15, 1407–1418. https://doi.org/10.1002/2013GC005216
Chemenda, A.I., Burg, J.-P., Mattauer, M., 2000. Evolutionary model of the Himalaya–Tibet system: geopoembased on new modelling, geological and geophysical data. Earth and Planetary Science Letters 174, 397–409. https://doi.org/10.1016/S0012-821X(99)00277-0
Chew, D.M., Strachan, R.A., 2014. The Laurentian Caledonides of Scotland and Ireland. SP 390, 45–91. https://doi.org/10.1144/SP390.16
Chiaradia, M., 2022. Distinct magma evolution processes control the formation of porphyry Cu–Au deposits in thin and thick arcs. Earth and Planetary Science Letters 599, 117864. https://doi.org/10.1016/j.epsl.2022.117864
Chiaradia, M., 2014. Copper enrichment in arc magmas controlled by overriding plate thickness. Nature Geosci 7, 43–46. https://doi.org/10.1038/ngeo2028
Chiaradia, M., Caricchi, L., 2017. Stochastic modelling of deep magmatic controls on porphyry copper deposit endowment. Sci Rep 7, 44523. https://doi.org/10.1038/srep44523
Clemens, J.D., Darbyshire, D.P.F., Flinders, J., 2009. Sources of post-orogenic calcalkaline magmas: The Arrochar and Garabal Hill–Glen Fyne complexes, Scotland. Lithos, The genesis and significance of adakitic, high-Mg andesites, and other refractory magmas in intra-oceanic forearc settings 112, 524–542. https://doi.org/10.1016/j.lithos.2009.03.026
Collins, W.J., Murphy, J.B., Johnson, T.E., Huang, H.-Q., 2020. Critical role of water in the formation of continental crust. Nat. Geosci. 13, 331–338. https://doi.org/10.1038/s41561-020-0573-6
Crisp, L.J., Berry, A.J., Burnham, A.D., Miller, L.A., Newville, M., 2023. The Ti-in-zircon thermometer revised: The effect of pressure on the Ti site in zircon. Geochimica et Cosmochimica Acta 360, 241–258. https://doi.org/10.1016/j.gca.2023.04.031
Davies, J., Von Blanckenburg, F., 1995. Slab breakoff: A model of lithosphere detachment and its test in the magmatism and deformation of collisional orogens. Earth and Planetary Science Letters 129, 85–102. https://doi.org/10.1016/0012-821X(94)00237-S
Deer, W.A., 1935. The Cairnsmore of Carsphairn Igneous Complex. Quarterly Journal of the Geological Society of London 91, 47–76. https://doi.org/10.1144/GSL.JGS.1935.091.01-04.03
Dewey, J., Mange, M., 1999. Petrography of Ordovician and Silurian sediments in the western Irish Caledonides: tracers of a short-lived Ordovician continent-arc collision orogeny and the evolution of the Laurentian Appalachian-Caledonian margin. Geological Society, London, Special Publications 164, 55–107. https://doi.org/10.1144/GSL.SP.1999.164.01.05
Dewey, J.F., Dalziel, I.W.D., Reavy, R.J., Strachan, R.A., 2015. The Neoproterozoic to Mid-Devonian evolution of Scotland: a review and unresolved issues. SJG 51, 5–30. https://doi.org/10.1144/sjg2014-007
Dewey, J.F., Ryan, P.D., 2016. Connemara: its position and role in the Grampian Orogeny. Can. J. Earth Sci. 53, 1246–1257. https://doi.org/10.1139/cjes-2015-0125
Dewey, J.F., Strachan, R.A., 2003. Changing Silurian–Devonian relative plate motion in the Caledonides: sinistral transpression to sinistral transtension. Journal of the Geological Society 160, 219–229. https://doi.org/10.1144/0016-764902-085
Dilek, Y., Altunkaynak, Ş., 2009. Geochemical and temporal evolution of Cenozoic magmatism in western Turkey: mantle response to collision, slab break-off,

and lithospheric tearing in an orogenic belt. Geological Society, London, Special Publications 311, 213–233. https://doi.org/10.1144/SP311.8
Ding, L., Maksatbek, S., Cai, F., Wang, H., Song, P., Ji, W., Xu, Q., Zhang, L., Muhammad, Q., Upendra, B., 2017. Processes of initial collision and suturing between India and Asia. Sci. China Earth Sci. 60, 635–651. https://doi.org/10.1007/s11430-016-5244-x
Ducea, M.N., Paterson, S.R., DeCelles, P.G., 2015. High-Volume Magmatic Events in Subduction Systems. Elements 11, 99–104. https://doi.org/10.2113/gselements.11.2.99
Ekici, T., 2016. Collision-related slab break-off volcanism in the Eastern Anatolia, Kepez volcanic complex (TURKEY). Geodinamica Acta 28, 223–239. https://doi.org/10.1080/09853111.2015.1121796
Ersoy, E.Y., Palmer, M.R., Genç, Ş.C., Prelević, D., Akal, C., Uysal, İ., 2017. Chemo-probe into the mantle origin of the NW Anatolia Eocene to Miocene volcanic rocks: Implications for the role of, crustal accretion, subduction, slab roll-back and slab break-off processes in genesis of post-collisional magmatism. Lithos 288–289, 55–71. https://doi.org/10.1016/j.lithos.2017.07.006
Faithfull, J.W., Dempster, T.J., MacDonald, J.M., Reilly, M., EIMF, 2018. Metasomatism and the crystallization of zircon megacrysts in Archaean peridotites from the Lewisian complex, NW Scotland. Contrib Mineral Petrol 173, 99. https://doi.org/10.1007/s00410-018-1527-5
Flinders, A.F., Shen, Y., 2017. Seismic evidence for a possible deep crustal hot zone beneath Southwest Washington. Sci Rep 7, 7400. https://doi.org/10.1038/s41598-017-07123-w
Fowler, M.B., Kocks, H., Darbyshire, D.P.F., Greenwood, P.B., 2008. Petrogenesis of high Ba–Sr plutons from the Northern Highlands Terrane of the British Caledonian Province. Lithos 105, 129–148. https://doi.org/10.1016/j.lithos.2008.03.003
Freeburn, R., Bouilhol, P., Maunder, B., Magni, V., Van Hunen, J., 2017. Numerical models of the magmatic processes induced by slab breakoff. Earth and Planetary Science Letters 478, 203–213. https://doi.org/10.1016/j.epsl.2017.09.008
Freeman, B., Klemperer, S.L., Hobbs, R.W., 1988. The deep structure of northern England and the Iapetus Suture zone from BIRPS deep seismic reflection profiles. JGS 145, 727–740. https://doi.org/10.1144/gsjgs.145.5.0727
Fu, B., Page, F.Z., Cavosie, A.J., Fournelle, J., Kita, N.T., Lackey, J.S., Wilde, S.A., Valley, J.W., 2008. Ti-in-zircon thermometry: applications and limitations. Contrib Mineral Petrol 156, 197–215. https://doi.org/10.1007/s00410-008-0281-5
Garzanti, E., Radeff, G., Malusà, M.G., 2018. Slab breakoff: A critical appraisal of a geological theory as applied in space and time. Earth-Science Reviews 177, 303–319. https://doi.org/10.1016/j.earscirev.2017.11.012
Halliday, A.N., 1984. Coupled Sm–Nd and U–Pb systematics in late Caledonian granites and the basement under northern Britain. Nature 307, 229–233. https://doi.org/10.1038/307229a0
Halliday, A.N., Aftalion, M., van Breemen, O., Jocelyn, J., 1979. Petrogenetic significance of Rb-Sr and U-Pb isotopic systems in the 400 Ma old British Isles granitoids and their hosts. Geological Society, London, Special Publications 8, 653–661. https://doi.org/10.1144/GSL.SP.1979.008.01.79
Halliday, A.N., Stephens, W.E., Harmon, R.S., 1980. Rb-Sr and O isotopic relationships in 3 zoned Caledonian granitic plutons, Southern Uplands, Scotland: evidence for varied sources and hybridization of magmas. Journal

of the Geological Society 137, 329–348. https://doi.org/10.1144/gsjgs.137.3.0329
Halliday, A.N., Stephens, W.E., Hunter, R.H., Menzies, M.A., Dickin, A.P., Hamilton, P.J., 1985. Isotopic and chemical constraints on the building of the deep Scottish lithosphere. Scottish Journal of Geology 21, 465–491. https://doi.org/10.1144/sjg21040465
Hildreth, W., Moorbath, S., 1988. Crustal contributions to arc magmatism in the Andes of Central Chile. Contr. Mineral. and Petrol. 98, 455–489. https://doi.org/10.1007/BF00372365
Hines, R., Paterson, S.R., Memeti, V., Chambers, J.A., 2018. Nested Incremental Growth of Zoned Upper Crustal Plutons in the Southern Uplands Terrane, UK: Fractionating, Mixing, and Contaminated Magma Fingers. Journal of Petrology 59, 483–516. https://doi.org/10.1093/petrology/egy034
Jackson, M.D., Blundy, J., Sparks, R.S.J., 2018. Chemical differentiation, cold storage and remobilization of magma in the Earth’s crust. Nature 564, 405–409. https://doi.org/10.1038/s41586-018-0746-2
Jhingran, A.G., Tomkeieff, S.I., 1942. The Cheviot Granite. Quarterly Journal of the Geological Society of London 98, 241–259. https://doi.org/10.1144/GSL.JGS.1942.098.01-04.14
Jones, K., Blake, S., 2003. Mountain Building in Scotland. Open University Worldwide.
Kaislaniemi, L., van Hunen, J., 2014. Dynamics of lithospheric thinning and mantle melting by edge-driven convection: Application to Moroccan Atlas mountains. Geochemistry, Geophysics, Geosystems 15, 3175–3189. https://doi.org/10.1002/2014GC005414
Kaislaniemi, L., van Hunen, J., Allen, M.B., Neill, I., 2014. Sublithospheric small-scale convection—A mechanism for collision zone magmatism. Geology 42, 291–294. https://doi.org/10.1130/G35193.1
Keskin, M., 2003. Magma generation by slab steepening and breakoff beneath a subduction-accretion complex: An alternative model for collision-related volcanism in Eastern Anatolia, Turkey. Geophysical Research Letters 30. https://doi.org/10.1029/2003GL018019
Keskin, M., Pearce, J.A., Mitchell, J.G., 1998. Volcano-stratigraphy and geochemistry of collision-related volcanism on the Erzurum–Kars Plateau, northeastern Turkey. Journal of Volcanology and Geothermal Research 85, 355–404. https://doi.org/10.1016/S0377-0273(98)00063-8
Kimbell, G.S., Stone, P., 1995. Crustal magnetization variations across the Iapetus Suture Zone. Geological Magazine 132, 599–609. https://doi.org/10.1017/S0016756800021257
Klaver, M., Blundy, J.D., Vroon, P.Z., 2018. Generation of arc rhyodacites through cumulate-melt reactions in a deep crustal hot zone: Evidence from Nisyros volcano. Earth and Planetary Science Letters 497, 169–180. https://doi.org/10.1016/j.epsl.2018.06.019
Kröner, A., Wan, Y., Liu, X., Liu, D., 2014. Dating of zircon from high-grade rocks: Which is the most reliable method? Geoscience Frontiers 5, 515–523. https://doi.org/10.1016/j.gsf.2014.03.012
Lawrence, A., Fowler, M., Kingsbury, C.G., Knott, T., Mark, D., Stevenson, C.T.E., 2023. Slab-failure or Slab-success? Examining the contributions of crust and mantle to post-subduction magmatism in the Ratagain Complex, NW Scotland. Lithos 448–449, 107139. https://doi.org/10.1016/j.lithos.2023.107139
Leake, R.C., Cooper, C., 1983. The Black Stockarton Moor subvolcanic complex, Galloway. JGS 140, 665–676. https://doi.org/10.1144/gsjgs.140.4.0665

Lee, M.K., 1982. Regional geophysics of the Cheviot area. United Kingdom.
Leggett, J.K., McKerrow, W.S., Casey, D.M., 1982. The anatomy of a Lower Palaeozoic accretionary forearc: the Southern Uplands of Scotland. Geological Society, London, Special Publications 10, 495–520. https://doi.org/10.1144/GSL.SP.1982.010.01.33
Leggett, J.K., McKerrow, W.S., Eales, M.H., 1979. The Southern Uplands of Scotland: A Lower Palaeozoic accretionary prism. JGS 136, 755–770. https://doi.org/10.1144/gsjgs.136.6.0755
Leggett, J.K., McKerrow, W.S., Soper, N.J., 1983. A model for the crustal evolution of southern Scotland. Tectonics 2, 187–210. https://doi.org/10.1029/TC002i002p00187
Li, S., Chung, S.-L., Wilde, S.A., Wang, T., Xiao, W.-J., Guo, Q.-Q., 2016. Linking magmatism with collision in an accretionary orogen. Sci Rep 6, 25751. https://doi.org/10.1038/srep25751
Lin, C.-M., Tseng, T.-L., Meliksetian, K., Karakhanyan, A., Huang, B.-S., Babayan, H., Hu, J.-C., Gevorgyan, M., Chang, S.-F., Levonyan, A., 2020. Locally Thin Crust and High Crustal VP/VS Ratio Beneath the Armenian Volcanic Highland of the Lesser Caucasus: A Case for Recent Delamination. Journal of Geophysical Research: Solid Earth 125, e2019JB019151. https://doi.org/10.1029/2019JB019151
Loader, M.A., Nathwani, C.L., Wilkinson, J.J., Armstrong, R.N., 2022. Controls on the magnitude of Ce anomalies in zircon. Geochimica et Cosmochimica Acta 328, 242–257. https://doi.org/10.1016/j.gca.2022.03.024
Macdonald, R., Fettes, D.J., 2006. The tectonomagmatic evolution of Scotland.
Magni, V., Allen, M.B., van Hunen, J., Bouilhol, P., 2017. Continental underplating after slab break-off. Earth and Planetary Science Letters 474, 59–67. https://doi.org/10.1016/j.epsl.2017.06.017
Maury, R., Fourcade, S., Coulon, C., El Azzouzi, M., Bellon, H., Coutelle, A., Ouabadi, A., Semroud, B., Megartsi, M., Cotten, J., Belanteur, O., Louni-Hacini, A., Piqué, A., Capdevila, R., Hernandez, J., Réhault, J.-P., 2000. Post-collisional Neogene magmatism : a consequence of slab breakoff. C. R. Acad. Sci. Paris. Earth Planet. Sci. 331, 159–173.
McCay, A.T., Younger, P.L., 2017. Ranking the geothermal potential of radiothermal granites in Scotland: are any others as hot as the Cairngorms? Scottish Journal of Geology 53, 1–11. https://doi.org/10.1144/sjg2016-008
McDonough, W.F., Sun, S. -s., 1995. The composition of the Earth. Chemical Geology, Chemical Evolution of the Mantle 120, 223–253. https://doi.org/10.1016/0009-2541(94)00140-4
McKerrow, W.S., 1987. The Southern Uplands Controversy. JGS 144, 735–736. https://doi.org/10.1144/gsjgs.144.5.0735
Mckerrow, W.S., Leggett, J.K., Eales, M.H., 1977. Imbricate thrust model of the Southern Uplands of Scotland. Nature 267, 237–239. https://doi.org/10.1038/267237a0
McKerrow, W.S., Mac Niocaill, C., Dewey, J.F., 2000. The Caledonian Orogeny redefined. JGS 157, 1149–1154. https://doi.org/10.1144/jgs.157.6.1149
Mendum, J.R., 2012. Late Caledonian (Scandian) and Proto-Variscan (Acadian) orogenic events in Scotland. Journal of the Open University Geological Society 33, 37–51.
Miles, A., Graham, C., Hawkesworth, C., Gillespie, M., Dhuime, B., Hinton, R., 2014. Using Zircon Isotope Compositions to Constrain Crustal Structure and Pluton Evolution: the Iapetus Suture Zone Granites in Northern Britain. Journal of Petrology 55, 181–207. https://doi.org/10.1093/petrology/egt065

Miles, A.J., 2013. Genesis of zoned granite plutons in the Iapetus Suture Zone: new constraints from high-precision micro-analysis of accessory minerals.

Miles, A.J., Graham, C.M., Hawkesworth, C.J., Gillespie, M.R., Hinton, R.W., Edinburgh Ion Microprobe Facility (EIMF), 2013. Evidence for distinct stages of magma history recorded by the compositions of accessory apatite and zircon. Contrib Mineral Petrol 166, 1–19. https://doi.org/10.1007/s00410-013-0862-9

Miles, A. J., Woodcock, N.H., 2018. A combined geochronological approach to investigating long lived granite magmatism, the Shap granite, UK. Lithos 304–307, 245–257. https://doi.org/10.1016/j.lithos.2018.02.012

Miles, A.J., Woodcock, N.H., 2018. A combined geochronological approach to investigating long lived granite magmatism, the Shap granite, UK. Lithos 304–307, 245–257. https://doi.org/10.1016/j.lithos.2018.02.012

Miles, A.J., Woodcock, N.H., Hawkesworth, C.J., 2016. Tectonic controls on post-subduction granite genesis and emplacement: The late Caledonian suite of Britain and Ireland. Gondwana Research 39, 250–260. https://doi.org/10.1016/j.gr.2016.02.006

Miller, C.F., McDowell, S.M., Mapes, R.W., 2003. Hot and cold granites? Implications of zircon saturation temperatures and preservation of inheritance. Geol 31, 529. https://doi.org/10.1130/0091-7613(2003)031<0529:HACGIO>2.0.CO;2

Miller, J.S., Matzel, J.E.P., Miller, C.F., Burgess, S.D., Miller, R.B., 2007. Zircon growth and recycling during the assembly of large, composite arc plutons. Journal of Volcanology and Geothermal Research, Large Silicic Magma Systems 167, 282–299. https://doi.org/10.1016/j.jvolgeores.2007.04.019

Milne, E.J.M., Neill, I., Bird, A.F., Millar, I.L., McDonald, I., Dempsey, E.D., Olive, V., Odling, N., Waters, E.C., 2023. Caledonian hot zone magmatism in the ‘Newer Granites’: insight from the Cluanie and Clunes plutons, Northern Scottish Highlands. JGS 180, jgs2022-076. https://doi.org/10.1144/jgs2022-076

Missenard, Y., Cadoux, A., 2012. Can Moroccan Atlas lithospheric thinning and volcanism be induced by Edge-Driven Convection? Terra Nova 24, 27–33. https://doi.org/10.1111/j.1365-3121.2011.01033.x

Nebel, O., 2013. Rb–Sr Dating, in: Rink, W.J., Thompson, J. (Eds.), Encyclopedia of Scientific Dating Methods. Springer Netherlands, Dordrecht, pp. 1–19. https://doi.org/10.1007/978-94-007-6326-5_116-1

Neill, I., Meliksetian, K., Allen, M.B., Navasardyan, G., Kuiper, K., 2015. Petrogenesis of mafic collision zone magmatism: The Armenian sector of the Turkish–Iranian Plateau. Chemical Geology 403, 24–41. https://doi.org/10.1016/j.chemgeo.2015.03.013

Neilson, J.C., Kokelaar, B.P., Crowley, Q.G., 2009. Timing, relations and cause of plutonic and volcanic activity of the Siluro-Devonian post-collision magmatic episode in the Grampian Terrane, Scotland. Journal of the Geological Society 166, 545–561. https://doi.org/10.1144/0016-76492008-069

Oliver, G., Wilde, S., Wan, Y., 2008. Geochronology and geodynamics of Scottish granitoids from the late Neoproterozoic break-up of Rodinia to Palaeozoic collision. Journal of The Geological Society - J GEOL SOC 165, 661–674. https://doi.org/10.1144/0016-76492007-105

Oliver, G.J.H., 2001. Reconstruction of the Grampian episode in Scotland: its place in the Caledonian Orogeny. Tectonophysics 332, 23–49. https://doi.org/10.1016/S0040-1951(00)00248-1

O’Reilly, B.M., Hauser, F., Readman, P.W., 2012. The fine-scale seismic structure of the upper lithosphere within accreted Caledonian lithosphere:

implications for the origins of the ‘Newer Granites.’ Journal of the Geological Society 169, 561–573. https://doi.org/10.1144/0016-76492011-128
Paterson, S.R., Ducea, M.N., 2015. Arc Magmatic Tempos: Gathering the Evidence. Elements 11, 91–98. https://doi.org/10.2113/gselements.11.2.91
Paton, C., Hellstrom, J., Paul, B., Woodhead, J., Hergt, J., 2011. Iolite: Freeware for the visualisation and processing of mass spectrometric data. J. Anal. At. Spectrom. 26, 2508–2518. https://doi.org/10.1039/C1JA10172B
Paul, B., Petrus, J., Savard, D., Woodhead, J., Hergt, J., Greig, A., Paton, C., Rayner, P., 2023. Time resolved trace element calibration strategies for LA-ICP-MS. Journal of Analytical Atomic Spectrometry 38, 1995–2006. https://doi.org/10.1039/D3JA00037K
Pearce, J.A., Bender, J.F., De Long, S.E., Kidd, W.S.F., Low, P.J., Güner, Y., Saroglu, F., Yilmaz, Y., Moorbath, S., Mitchell, J.G., 1990. Genesis of collision volcanism in Eastern Anatolia, Turkey. Journal of Volcanology and Geothermal Research 44, 189–229. https://doi.org/10.1016/0377-0273(90)90018-B
Petford, N., Gallagher, K., 2001. Partial melting of mafic (amphibolitic) lower crust by periodic influx of basaltic magma. Earth and Planetary Science Letters 193, 483–499. https://doi.org/10.1016/S0012-821X(01)00481-2
Pichavant, M., Villaros, A., Michaud, J.A.-S., Scaillet, B., 2024. Granite magmatism and mantle filiation. European Journal of Mineralogy 36, 225–246. https://doi.org/10.5194/ejm-36-225-2024
Rabayrol, F., Hart, C.J.R., Thorkelson, D.J., 2019. Temporal, spatial and geochemical evolution of late Cenozoic post-subduction magmatism in central and eastern Anatolia, Turkey. Lithos 336–337, 67–96. https://doi.org/10.1016/j.lithos.2019.03.022
Read, H.H., 1961. Aspects of Caledonian magmatism in Britain. Geological Journal 2, 653–683. https://doi.org/10.1002/gj.3350020408
Richards, J.P., 2022. Porphyry copper deposit formation in arcs: What are the odds? Geosphere 18, 130–155. https://doi.org/10.1130/GES02086.1
Richards, J.P., 2021. Porphyry copper deposit formation in arcs: What are the odds? Geosphere 18, 130–155. https://doi.org/10.1130/GES02086.1
Richards, J.P., 2009. Postsubduction porphyry Cu-Au and epithermal Au deposits: Products of remelting of subduction-modified lithosphere. Geology 37, 247–250. https://doi.org/10.1130/G25451A.1
Roberts, N.M.W., Spencer, C.J., 2015. The zircon archive of continent formation through time. SP 389, 197–225. https://doi.org/10.1144/SP389.14
Rock, N.M.S., Gaskarth, J.W., Rundle, C.C., 1986. Late Caledonian Dyke-Swarms in Southern Scotland: A Regional Zone of Primitive K-Rich Lamprophyres and Associated Vents. The Journal of Geology 94, 505–522.
Schaltegger, U., Schmitt, A.K., Horstwood, M.S.A., 2015. U–Th–Pb zircon geochronology by ID-TIMS, SIMS, and laser ablation ICP-MS: Recipes, interpretations, and opportunities. Chemical Geology 402, 89–110. https://doi.org/10.1016/j.chemgeo.2015.02.028
Schiller, D., Finger, F., 2019. Application of Ti-in-zircon thermometry to granite studies: problems and possible solutions. Contrib Mineral Petrol 174, 51. https://doi.org/10.1007/s00410-019-1585-3
Schofield, D.I., Potter, J., Barr, S.M., Horák, J.M., Millar, I.L., Longstaffe, F.J., 2016. Reappraising the Neoproterozoic ‘East Avalonian’ terranes of southern Great Britain. Gondwana Research 35, 257–271. https://doi.org/10.1016/j.gr.2015.06.001

Şengör, A.M.C., Özeren, S., Genç, T., Zor, E., 2003. East Anatolian high plateau as a mantle-supported, north-south shortened domal structure. Geophysical Research Letters 30. https://doi.org/10.1029/2003GL017858
Siégel, C., Bryan, S.E., Allen, C.M., Gust, D.A., 2018. Use and abuse of zircon-based thermometers: A critical review and a recommended approach to identify antecrystic zircons. Earth-Science Reviews 176, 87–116. https://doi.org/10.1016/j.earscirev.2017.08.011
Skobeltsyn, G., Mellors, R., Gök, R., Türkelli, N., Yetirmishli, G., Sandvol, E., 2014. Upper mantle S wave velocity structure of the East Anatolian-Caucasus region. Tectonics 33, 207–221. https://doi.org/10.1002/2013TC003334
Sláma, J., Košler, J., Condon, D.J., Crowley, J.L., Gerdes, A., Hanchar, J.M., Horstwood, M.S.A., Morris, G.A., Nasdala, L., Norberg, N., Schaltegger, U., Schoene, B., Tubrett, M.N., Whitehouse, M.J., 2008. Plešovice zircon — A new natural reference material for U–Pb and Hf isotopic microanalysis. Chemical Geology 249, 1–35. https://doi.org/10.1016/j.chemgeo.2007.11.005
Solari, L.A., Ortega-Obregón, C., Bernal, J.P., 2015. U–Pb zircon geochronology by LAICPMS combined with thermal annealing: Achievements in precision and accuracy on dating standard and unknown samples. Chemical Geology 414, 109–123. https://doi.org/10.1016/j.chemgeo.2015.09.008
Song, S., Wang, M., Wang, C., Niu, Y., 2015. Magmatism during continental collision, subduction, exhumation and mountain collapse in collisional orogenic belts and continental net growth: A perspective. Sci. China Earth Sci. 58, 1284–1304. https://doi.org/10.1007/s11430-015-5102-x
Soper, N.J., 1986. The Newer Granite problem: a geotectonic view. Geological Magazine 123, 227–236. https://doi.org/10.1017/S0016756800034725
Soper, N.J., Ryan, P.D., Dewey, J.F., 1999. Age of the Grampian orogeny in Scotland and Ireland. Journal of the Geological Society 156, 1231–1236. https://doi.org/10.1144/gsjgs.156.6.1231
Soper, N.J., Woodcock, N.H., 2003. The lost Lower Old Red Sandstone of England and Wales: a record of post-Iapetan flexure or Early Devonian transtension? Geol. Mag. 140, 627–647. https://doi.org/10.1017/S0016756803008380
Spencer, C.J., Kirkland, C.L., Taylor, R.J.M., 2016. Strategies towards statistically robust interpretations of in situ U–Pb zircon geochronology. Geoscience Frontiers 7, 581–589. https://doi.org/10.1016/j.gsf.2015.11.006
Stacey, J.S., Kramers, J.D., 1975. Approximation of terrestrial lead isotope evolution by a two-stage model. Earth and Planetary Science Letters 26, 207–221. https://doi.org/10.1016/0012-821X(75)90088-6
Stephens, W.E., Halliday, A.N., 1984. Geochemical contrasts between late Caledonian granitoid plutons of northern, central and southern Scotland 15.
Stephens, W.E., Halliday, H., 1979. Compositional Variation in the Galloway Plutons, in: Atherton, M.P., Tarney, J. (Eds.), Origin of Granite Batholiths. Birkhäuser Boston, Boston, MA, pp. 9–17. https://doi.org/10.1007/978-1-4684-0570-5_2
Stone, P., 2014. The Southern Uplands Terrane in Scotland – a notional controversy revisited. SJG 50, 97–123. https://doi.org/10.1144/sjg2014-001
Stone, P., KIMBELL, G.S., HENNEY, P.J., 1997. Basement control on the location of strike-slip shear in the Southern Uplands of Scotland. Journal of the Geological Society 154, 141–144. https://doi.org/10.1144/gsjgs.154.1.0141
Strachan, R.A., Alsop, G.I., Ramezani, J., Frazer, R.E., Burns, I.M., Holdsworth, R.E., 2020. Patterns of Silurian deformation and magmatism during sinistral

oblique convergence, northern Scottish Caledonides. JGS 177, 893–910. https://doi.org/10.1144/jgs2020-039
Thirlwall, M.F., 1988. Geochronology of Late Caledonian magmatism in northern Britain. JGS 145, 951–967. https://doi.org/10.1144/gsjgs.145.6.0951
Thirlwall, M.F., 1982. Systematic variation in chemistry and Nd-Sr isotopes across a Caledonian calc-alkaline volcanic arc: implications for source materials. Earth and Planetary Science Letters 58, 27–50. https://doi.org/10.1016/0012-821X(82)90101-7
Thirlwall, M.F., 1981. Implications for Caledonian plate tectonic models of chemical data from volcanic rocks of the British Old Red Sandstone. JGS 138, 123–138. https://doi.org/10.1144/gsjgs.138.2.0123
Tibaldi, A., 2008. Contractional tectonics and magma paths in volcanoes. Journal of Volcanology and Geothermal Research 176, 291–301. https://doi.org/10.1016/j.jvolgeores.2008.04.008
Tindle, G., McGARVIE, D.W., WEBB, P.C., 1988. The role of hybridization and crystal fractionation in the evolution of the Cairnsmore of Carsphairn Intrusion, Southern Uplands of Scotland. Journal of the Geological Society 145, 11–21. https://doi.org/10.1144/gsjgs.145.1.0011
Toussaint, G., Burov, E., Avouac, J.-P., 2004. Tectonic evolution of a continental collision zone: A thermomechanical numerical model. Tectonics 23. https://doi.org/10.1029/2003TC001604
Trewin, N.H., 2003. The Geology of Scotland, 4th edition. ed. Geological Society, London.
van Hunen, J., Allen, M.B., 2011. Continental collision and slab break-off: A comparison of 3-D numerical models with observations. Earth and Planetary Science Letters 302, 27–37. https://doi.org/10.1016/j.epsl.2010.11.035
van Staal, C.R., Barr, S.M., Waldron, J.W.F., Schofield, D.I., Zagorevski, A., White, C.E., 2021. Provenance and Paleozoic tectonic evolution of Ganderia and its relationships with Avalonia and Megumia in the Appalachian-Caledonide orogen. Gondwana Research 98, 212–243. https://doi.org/10.1016/j.gr.2021.05.025
Vermeesch, P., 2018. IsoplotR: a free and open toolbox for geochronology.
Villa, I.M., De Bièvre, P., Holden, N.E., Renne, P.R., 2015. IUPAC-IUGS recommendation on the half life of 87Rb. Geochimica et Cosmochimica Acta 164, 382–385. https://doi.org/10.1016/j.gca.2015.05.025
von Blanckenburg, F., Davies, J.H., 1995a. Slab breakoff: A model for syncollisional magmatism and tectonics in the Alps. Tectonics 14, 120–131. https://doi.org/10.1029/94TC02051
von Blanckenburg, F., Davies, J.H., 1995b. Slab breakoff: A model for syncollisional magmatism and tectonics in the Alps. Tectonics 14, 120–131. https://doi.org/10.1029/94TC02051
Waldron, J.W.F., Floyd, J.D., Simonetti, A., Heaman, L.M., 2008. Ancient Laurentian detrital zircon in the closing Iapetus Ocean, Southern Uplands terrane, Scotland. Geol 36, 527. https://doi.org/10.1130/G24763A.1
Waldron, J.W.F., Schofield, D.I., Dufrane, S.A., Floyd, J.D., Crowley, Q.G., Simonetti, A., Dokken, R.J., Pothier, H.D., 2014. Ganderia–Laurentia collision in the Caledonides of Great Britain and Ireland. Journal of the Geological Society 171, 555–569. https://doi.org/10.1144/jgs2013-131
Waldron, J.W.F., Schofield, D.I., Murphy, J.B., 2019. Diachronous Paleozoic accretion of peri-Gondwanan terranes at the Laurentian margin. SP 470, 289–310. https://doi.org/10.1144/SP470.11

Walker, B.A., Miller, C.F., Lowery Claiborne, L., Wooden, J.L., Miller, J.S., 2007. Geology and geochronology of the Spirit Mountain batholith, southern Nevada: Implications for timescales and physical processes of batholith construction. Journal of Volcanology and Geothermal Research, Large Silicic Magma Systems 167, 239–262. https://doi.org/10.1016/j.jvolgeores.2006.12.008

Walker, S., Bird, A.F., Thirlwall, M.F., Strachan, R.A., 2020. Caledonian and Pre-Caledonian orogenic events in Shetland, Scotland: evidence from garnet Lu–Hf and Sm–Nd geochronology. Geological Society, London, Special Publications 503, 305–331. https://doi.org/10.1144/SP503-2020-32

Watson, E.B., Wark, D.A., Thomas, J.B., 2006. Crystallization thermometers for zircon and rutile. Contrib Mineral Petrol 151, 413–433. https://doi.org/10.1007/s00410-006-0068-5

Watson, J., 1984. The ending of the Caledonian orogeny in Scotland: President's anniversary address 1983: Journal of the Geological Society: Vol 141, No 2 [WWW Document]. URL https://www.lyellcollection.org/doi/abs/10.1144/gsjgs.141.2.0193 (accessed 5.18.24).

Wendt, I., Carl, C., 1991. The statistical distribution of the mean squared weighted deviation. Chemical Geology: Isotope Geoscience section 86, 275–285. https://doi.org/10.1016/0168-9622(91)90010-T

Widmann, P., Davies, J.H.F.L., Schaltegger, U., 2019. Calibrating chemical abrasion: Its effects on zircon crystal structure, chemical composition and UPb age. Chemical Geology 511, 1–10. https://doi.org/10.1016/j.chemgeo.2019.02.026

Wiedenbeck, M., Allé, P., Corfu, F., Griffin, W. l., Meier, M., Oberli, F., Quadt, A.V., Roddick, J. c., Spiegel, W., 1995. Three Natural Zircon Standards for U-Th-Pb, Lu-Hf, Trace Element and Ree Analyses. Geostandards Newsletter 19, 1–23. https://doi.org/10.1111/j.1751-908X.1995.tb00147.x

Williams, H.M., 2004. Nature of the Source Regions for Post-collisional, Potassic Magmatism in Southern and Northern Tibet from Geochemical Variations and Inverse Trace Element Modelling. Journal of Petrology 45, 555–607. https://doi.org/10.1093/petrology/egg094

Woodcock, N.H., Jack Soper, N., Miles, A.J., 2019. Age of the Acadian deformation and Devonian granites in northern England: a review. PYGS 62, 238–253. https://doi.org/10.1144/pygs2018-009

Woodcock, N.H., SOPER, N.J., STRACHAN, R.A., 2007. A Rheic cause for the Acadian deformation in Europe. Journal of the Geological Society 164, 1023–1036. https://doi.org/10.1144/0016-76492006-129

Woodcock, N.H., Strachan, R.A., 2012. Geological History of Britain and Ireland. John Wiley & Sons.

Wu, H., Li, C., Xu, M., Li, X., 2015. Early Cretaceous adakitic magmatism in the Dachagou area, northern Lhasa terrane, Tibet: Implications for slab roll-back and subsequent slab break-off of the lithosphere of the Bangong–Nujiang Ocean. Journal of Asian Earth Sciences 97, 51–66. https://doi.org/10.1016/j.jseaes.2014.10.014

Wu, S., Wang, Y., Qian, X., Asis, J.B., Lu, X., Zhang, Y., Gan, C., 2022. Discovery of the Late Cretaceous Barru adakite in SW Sulawesi and slab break-off beneath the Central Indonesian Accretionary Complex. Journal of Asian Earth Sciences 232, 105214. https://doi.org/10.1016/j.jseaes.2022.105214

Yang, X., Wang, D., Zhang, Z.-F., 2024. Effects of Thermal Annealing and Chemical Abrasion on In-situ U-Pb Dating of Complex Ancient Zircons by

Laser Ablation ICP-MS. Atom. Spectrosc. 45. https://doi.org/10.46770/AS.2024.179

Yilmaz Şahin, S., Aysal, N., Güngör, Y., Peytcheva, I., Neubauer, F., 2014. Geochemistry and U–Pb zircon geochronology of metagranites in Istranca (Strandja) Zone, NW Pontides, Turkey: Implications for the geodynamic evolution of Cadomian orogeny. Gondwana Research 26, 755–771. https://doi.org/10.1016/j.gr.2013.07.011